Physics of the Earth and Planetary Interiors 361 (2025) 107319

Contents lists available at ScienceDirect

Physics of the Earth and Planetary Interiors

journal homepage: www.elsevier.com/locate/pepi

Radial structure of the Earth: (I) Model concepts and data

Pritwiraj Moulik [a,*], Göran Ekström [b]

[a] Department of Geosciences, Princeton University, Princeton, NJ 08544, USA
[b] Lamont-Doherty Earth Observatory of Columbia University, Palisades, NY 10964, USA

ARTICLE INFO

Keywords:
Core phases
Seismic velocities
Traveltimes
Normal modes
Surface waves

ABSTRACT

A framework is introduced for developing a radial reference model that incorporates diverse observations and techniques for improving the constraints on bulk Earth structure. This study describes new modeling concepts and reference datasets while features of the reference Earth model REM1D and geological interpretations are discussed in a companion manuscript. Recent measurements from various techniques have improved in precision and are broadly consistent, and are summarized as best estimates with uncertainties. We construct a reference dataset comprising normal-mode eigenfrequencies and quality factors, surface-wave dispersion curves, impedance constraints and travel-time curves from body waves, and astronomic-geodetic observations. Classical radial reference models do not account for the theoretical effects and observational biases resulting from heterogeneity in the crust and mantle. We address three issues that account for lateral variations in the modeling of average elastic, anelastic and density structure. First, current ray coverage of traveling waves is biased towards structure in the northern hemisphere, leading to faster velocities especially in the lower mantle. Second, horizontal wavelength of the heterogeneity that a traveling wave encounters is assumed to be much greater than that of the corresponding normal mode in most ray-theoretical and finite-frequency formulations of wave propagation. Effects of the full volumetric sensitivity on local eigenfrequencies and phase velocities that are ignored with this approximation exceed the data uncertainty for both fundamental spheroidal (Rayleigh waves, T $\geq$ 220 s) and toroidal modes (Love waves, T $\geq$ 120 s); waves at these longer periods cannot be modeled solely in terms of radial variations along the ray path. Third, non-linear effects from the strongly heterogeneous crustal structure are substantial for shorter-period waves (T $\leq$ 100 s) and need to be accounted for while deriving radial models. After accounting for these issues on heterogeneity, rapid convergence for average structure is facilitated by utilizing *a priori* constraints from recent literature, analytical sensitivity kernels that account for physical dispersion, and a flexible parameterization comprising polynomial functions and cubic B-splines. By adopting a higher order polynomial for density than the elastic structure, artifacts that imply strong inhomogeneity and non-adiabaticity are avoided in potentially well-mixed regions like the outer core. Derivative properties like the gradient of bulk modulus with pressure ($\kappa' = d\kappa/dp$) and the Bullen's stratification parameter (η_B) are adjusted in the core to match expectations from mineral physics without deteriorating the fits to reference datasets. A cubic polynomial parameterization in the lower mantle is adequate to capture possible changes in the gradients of the modulus ratio (μ/κ) associated with spin transitions in iron-bearing minerals. Radial reference models need to account for lateral heterogeneity and prior geological information in their construction to accurately represent the bulk average properties of a heterogeneous Earth.

1. Introduction

A fundamental goal in seismology is to describe the average elastic, anelastic and density variations with depth in terms of 'radially stratified' or 'spherically symmetric' one-dimensional (1D) Earth models. While no location on Earth can be strictly represented by a single radial reference model, primarily due to the strong lateral heterogeneity in the crust and uppermost mantle, this mathematical abstraction is nevertheless of critical importance to the geosciences. Average physical properties represented by radial reference Earth models are used in a variety of geophysical, geodetic, geochemical and petrological problems apart from their standard applications in seismology such as calculations of arrival times (e.g. Doornbos, 1988) and synthetic seismograms (e.g. Dahlen and Tromp, 1998). In studies of the Earth's deep interior, radial

* Corresponding author.
E-mail addresses: moulik@caa.columbia.edu, moulik@princeton.edu (P. Moulik).

https://doi.org/10.1016/j.pepi.2025.107319
Received 4 March 2024; Received in revised form 2 December 2024; Accepted 1 February 2025
Available online 10 February 2025

reference models are used for either interpreting or calibrating the average mantle geotherm (e.g. Stixrude and Lithgow-Bertelloni, 2011), bulk composition (e.g. Ringwood, 1975; McDonough and Sun, 1995), grain size evolution (e.g. Dannberg et al., 2017), energy dissipation mechanisms (e.g. Faul and Jackson, 2005), and the dynamics of mass and heat transport (e.g. Christensen and Yuen, 1985; Jeanloz and Knittle, 1989; Tackley et al., 1993). If the absolute properties of a heterogeneous Earth are to be mapped for self-consistent interpretations across the geosciences, an accurate radial model is required as a baseline for the lateral variations of a few percent that are typically reported in global and regional studies. Several generations of radial models have been constructed using datasets sensitive to average Earth structure like body-wave arrival times (e.g. Jeffreys and Bullen, 1940; Kennett and Engdahl, 1991; Morelli and Dziewonski, 1993; Kennett et al., 1995) and normal-mode eigenfrequencies (e.g. Gilbert and Dziewonski, 1975). Methodological advancements along with the high level of consensus between radial models led to the development of a preliminary reference Earth model (PREM - Dziewoński and Anderson, 1981), which combined travel-time and normal-mode data with Earth's mass and moment of inertia to solve simultaneously for elastic, anelastic and density variations.

Since the development of PREM, there has been a growing agreement on the need for modeling complexities like anisotropy and attenuation while constraining robust features like a low-velocity zone in the uppermost mantle (e.g. Anderson, 1965; Kanamori and Anderson, 1977). Recent results from seismology (e.g. Shearer and Flanagan, 1999; Gu et al., 2003; Ekström, 2011), geodesy (e.g. Pavlis et al., 2012) and mineral physics (e.g. Weidner and Wang, 2000; Wentzcovitch et al., 2010; Stixrude and Lithgow-Bertelloni, 2012) provide improved constraints on parameters ranging from Earth's mass and moment of inertia to the average depths and contrasts at seismic discontinuities. Advancements in mineral physics now afford new equations of state (EoS) for representing the physical properties of a well-mixed isochemical material under pressure. Some EoS studies have claimed that the polynomial representation of PREM, (a) produces derivative features in the outer core that may be physically implausible (e.g. Stacey, 2005), and (b) lacks the flexibility to detect localized features in the lower mantle (e.g. Kennett, 2021). For example, a positive curvature of the bulk modulus with pressure ($\kappa'' = d^2\kappa/d^2p$) in PREM is not compatible with a uniform phase and composition in the silicate lower mantle or the iron-rich outer core. A polynomial parameterization has also been questioned based on the reported values of the Bullen's stratification parameter η_B, which represent deviations from a standard adiabatic and homogeneous region that is in hydrostatic equilibrium (e.g. Bullen, 1963; Dahlen and Tromp, 1998). For example, it remains debated whether the small yet mineralogically and dynamically significant deviations of η_B from one (± 0.04) in the lower mantle and outer core are in fact an artifact of parameterization choices (e.g. Stacey, 1997; Valencia-Cardona et al., 2017). Kennett (2021) has questioned the flexibility of cubic polynomials in the elastic structure of PREM to recover localized changes in the relative behavior of shear and bulk modulus (μ/κ), which may afford signatures of spin transitions in iron-bearing minerals of the lower mantle (e.g. Badro et al., 2003; Tsuchiya et al., 2006; Wentzcovitch et al., 2010). There is broad consensus on the need for a new radial reference Earth model that incorporates latest techniques and observations while assessing the limitations of parameterization in earlier radial models. An update to the preliminary information on radial structure contained in PREM will improve inferences on bulk Earth properties and serve as the foundation for a three-dimensional (3D) reference Earth model (e.g. REM3D, Moulik et al., 2022). However, advancement and reconciliation of radial reference models has been hampered by the use of disparate datasets, geographic biases, theoretical approximations and the lack of a self-consistent methodology.

A plethora of seismological observations afford complementary information on features of geological interest. For example, some body-wave studies have proposed localized changes to velocity and density contrasts in the transition zone (e.g. Shearer and Flanagan, 1999; Revenaugh and Jordan, 1991b; Estabrook and Kind, 1996; Deuss, 2009) or inferred directly the mantle composition (e.g. Gaherty et al., 1999). Normal-mode observations used in PREM provide overlapping sensitivities in this region and can improve estimates of absolute properties and their gradients. Several widely used models like IASP91 (Kennett and Engdahl, 1991) and AK135 (Kennett et al., 1995) were optimized to fit body-wave arrival times for the purposes of earthquake location but exclude important features such as a low-velocity zone in the shallowest mantle required by surface-wave observations. Similarly, models based on long-period datasets like 1066B (Gilbert and Dziewonski, 1975) predict arrival times of body-wave phases such as S that are slow by as much as 4 s (Nolet and Moser, 1993). Improved constraints on radial Earth structure can be gleaned by jointly reconciling multiple datasets covering a broad spectrum of frequencies (~0.3 mHz – 1 Hz, ~1–3200 s).

Geographic bias is evident in the observations of traveling waves; summary arrival-time curves of several body-wave phases at teleseismic distances are biased towards velocities in the northern hemisphere due to the current distribution of stations (e.g. Dziewonski, 1984; Morelli and Dziewonski, 1991). The choice of radial (1D) reference model can introduce discrepancies in arrival times that far exceed the signal from heterogeneity interpreted in 3D tomographic studies that use body waves in isolation (e.g. Fukao et al., 2003; Li et al., 2008). Surface waves traverse large swaths of the oceanic basins and provide better geographic coverage than body waves. While recent surface-wave compilations include data from new stations in the Pacific Ocean Basin (e.g. Ekström, 2011) and temporary deployments such as the Hawaiian PLUME experiment (e.g. Ma et al., 2014), large areas in the southern oceans still lack good station coverage. Normal modes, by their very nature, provide a more even global coverage by integrating the volumetric effects of heterogeneity. Due to theoretical advancements that can leverage data from recent, large earthquakes (e.g. Masters et al., 1983), expanded sets of eigenfrequencies and quality factors are now available for constraining the average Earth structure (e.g. Resovsky and Ritzwoller, 1998; Deuss et al., 2013). Accounting for geographic bias in body- and surface-wave arrival times while reconciling normal-mode observations can afford an unbiased description of average structure. However, this critical objective in seismic imaging has not been met by any radial reference model to date.

Another potential source of discrepancy is the strong crustal heterogeneity that cannot be adequately described by a single radial model (Dziewoński and Anderson, 1981). New crustal models afford detailed constraints on density and velocity structure that were unavailable during the construction of PREM (e.g. Bassin et al., 2000; Laske et al., 2013). Propagation of a specific type of traveling wave (or the corresponding normal mode) can be understood in terms of eigenfunctions that describe displacements at depth and the eigenfrequency of vibration (e.g. Dahlen and Tromp, 1998). Several studies have applied linear corrections to remove the effect of ocean-continent crustal dichotomy on long-period waveforms (e.g. Woodhouse and Dziewoński, 1984), where local shifts in eigenfrequency due to crustal structure are calculated from a global radial model and any regional perturbations to the displacement eigenfunctions at depth are neglected. However, strong crustal variations between orogens, platforms, shields, continental margins, and oceanic basins, can change the shape of eigenfunctions and affect the local eigenfrequencies in a significantly non-linear fashion (Montagner and Jobert, 1988). Non-linear effects of the crust have been shown to strongly influence the modeling of seismic observables like long-period waveforms (e.g. Kustowski et al., 2007; Lekic et al., 2009). All radial reference models to date have assumed that the bulk Earth datasets used in their construction are largely unaffected by crustal structure.

Inferences regarding the upper mantle, especially using complexities like anisotropy and attenuation, could be impacted by crustal structure.

In order to explain the observed discrepancies in the propagation velocities of Love and Rayleigh waves, radial anisotropy with faster shear-wave velocities in the horizontal rather than the vertical polarization ($v_{SH} > v_{SV}$) was proposed as an intrinsic and pervasive feature in the uppermost mantle (Anderson, 1965). Numerous regional (e.g. Montagner and Jobert, 1988; Nishimura and Forsyth, 1989) and global studies (e.g. Ekström and Dziewonski, 1998) have found additional evidence for the robustness of this feature, especially beneath oceanic basins. Several studies have also reported strong shear attenuation in the asthenosphere based on the amplitude decay of surface waves (e.g Anderson and Hart, 1978; Sailor and Dziewonski, 1978; Widmer et al., 1991; Selby and Woodhouse, 2002; Dalton et al., 2008). Reproducing the fundamental features of attenuation could help disentangle the contributions from grain size, temperature, partial melt and composition (e.g. Faul and Jackson, 2005; Abers et al., 2014), and calibrate mineral physical parameters in geodynamic simulations (e.g. Dannberg et al., 2017). However, the impact of strong crustal variations on these global features in seismological models has not yet been evaluated. For example, it is typically assumed that the influence of heterogeneity on the Love-Rayleigh wave discrepancy in phase velocities is weak, can be accounted for in a linear fashion or get averaged out by combining many earthquakes and stations (e.g. Anderson and Dziewoński, 1982). Radial models like PREM assume that the average Love-Rayleigh discrepancy in velocities can be attributed solely to the radial anisotropic variations. Quantifying the relative contribution of lateral heterogeneity to the bulk Earth datasets could help refine the estimates of average anisotropy and attenuation in the Earth's upper mantle.

Apart from data and modeling considerations, theoretical formulations for constructing radial models may need to be evaluated due to heterogeneity in the Earth's interior. Modeling of traveling (body and surface) waves as a superposition of fundamental modes and overtones in the geometrical optics limit consists of several approximations including, (a) local-eigenfrequency approximation where the sensitivity kernels to structure at various spherical harmonic degrees (K^s) are approximated by their degree-zero counterparts ($K^s \simeq K^0$, Jordan, 1978); (b) great-circle ray approximation that treats the surface integral of the product of two spherical harmonics by a line integral along the great-circle path between the source and receiver; (c) stationary phase approximation; (d) approximations of the Wigner-3j symbols (e.g. Dahlen and Tromp, 1998). These theoretical assumptions are interrelated and often contingent on the local-eigenfrequency approximation, which is valid only when the horizontal wavelengths of structural heterogeneity (s) are much greater than that of the normal mode (${}_nS_l$, ${}_nT_l$) with its power concentrated in degrees $s \ll l$. If these asymptotic limits are satisfied, observed shifts in normal-mode eigenfrequencies (e.g. Silver and Jordan, 1981; Masters et al., 1982) and lateral variations in surface-wave dispersion (e.g. Ekström, 2011) can be attributed to local radial structures rather than the full volumetric heterogeneity. Several theoretical formulations assume the local-eigenfrequency approximation to model the effects of heterogeneity on waveforms (e.g. Mochizuki, 1986a; Park, 1987; Romanowicz, 1987; Nolet, 1990) and in the Jeffreys-Wentzel-Kramers-Brillouin (JWKB) description of surface wave propagation (e.g. Tromp and Dahlen, 1992). Location of a normal mode multiplet with this approximation is the average of local perturbation in eigenfrequency over the great-circle path connecting the source and receiver (Jordan, 1978). The phase velocity of the corresponding surface wave can be represented as a sum of their fractional dispersion along the ray path. Validity of the local-eigenfrequency approximation is also assumed in recent tomographic inversions (e.g. Woodhouse and Dziewoński, 1984; Lebedev and van der Hilst, 2008; French and Romanowicz, 2014; Moulik and Ekström, 2014) and while accounting for crustal effects on waveforms (e.g. Kustowski et al., 2007; Lekic et al., 2010). Formulations that account for coupling between modes within (e.g. Woodhouse and Dziewoński, 1984) or across overtone branches (e.g. Li and Tanimoto, 1993) are also contingent on these asymptotic limits in the frequency band of interest. Since we employ a broad range of frequencies (~0.3 mHz – 1 Hz) and correct the data for lateral heterogeneity, wavelength limits to the local-eigenfrequency approximation need to be evaluated.

In this study, we formulate new concepts for constructing radial models that account for the intertwined theoretical and observational effects of lateral heterogeneity on bulk Earth structure. A radial reference Earth model (REM1D), in the modern sense, is one that satisfies several types of geophysical observations and corresponds to the spherical average of Earth's 3D heterogeneity (degree-0 term in spherical harmonics). Our approach of utilizing a broad spectrum of data and accounting for the theoretical complexities of attenuation and anisotropy is an extension of full spectrum tomography used for constructing 3D Earth models (FST; Moulik and Ekström, 2014, 2016). A key ingredient for model construction is a reference dataset that provides best estimates with associated uncertainties based on available measurements, as is the standard procedure in physics, chemistry, geodesy and the material sciences (e.g. Birge, 1929; Mohr et al., 2016). Different types of data employed in the construction of a reference bulk Earth dataset are described in Section 2. The coupled effects of heterogeneity on radial structure are discussed in Section 3 while modeling choices to incorporate prior information in our inversions are summarized in Section 4. We conclude, in Section 5, with a discussion of the general implications from the reference datasets on bulk Earth structure. Primary features of REM1D and geological interpretations are discussed in a separate manuscript (Moulik and Ekström, 2025, hereafter referred to as Paper II).

2. Reference bulk Earth data

We reconcile diverse observations that afford sensitivity to radial structure with the creation of a reference bulk Earth dataset (e.g. Tables 1–3, Figs. 1–4). The modeling schemes described below account for crustal effects and, whenever possible, any geographical bias in sampling mantle heterogeneity. In contrast to the numerical sensitivity kernels and non-linear optimization schemes employed in previous studies (e.g. PREM), our formulation leverages first-order perturbation theory to efficiently model these diverse datasets in terms of degree-0 perturbations to any 1D or 3D Earth model.

2.1. Astronomic-geodetic data

Earth's mass and moment of inertia provide constraints on the radial density variations in the mid and upper mantle with sensitivity decreasing monotonically from the surface to center of the Earth (CoE). There is an overall requirement for a mass concentration towards the CoE because inertia coefficient is less than what is expected for a uniform body (0.4). Absolute perturbations in density ($\delta\rho$) from the starting reference model (ρ_0) are constrained to match the observed mass and moment of inertia of the Earth. These constraints can be expressed as

$$\mathscr{M}_{true} - \mathscr{M}_0 = \int_0^R 4\pi r^2 \delta\rho \ dr \tag{1}$$

and

$$\mathscr{I}_{true} - \mathscr{I}_0 = \int_0^R 4\pi r^2 \left(\frac{2}{3} r^2\right) \delta\rho \ dr, \tag{2}$$

where $\mathscr{M}_{true}$ is the mass, $\mathscr{I}_{true}$ the moment of inertia, and the integral is taken over the radius r from CoE to the mean Earth radius R. In the rest of this manuscript, the subscript '0' (e.g. $\mathscr{M}_0$, $\mathscr{I}_0$) denotes values from the starting radial reference model (START, Section 4.2). Constraints on these parameters from previous studies and the best estimates obtained here are summarized in Table 1.

The definition of mean Earth radius (R) depends on the geodetic

Table 1
Reference astronomic-geodetic data. The best estimates and uncertainties of the reference dataset are marked in bold; model predictions are from PREM (Dziewoński and Anderson, 1981) and AK135 (Kennett et al., 1995). OBANI (Woodhouse, 1988) and MINEOS (Masters et al., 2011) refer to values typically used in these standard tools for solving normal modes of a radial reference model; WGS84 and its successors EGM96, EGM2008 are geodetic reference systems. Model predictions or inconsistent, low-precision measurements are denoted by a "†" and excluded from uncertainty estimation. The types of data in italics are variables whose best estimates and uncertainties are determined from those of other independent variables. Relative uncertainty is undefined if the variable needs to be prescribed as a constant during model construction (e.g. radius R) or if the source does not specify uncertainty. Subscripts correspond to the method for determining the best estimate and its uncertainty (Section 2.6).

Data	Symbol	Units	Value ± Uncertainty	Relative uncertainty	Source
Equatorial radius	a_e	m	6,378,137 ± 3†	4.7×10^{-7}	WGS84; Chambat and Valette (2001)
			6,378,136.3$_{\mathrm{prf}}$	–	EGM96, EGM2008
Flattening	f	–	1/298.257223563†	–	WGS84
			1/299.627†	–	Hydrostatic prediction (Nakiboglu, 1982, PREM)
			1/298.256415099$_{\mathrm{prf}}$	–	**This study**; EGM96; EGM2008
Geocentric gravitational constant[a]	$G\mathcal{M}$	10^{9} m^{3} s^{-2}	398,600.4418 ± 0.0008†	2.0×10^{-9}	WGS84; Luzum et al. (2011)
			398,600.4415 ± 0.0040$_{\mathrm{prf}}$	$\mathbf{1.0 \times 10^{-8}}$	Ries et al. (1992); Chambat and Valette (2001) **This study**, EGM96, EGM2008
Radius	R	m	6,371,012 ± 15	2.4×10^{-6}	Romanowicz and Lambeck (1977)
			6,371,001 ± 2	3.1×10^{-7}	Khan (1983)
			6,370,994 ± 3	4.7×10^{-7}	Chambat and Valette (2001)
			6,371,000[b]$_{\mathrm{prf}}$	–	**This study**; PREM; Kennett (1998)
Angular velocity	Ω	10^{-5} rad s^{-1}	**7.292115**$_{\mathrm{prf}}$	–	OBANI/MINEOS; Groten (2000) **This study**; WGS84; EGM96; EGM2008
Gravitational constant	G	10^{-11} m^{3} kg^{-1} s^{-2}	6.6723†	–	PREM; OBANI/MINEOS
			6.67408 ± 0.00031$_{\mathrm{prf}}$	$\mathbf{4.7 \times 10^{-5}}$	**This study;** Mohr et al. (2016)
Atmospheric mass	$\mathcal{M}_{atm}$	10^{18} kg	5.1†	–	Yoder (1995)
			5.1480 ± 0.0003$_{\mathrm{prf}}$	$\mathbf{5.8 \times 10^{-5}}$	**This study;** Trenberth et al. (2005)
Solid Earth mass	$\mathcal{M}_{true}$	10^{24} kg	5.9742† ± 0.006	–	Romanowicz and Lambeck (1977)
			5.9742† ± 0.0036	6.0×10^{-4}	Khan (1983)
			5.9736	–	Yoder (1995); Dickey (1995) Cazenave (1995); Kennett (1998)
			5.9733 ± 0.0090	1.5×10^{-3}	Chambat and Valette (2001)
			5.97218 ± 0.00060	1.0×10^{-4}	Chambat et al. (2010)
			5.97236[c] **± 0.00028**[d]$_{\mathrm{prf}}$	$\mathbf{4.7 \times 10^{-5}}$	**This study**
			5.974†	–	PREM; OBANI/MINEOS
			5.970†	–	AK135
Inertia coefficient	$\mathcal{I}_{true}/\mathcal{M}_{true}R^{2}$	–	0.330830† ± 0.000015	4.5×10^{-5}	Romanowicz and Lambeck (1977)
			0.330729 ± 0.000007	2.1×10^{-5}	Khan (1983)
			0.332†	–	Denis et al. (1997)
			0.3307144	–	Kennett (1998)
			0.330714 ± 0.000008	2.4×10^{-5}	Chambat and Valette (2001)
			0.330690 ± 0.000009[e]	2.6×10^{-5}	Chambat et al. (2010)
			0.330714$_{\mathrm{prf}}$ **± 0.000024**$_{\mathrm{sd}}$	$\mathbf{7.3 \times 10^{-5}}$	**This study**
			0.3308†	–	PREM
			0.33109†	–	AK135

(*continued on next page*)

Table 1 (*continued*)

Data	Symbol	Units	Value ± Uncertainty	Relative uncertainty	Source
Inertia	$\mathscr{I}_{true}$	10^{37} m^2 kg	8.018 ± 0.012	1.5×10^{-3}	Chambat and Valette (2001)
			8.017 ± 0.001$_{\text{prf}}$	**1.2×10^{-4}**	**This study**
			8.021[†]	–	PREM
			8.023[†]	–	AK135
Average density	$\bar{\rho} = \mathscr{M}_{true} / \frac{4}{3}\pi R^3$	kg m^{-3}	5515[†]	–	PREM; OBANI/MINEOS
			5513.59[c] ± 0.26$^{d}_{\text{prf}}$	**4.7×10^{-5}**	**This study**
Geocentric conversion factor	W	–	0.993277	–	PREM
			0.9933056[f]	–	**This study**
Distance factor	Δ_F	km/degree°	111.1949	–	PREM
			111.31948[g]	–	**This study**

[a] Including the atmosphere.
[b] Approximation to equivolumetric sphere radius $R = a_e[1-f]^{1/3} = 6{,}371{,}000.07$ m.
[c] Accounts for atmospheric mass $\mathscr{M}_{true} = \mathscr{M} - \mathscr{M}_{atm}$.
[d] Calculated with the same relative standard uncertainty as that of G.
[e] Accounts for mean solid topography from digital elevation models.
[f] Geographic to geocentric conversion of latitudes (θ) are done with $\theta' = \text{atan}(W \cdot \tan(\theta))$.
[g] Great circle distances in degrees are converted to km using the factor $\Delta_F = 2\pi a_e/360/1000$ (e.g. Seidelmann, 1992).

reference system (e.g. WGS84, EGM2008), expressions used for equivalent radii (e.g. Chambat and Valette, 2001), and on whether continental volume above the geoid from a digital elevation model is included (~230 m, e.g. Fan, 1998). For historical reasons, we stick to a value of $R = 6371$ km for model construction, which corresponds roughly to the radius of a sphere with the same volume as the reference ellipsoid in the EGM2008 geodetic system (Pavlis et al., 2012). Revised astronomic-geodetic constants influence the calculations of great-circle distances through the conversion of geographic to geocentric latitudes (e.g. W) and the distance factor (Δ_F) between angular degrees and kilometers (e.g. Seidelmann, 1992). The former conversion provides the parametric or reduced latitudes on a spherical geodesic of equatorial radius a_e, while the latter conversion uses the spherical law of cosines to calculate distances that account somewhat for the relative spacing of latitudes on the original reference ellipsoid. Past seismological studies have often used a distance factor based on the mean radius (R) instead of the equatorial radius (a_e) leading to systematically smaller distances between geographic locations (Table 1). This choice can lead to systematically faster velocities of traveling waves; new constants were therefore adopted during the construction of the reference dataset of multi-mode surface wave dispersion (Moulik et al., 2022).

Solid Earth mass ($\mathscr{M}_{true}$) and average density ($\bar{\rho}$) are known with about the same precision as the gravitational constant (G), while moment of inertia ($\mathscr{I}_{true}$), which depends on the precessional constant, is nearly as well-determined. We chose $\mathscr{M}_{true}$ to fit the latest estimates of geocentric gravitational constant $G\mathscr{M}$ from EGM2008, atmospheric mass $\mathscr{M}_{atm}$ from Trenberth et al. (2005), and gravitational constant G from Mohr et al. (2016). Relative standard uncertainty in G has reduced to 4.7×10^{-5} from 1.5×10^{-3} in earlier studies (e.g. Chambat and Valette, 2001), affording more precise estimates of $\mathscr{M}_{true}$ and $\bar{\rho}$. We adopt a recent estimate of inertia coefficient (0.714) with an uncertainty (σ_{sd}) corresponding to the whole range of recently reported values (Table 1); our inertia ratio ($\mathscr{I}_{true}/\mathscr{M}_{true}$) is consistent with high-precision estimates reported by recent studies to within one standard deviation (e.g. Chambat et al., 2010).

Apart from directly constraining density structure, the new set of astronomic-geodetic data also influence the modeling of wave propagation. In the context of normal mode formalisms for standing and traveling waves, these revised estimates are used in calculations of eigenfrequencies and eigenfunctions (e.g. Woodhouse, 1988; Masters et al., 2011) and the related sensitivity kernels for inferring internal structure (e.g. Mochizuki, 1986b). Astronomic-geodetic constants are used for normalizing physical state variables in wave propagation codes and the various choices can lead to discrepant estimates of normal-mode eigenfrequencies. Keeping the radial structure fixed at PREM, eigenfrequencies predicted by our revised constants differ from those obtained earlier by up to 0.5–4 times the uncertainties in Section 2.2. These constants most strongly influence the characterization of low-frequency normal modes (0.3–5.7 mHz), especially the radial (${}_{0-6}S_0$) and fundamental modes (${}_0S_{2-9}$), as well as some overtones (e.g. ${}_1S_{8-9}$, ${}_2S_{10-13}$). The choice of astronomic-geodetic constants therefore critically influences our inferences of radial structure, especially in the deeper regions of the Earth.

2.2. Normal modes

We first discuss classical approximations and derive new expressions for spherically-averaged properties that account for physical dispersion and crustal heterogeneity (Section 2.2.1). Thereafter, we reconcile normal-mode observations from various techniques for a reference dataset of eigenfrequencies and quality factors (Section 2.2.2).

2.2.1. Theoretical background

The multiplet eigenfrequencies (ω) and quality factors (Q) of Rayleigh-wave equivalent spheroidal modes ${}_nS_l$ and Love-wave equivalent toroidal modes ${}_nT_l$ with overtone number n and angular order l provide depth-integrated constraints on Earth structure. Substantial coupling can occur between different multiplets in a realistic Earth that is rotating and has small asphericities in structure. These additional effects must be accounted for in order to prevent a biased spherically-

Table 2
Reference datasets sensitive to the absolute variations and gradients of physical properties. We list the number of eigenfrequencies (ω), quality factors (Q) and the number of unique modes for each subset of normal-mode observations. Eigenfrequencies of fundamental modes include values converted from average dispersion curves following eq. 12. The spheroidal overtones are sub-divided based on their sensitivity either to v_P variations or core structure. Frequency range and overtone number (0 - fundamental modes) of the surface-wave dispersion curves from GDM52 (Ekström, 2011) and Ma et al. (2014) are provided. Body-wave arrival times of specific phases and branches are obtained from SP6 at the corresponding components and range of great-circle distances (Δ). Phases arrivals are associated either with the transverse (T) or vertical component (V).

Normal modes	**No. of ω | modes**	**No. of Q | modes**
Radial	34 | 16	29 | 10
Spher. Fund.	360 | 91	180 | 67
Spher. Over. (v_P)	156 | 50	111 | 50
Spher. Over. (Core)	236 | 46	195 | 46
Spher. Over. (Other)	538 | 64	175 | 64
Tor. Fund.	132 | 92	77 | 57
Tor. Over.	230 | 185	47 | 18
Dispersion curves	**Overtone number**	**Frequency (mHz)**
Love wave (GDM52)	0	4–40
Love wave (Ma et al., 2014)	0	7–30
Rayleigh wave (GDM52)	0	4–40
Rayleigh wave (Ma et al., 2014)	0	5–35
Body-wave phases	**Weight w (Component)**	**Great-circle Δ**
P	5.0 (V)	27°–125°
S	5.0 (T)	27°–125°
PP	1.5 (V)	53°–180°
SS	1.0 (T)	56°–150°
PcP	2.0 (V)	26°–70°
ScS	2.0 (T)	19°–65°
ScP	2.0 (V)	18°–62°
SP	1.0 (V)	95°–128°
PKIKP	4.0 (V)	118°–180°
PKP_{ab}	4.0 (V)	156°–178°
PKP_{bc}	4.0 (V)	151°–153°
$PKKP_{ab}$	1.5 (V)	111°–122°
$PKKP_{bc}$	1.5 (V)	83°–122°
SKS	3.0 (V)	91°–123°
SKKS	1.5 (V)	65°–178°
SKIKP	1.0 (V)	113°–160°
SKP_{bc}	1.0 (V)	141°–148°
P′P′ (PKPPKP)	1.0 (V)	56°–70°

averaged elastic and anelastic structure (e.g. Masters et al., 1983). Recent studies have measured ω and Q as degree-0 terms of the complex splitting coefficient ($\sigma_{00} = c_{00} + id_{00}$), while accounting for the effects of rotation, ellipticity and lateral heterogeneity (e.g. Resovsky and Ritzwoller, 1998; Deuss et al., 2013). This procedure is equivalent to evaluating the spherically symmetric adjustments to the multiplet eigenfrequencies ($\Delta\omega$) and quality factors $\left(\Delta Q^{-1}\right)$ predicted by the reference model. Following Giardini et al. (1988), the various terms can be related as

$$\omega = \omega_0\left[1 + c_{00}\cdot(4\pi)^{-\frac{1}{2}}\right] \tag{3}$$

and

$$Q = \frac{\omega}{2\left[\alpha_0 + d_{00}\cdot\omega_0(4\pi)^{-\frac{1}{2}}\right]}, \tag{4}$$

where $\alpha_0 = \omega_0/2Q_0$ is the imaginary part of frequency ω_0 with quality factor Q_0. Assuming small and independent perturbations, the c_{00} term that is representative of the elastic and density variations (eq. 3), can be neglected when anelastic perturbations are being considered (i.e. $\omega \simeq \omega_0$ in eq. 4). This approximation leads to expressions for degree-0 splitting coefficients c_{00} and d_{00} in terms of the $\Delta\omega$ and ΔQ observations as

$$c_{00} = \sqrt{4\pi}\cdot\frac{\Delta\omega}{\omega_0}, \tag{5}$$

and

$$d_{00} = \frac{\sqrt{4\pi}}{2}\cdot\Delta Q^{-1}, \tag{6}$$

This transformation can be used to relate ω and Q measurements to the degree-0 components of heterogeneity, which are inverted during the construction of a radial reference model.

Now, let us consider whether these simple transformations hold true for a strongly heterogeneous Earth model. The elastic splitting function F_E (e.g Woodhouse et al., 1986; Giardini et al., 1987) of a normal mode (${}_nS_l$, ${}_nT_l$) with angular order l represents shifts in eigenfrequencies due to the lateral heterogeneities of angular order s and azimuthal order t following

$$F_E(\theta,\phi) = \sum_{s=0}^{2l}\sum_{t=-s}^{s} c_{st}Y_{st}(\theta,\phi), \tag{7}$$

where Y_s^t denotes a fully normalized surface spherical harmonic (Dahlen and Tromp, 1998). The effect of heterogeneity is modeled using self-coupled splitting coefficients, denoted by c_{st}, which account for perturbations in the i-th model parameter m_i^{st}, according to

$$c_{st} = \int_0^R \sum_i \delta m_i^{st} K_{m_i}^s \, dr + \sum_d \delta h_d^{st} H_d^s, \tag{8}$$

where subscript i stands for the five elastic parameters (v_{PH}, v_{PV}, v_{SH}, v_{SV}, and η) and density (ρ) while subscript d stands for the topography of three major internal discontinuities (410 km and 650 km discontinuity, and core-mantle boundary CMB). In the local-eigenfrequency limit, when the horizontal wavelength of the heterogeneity is much greater than that of the mode ($l \gg s$), frequency shift is solely a function of the pole of the great circle joining the source and receiver (Jordan, 1978). This wavelength requirement is valid only when power of structural heterogeneity is concentrated in the low degrees ($s \ll l$). In the case of high-frequency modes with large l, sensitivity kernels are similar for all degrees s ($K_{m_i}^s \simeq K_{m_i}^0$), resulting in splitting functions and related phase velocity variations that are proxies for radial structure beneath each point in the Earth. Local eigenfrequency variations are defined as

$$F_E^{\text{local}}(\theta,\phi) = \frac{\delta\omega_{\text{local}}(\theta,\phi)}{\omega_0} = \sum_s^{2l}\sum_{t=-s}^{s} c_{st}^{\text{local}}Y_{st}(\theta,\phi) \tag{9}$$

where c_{st}^{local} is related to perturbations in the i-th model parameter m_i^{st}, according to

Table 3
Reference dataset of contrasts in physical properties across major internal discontinuities. Our compilation includes contrasts in elastic parameters and density at transition-zone discontinuities and the inner-core boundary (ICB) from the analysis of body-wave phases (e.g. ScS_n), normal modes and receiver functions (RFs). We define the contrast as $\%\Delta x = 100 \times \Delta x / x_{avg}$, where $\Delta x = |x_+ - x_-|$ is the magnitude of difference between parameters at the top (subscript '+') and bottom (subscript '–') of the discontinuity and $x_{avg} = [x_+ + x_-]/2$ is the average. Parameter x can be density ρ, shear modulus μ, bulk modulus κ, shear-wave velocity (v_S) and impedance (Z_S), compressional-wave velocity (v_P) and impedance (Z_P), and bulk-sound velocity (v_Φ). Subscripts correspond to the method for determining the best estimate and its uncertainty (Section 2.6). Values used as the reference dataset and employed in the starting model (Section 4.2) are marked in bold. Estimates from mineral physics are only provided for comparison (see Paper II) and are not employed while determining the reference seismological dataset.

Discontinuity	Values ± Uncertainty							Data	Source
	$\%\Delta v_P$	$\%\Delta v_S$	$\%\Delta\rho$	$\%\Delta\kappa$	$\%\Delta v_\Phi$[§]	$\%\Delta Z_S$[§]	$\%\Delta Z_P$[§]		
410 km $\alpha \rightarrow \beta$	–	5.4	3.9	–	–	9.2 ± 2	–	Seismic (ScS_n, $sScS_n$)	Revenaugh and Jordan (1991b)
	–	–	–	–	–	6.7 ± 1.1	–	Seismic (S_dS)	Shearer (1996)
	7.3[†]	9.7[†]	0.9[†]	–	–	10.6[†]	8.2	Seismic (P_dP,S_dS)	Shearer and Flanagan (1999)
	–	–	–	–	–	7.8 ± 0.6	5.3 ± 0.5	Seismic (S_dS)	Chambers et al. (2005)
	4.8 ± 0.1	5.1 ± 0.4	4.8 ± 0.2	–	–	9.9 ± 0.6	9.6 ± 0.3[†]	Seismic (P_dP, S_dS, RFs)	Lawrence and Shearer (2006)
	–	4.0 ± 2.4	3.4 ± 1.4	–	–	7.4 ± 1.0	–	Seismic (S_dS)	Huang et al. (2019)
	2.5–4.8	**3.4–5.4**	**3.9–5.0**	–	–	**8.3**$_{prf}$ ± **1.6**$_{sd}$	**7.5**$_{prf}$ ± **2.2**$_{sd}$	**Best estimates**	**This study**
	2.5	3.4	5.0	9.0	2.0	8.3	7.5	Model predictions	PREM
	–	–	*5.1*	*20.2*	*7.6*	–	–	*ab initio* (Mg_2SiO_4,~ 1500 K, 16.3 GPa)	Yu et al. (2008); Wentzcovitch et al. (2010)
	–	*7.9 ± 0.9*	*2.9*	–	–	*10.8 ± 0.9*[§]	–	Min. phy (pyrolite, 3 % Al, 1473 K)	Gaherty et al. (1999); Weidner and Wang (2000)
	5.6	*6.8*	*3.3*	–	–	*10.1*[§]	*8.9*[§]	Min. phy (pyrolite, 1600 K)	Stixrude and Lithgow-Bertelloni (2011)
650 km $\gamma \rightarrow$ pv + pc	–	8.5	6.1	–	–	14.4 + 2	–	Seismic (ScS_n, $sScS_n$)	Revenaugh and Jordan (1991b)
	–	–	–	–	–	9.9 ± 1.5	–	Seismic (S_dS)	Shearer (1996)
	2.5	6.1	6.2	–	–	12.3	8.7	Seismic (P_dP)	Estabrook and Kind (1996)
	2	4.8	5.2	5.5	0.16	10	7.2	Seismic (P_dP, S_dS)	Shearer and Flanagan (1999)
	0.7 + 0.8[†]	4.2 ± 0.3[†]	4.4 ± 0.7[†]			8.6 + 1	5.1 ± 1.5	Seismic (P_dP, S_dS, RFs)	Lawrence and Shearer (2006)
	–	4.1 ± 1.7	4.5 ± 0.6	–	–	8.6 ± 1.2	–	Seismic (S_dS)	Huang et al. (2019)
	0.7–2.5	**4.8–8.5**	**5.2–6.2**	–	–	**10**$_{prf}$ ± **1.4**$_{sd}$	**7.2**$_{prf}$ ± **2.1**$_{sd}$	**Best estimates**	**This study**
	4.6	6.5	9.3	16.0	3.4	15.8	13.9	Model predictions	PREM
	–	–	*7.9*	*7.7 ± 1*	*−0.1 ± 0.48*	–	–	*ab initio* (Mg_2SiO_4, 1900 K and 23.2 GPa)	Yu et al. (2007); Wentzcovitch et al. (2010)
	5.4 ± 4.0	*6.3 ± 6.0*	*6.2 ± 0.4*	–	–	*11.7 ± 10.0*[§]	*11.6 ± 4.4*[§]	Mineralogy (piclogite, 1500 K)	Vacher et al. (1998)
	3.3	*5.5*	*5.4*	–	–	*10.9*[§]	*8.7*[§]	Min. phy (pyrolite, 1600 K)	Stixrude and Lithgow-Bertelloni (2011)
		Δv_S (km/s)	**$\Delta\rho$ (g/cm^3)**						
ICB	–	–	<1.1–1.2	–	–	–	–	Seismic(PKiKP/PcP)	Tkalčić et al. (2009); Waszek and Deuss (2015)
	–	2.82 ± 0.32	0.52 ± 0.24	–	–	–	–	Seismic(PKiKP/PcP, PKiKP/P)	Koper and Dombrovskaya (2005)
	–	2–3	0.6–0.9	–	–	–	–	Seismic(PKiKP/PcP)	Cao and Romanowicz (2004)
	–	>2.5	<1	–	–	–	–	Seismic(PKiKP/PcP)	Shearer and Masters (1990)
	–	3.45 ± 0.1	~0.55	–	–	–	–	Seismic(normal modes)	Shearer and Masters (1990)

(*continued on next page*)

Table 3 (*continued*)

Discontinuity	Values ± Uncertainty							Data	Source
	–	–	0.82 ± 0.18	–	–	–	–	Seismic(normal modes)	Masters and Gubbins (2003)
	–	**2.5–3.5**	**0.5–0.9**	–	–	–	–	**Best estimates**	**This study**
	–	3.5	0.6	–	–	–	–	Model predictions	PREM

† Excluded in best estimates because of inconsistencies with other studies, possibly due to tradeoffs.

§ For small contrasts in properties, $\%\Delta Z_S = \%\Delta v_S + \%\Delta\rho$, $\%\Delta Z_P = \%\Delta v_P + \%\Delta\rho$, and $\%\Delta v_\Phi = [\%\Delta\kappa - \%\Delta\rho]/2$, unless explicitly provided by a study.

$$c_{st}^{\text{local}} = \int_0^R \sum_i \delta m_i^{st} K_{m_i}^0 \, dr + \sum_d \delta h_d^{st} H_d^0. \tag{10}$$

Here, structural heterogeneity at all degrees s are mapped to the corresponding splitting coefficient through degree-0 kernels ($K_{m_i}^0$, H_d^0; Supplementary Figs. S1 and S2), representing sensitivity to local radial structure while ignoring full volumetric effects (in contrast to $K_{m_i}^s$ and H_d^s in eqs. 7 and 8). In Section 3.2, we evaluate the validity limits of this local-eigenfrequency approximation based on our current knowledge of the power of structural heterogeneity.

Even when the local-eigenfrequency approximation is valid, it can be demonstrated that mode eigenfrequencies and related degree-0 splitting coefficients cannot be directly attributed to radial variations due to the intertwined effects of crustal structure and that further corrections are needed (Section 3.3). In order to be consistent with our treatment of surface-wave dispersion (Section 2.3), we express the degree-0 splitting coefficient as

$$c_{00} = \frac{\sqrt{4\pi}}{\omega_0} \cdot \left[\Delta\omega_{obs} - \Delta\omega_{\text{crust}}^{\text{non-linear}}\right]. \tag{11}$$

where subscript *obs* denotes observations and the latter term is the non-linear contribution from crustal heterogeneity. Phase-velocity perturbation at a fixed frequency ω is related to the eigenfrequency perturbation at a fixed wavenumber k by

$$\left(\frac{\delta c}{c}\right)_\omega = \frac{c}{U}\left(\frac{\delta\omega}{\omega}\right)_k, \tag{12}$$

where c and U are the phase and group velocity of the normal mode, respectively (Dahlen and Tromp, 1998). Consequently, non-linear crustal contributions to eigenfrequencies can be expressed as

$$\Delta\omega_{\text{crust}}^{\text{non-linear}} = \frac{U_0}{c_0} \Delta c_{\text{crust}}^{\text{non-linear}} \omega_0. \tag{13}$$

Non-linear crustal effects on the average phase-velocity perturbation of a traveling surface wave are

$$\Delta c_{\text{crust}}^{\text{non-linear}} = \left\langle \frac{c_{\text{crust}}(\theta,\phi) - c_0}{c_0} \right\rangle, \tag{14}$$

where $\langle\cdot\rangle$ denotes the spherical average of a 2-dimensional map of phase-velocity perturbations evaluated at a given latitude θ and longitude ϕ. Here, c_{crust} is the local phase velocity calculated with a radial reference model where a crustal model (e.g. Bassin et al., 2000; Laske et al., 2013) is overlain on top of average mantle and core structure (Section 3.3). In practice, non-linear phase-velocity corrections (eq. 14) are stored roughly at evenly-spaced frequencies between 0.04 and 4 mHz and evaluated thereafter for any mode eigenfrequency (ω_0) using cubic B-spline interpolation. A similar non-linear crustal correction is not applied to the quality-factor measurements (eq. 6) as this non-linear effect is small relative to the uncertainty in available data (Section 3.3).

The imaginary parts of the self-coupled splitting coefficients are related to perturbations in bulk ($q_\kappa = Q_\kappa^{-1}$) and shear attenuation ($q_\mu = Q_\mu^{-1}$), as

$$d_{00} = \int_0^R \left[\mu\delta q_\mu^{00} K_\mu^0 + \kappa\delta q_\kappa^{00} K_\kappa^0\right] dr, \tag{15}$$

where K_μ^0 and K_κ^0 are the kernels for degree-0 perturbations to shear (μ) and bulk modulus (κ), respectively, while accounting for the effects of physical dispersion in the reference model. The degree-0 elastic splitting coefficient c_{00} is related to the degree-0 perturbations in the i-th model parameter $\left(m_i^{00}\right)$, according to

$$c_{00} = \int_0^R \sum_{i=1}^{6} \delta m_i^{00} K_{m_i}^0 \, dr + \frac{2}{\pi} ln\left[\frac{\omega}{2\pi}\right] d_{00}. \tag{16}$$

The kernel expressions (Supplementary Figs. S1 and S2) are obtained from Mochizuki (1986b) and Dahlen and Tromp (1998), and we recalculate the sensitivities to degree-0 perturbations when the reference model is updated in our iterative modeling scheme (Section 4.3). The attenuation term (d_{00}) denotes the contribution from physical dispersion based on an absorption band model with constant quality factors (Q_κ, Q_μ) across the entire seismic frequency band (∼1–3200 s; e.g. Kanamori and Anderson, 1977).

2.2.2. Data compilation

We compile a large dataset of normal modes available from the literature (Figs. 1–3, Table 2, Supplementary Figs. S3–S19) obtained using five techniques: single station analysis (Smith and Masters, 1989; Roult et al., 1990), iterative spectral fitting (ISF, e.g. Giardini et al., 1987, 1988; Li et al., 1991; Resovsky and Ritzwoller, 1998), singlet stripping (SS, e.g. Buland et al., 1979; Ritzwoller et al., 1986), multiplet stripping (MS, e.g. Gilbert and Dziewonski, 1975), and regionalized multiplet stripping (RMS, e.g. Widmer-Schnidrig, 2002). Single station methods involve histogram analyses of peak-frequency measurements from single recordings and therefore need to be corrected for aspherical structure. The ISF technique iteratively fits a set of observed normal-mode spectra but is non-linear and requires accurate descriptions of the earthquake source. Other processing techniques utilize simplifying assumptions to linearize the determination of eigenfrequencies and quality factors. Singlet stripping regards the dominant asphericities sensed by the target normal-mode multiplet as axisymmetric, a restrictive assumption that may be applicable only at small angular orders. Multiplet stripping linearly estimates resonance functions from multiple records ignoring aspherical structure and typically requires similar fidelity of source mechanisms as the ISF technique. These techniques can provide an unbiased estimate only if the ray paths sample the Earth evenly or their relative sampling is accounted for during the fitting procedure. Regionalized multiplet stripping was introduced for overtones with high angular order where other linearized techniques often fail to disentangle the contributions from fundamental modes. This technique accounts more explicitly for the geographic coverage with sets of seismograms that share a common great circle, utilizing the asymptotic relations of the local-eigenfrequency approximation (Jordan, 1978).

A compilation of normal-mode eigenfrequencies and quality factor

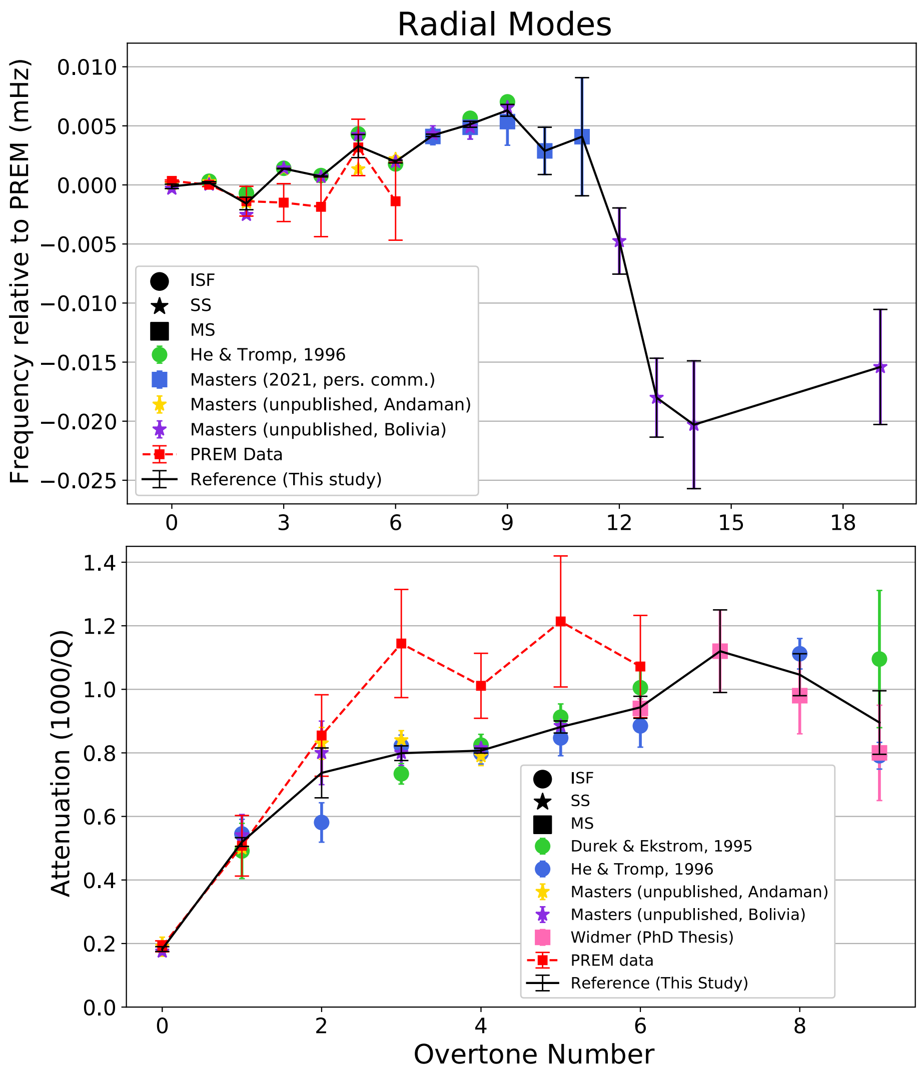

Fig. 1. Observed eigenfrequencies and quality factors of radial modes (${}_nS_0$, where n is overtone number). The reference data and uncertainties (in black) are estimated based on the procedure outlined in Section 2.6. Symbols denote the various types of normal-mode techniques (e.g. ISF, MS, SS) discussed in Section 2.2. For clarity, eigenfrequencies are plotted relative to the values predicted by PREM.

observations made prior to the year 2001 was obtained from a website (Laske, 2001) hosted at the Scripps Institution of Oceanography (hereafter Scripps). This compilation extended the measurements used in the development of PREM with average global values of fundamental-mode surface-wave attenuation (Durek et al., 1993; Durek, 1994), fundamental-mode and overtone data from the analysis of normal mode spectra using the standing wave approach (Smith and Masters, 1989; Widmer et al., 1991; He and Tromp, 1996) as well as the unpublished updates to these data. Recent occurrence of several large earthquakes, expansion of the global seismic network along with theoretical and computational advancements have led to new measurements of normal modes (e.g. Widmer et al., 1992; Resovsky and Pestana, 2003; Häfner and Widmer-Schnidrig, 2013; Deuss et al., 2013; Schneider and Deuss, 2020). Recent measurements account for the coupling between spheroidal modes and are therefore likely to bias less the results on spherically-averaged structure (e.g. Masters et al., 1983). We augment the dataset compiled at Scripps with revised estimates from Masters (2020, personal communication) and published studies (Deuss et al., 2011, 2013). Singlet stripping measurements of the radial (${}_{0-6}S_0$) and fundamental modes (${}_0S_{2-6}$, ${}_0T_{2-6}$) from the deep ($d = 647$ km) Bolivia earthquake in 1994 (Masters and Widmer, 1995) are updated with improved estimates from the 2004 Sumatra (Andaman) earthquake (M_W 9.3). Additionally, new measurements are included from applications of the multiplet stripping (Widmer, 1991) and regionalized multiplet stripping techniques (Widmer-Schnidrig, 2002). The eigenfrequency estimates based on the multiplet stripping technique are biased low but generally agree with other techniques within the 2-σ uncertainty bounds (e.g. Fig. 2). Available measurements are broadly consistent across various normal-mode studies and can be reconciled with independent surface-wave techniques to determine our best estimates and uncertainties. For example, normal-mode eigenfrequencies of fundamental modes measured using standing wave approaches lie within the 95 % confidence interval of surface-wave dispersion measurements (Section 2.3).

We test the consistency between various subsets of data and use a preferred subset for the reference dataset construction. Inconsistencies between measurements can be attributed to techniques, quality of data or the approximations employed. A few inconsistent observations are detected by performing joint inversions with all data types and tracking anomalously large misfits ($\chi^2 > 1500$) e.g. quality factor of the v_P-sensitive mode ${}_{11}S_{25}$ (Deuss et al., 2013). Quality factors of fundamental spheroidal modes measured using the traveling (surface) wave approach (e.g. Durek et al., 1993) are lower than the measurements that utilize the standing wave (normal mode) approach (e.g. Widmer et al., 1991). Durek and Ekström (1997) suggested that the normal mode approach can bias attenuation measurements towards lower values due to effects

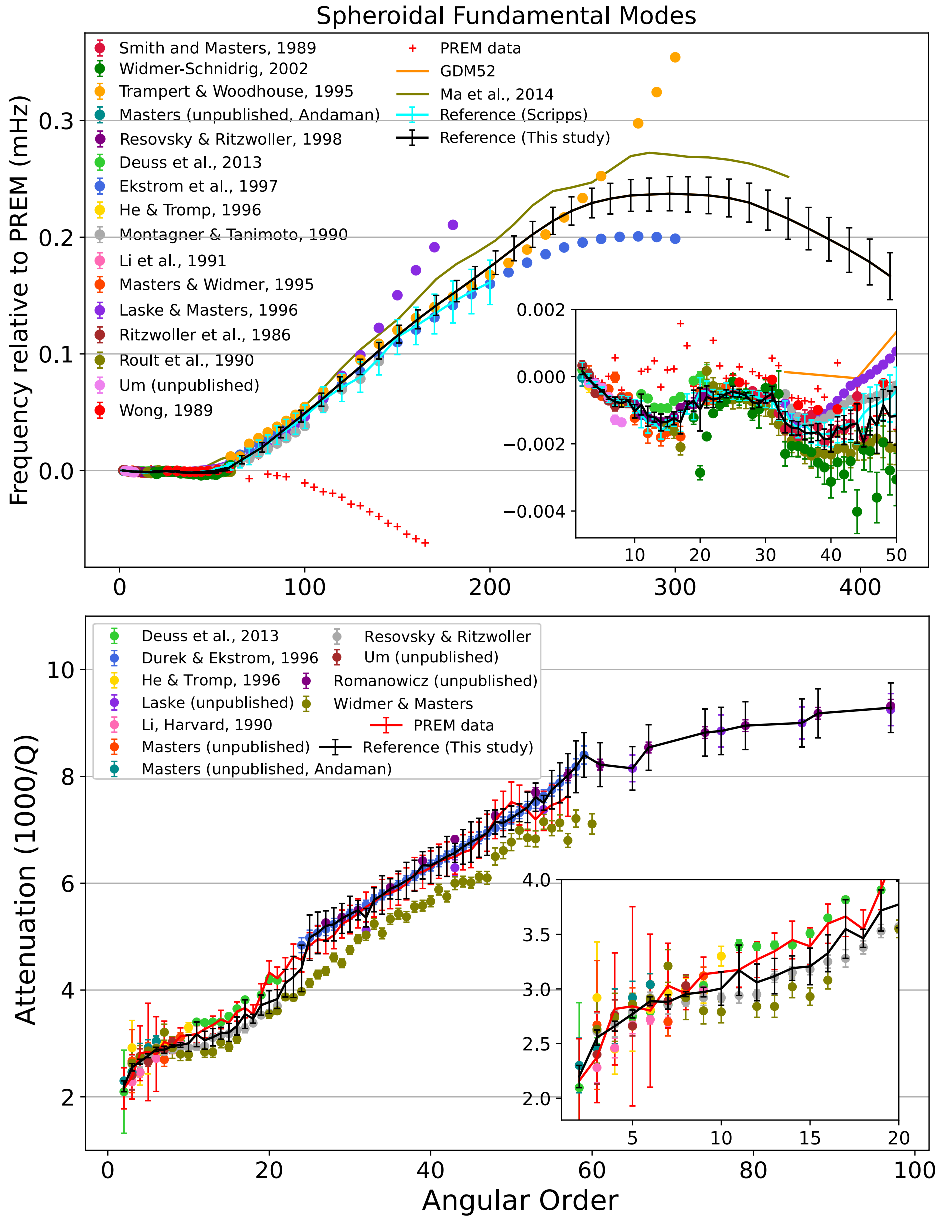

Fig. 2. Observed eigenfrequencies and quality factors of Rayleigh-wave equivalent spheroidal fundamental modes (${}_0S_l$, where l is angular order). The reference data and uncertainties (in black) are estimated based on the procedure outlined in Section 2.6. Inset figures zoom into the values for long-period vibrations at small angular orders. At shorter periods (T < 150 s), estimates of average surface wave dispersion are converted to eigenfrequencies for Rayleigh waves ($l > 58$). A small catalog of best estimates from Scripps based on data till the year 2000 is plotted for comparison wherever available (light blue curves). For clarity, eigenfrequencies are plotted relative to the values predicted by PREM. Similar plots for spheroidal overtones are provided as Supplementary Figs. S3–S12.

of noise on a long time series while Masters and Laske (1997) pointed to the problem of selecting appropriate windowing for long-period surface waves as a reason to favor the normal mode measurements. There is limited consensus on the kind of measurement that provides a more robust representation of Earth's attenuation structure (e.g. Roult and Clévédé, 2000; Romanowicz and Mitchell, 2007). Our reference dataset transitions smoothly from values consistent with normal mode estimates at low frequencies to surface wave estimates at higher frequencies ($l \geq 32$, T < 250 s). Reference data typically corresponds to the mean of available quality factors and standard uncertainty at low frequencies, while a preferred value and relative uncertainty is used at high frequencies ($\mu_{\mathrm{prf}} \pm \sigma_{\mathrm{rel}}$, Section 2.6). This choice results in robust fits to the measurements of fundamental-mode Rayleigh waves at periods shorter than 250 s, and is consistent with the approach used for constructing the radial attenuation model QL6 (Durek and Ekström, 1996). Several inconsistencies in the data and uncertainties have also been reported by other studies. The uncertainty estimates in the catalog from Scripps are anomalously low for the dataset measured by Y. Um (Resovsky et al., 2005). We modify the reported uncertainty estimates to account for the wide variety in the quality of measurements; based on our experiments, these choices do not influence strongly the primary features of average Earth structure (Paper II).

2.3. Surface-wave dispersion curves

Global dispersion curves of fundamental-mode surface waves provide constraints on average elastic properties and density in the upper mantle (Supplementary Fig. S2). In the overlapping periods of vibrations (4–8 mHz, Fig. 2, Table 2), estimates of average dispersion from Rayleigh-wave studies are in agreement ($\pm 2\sigma$) with independent

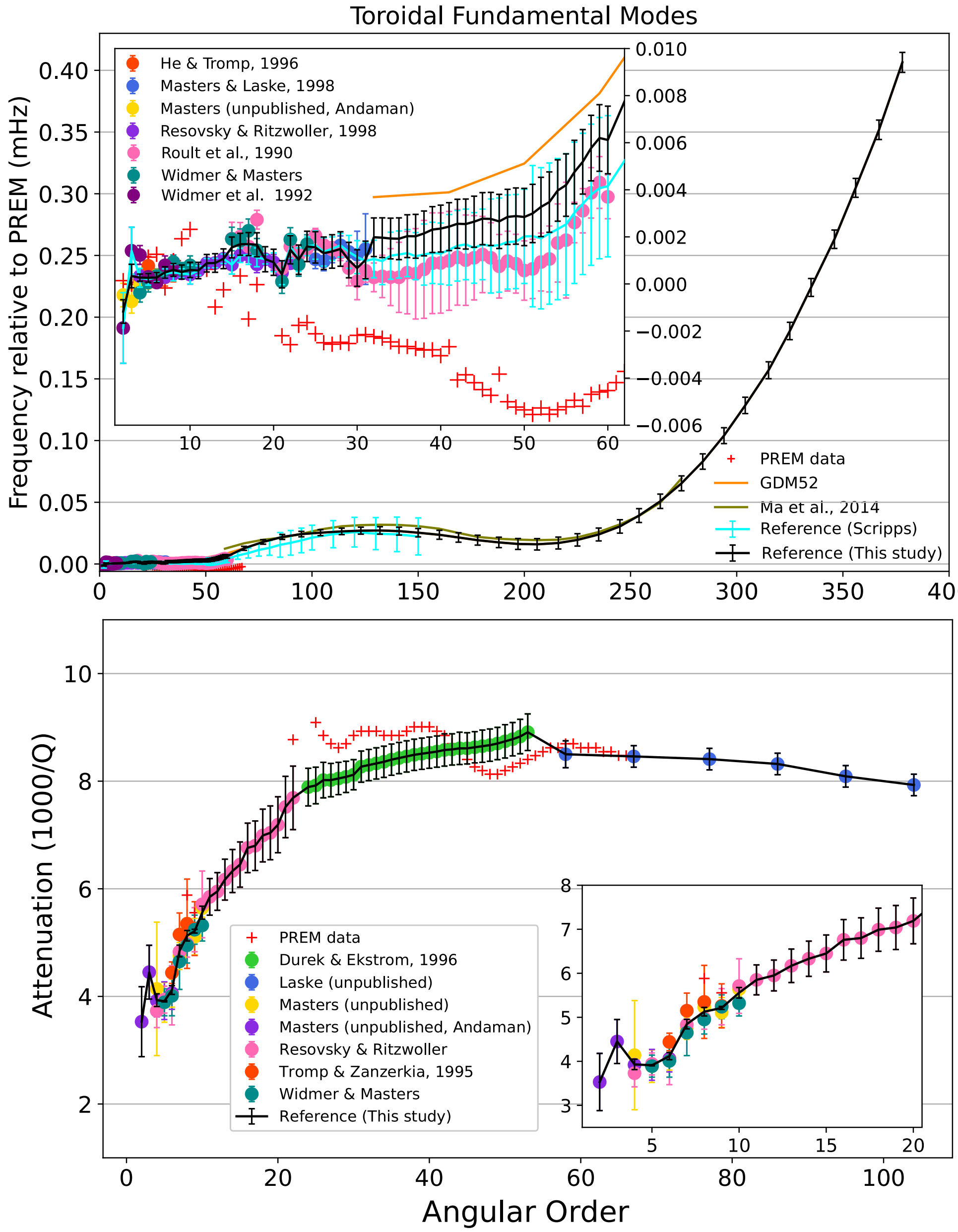

Fig. 3. Observed eigenfrequencies and quality factors of Love-wave equivalent toroidal fundamental modes (${}_0T_l$, where l is angular order). The reference data and uncertainties (in black) are estimated based on the procedure outlined in Section 2.6. Inset figures zoom into the values for long-period vibrations at small angular orders. At shorter periods (T < 150 s), estimates of average surface wave dispersion are converted to eigenfrequencies for Love waves ($l > 60$). A small catalog of best estimates from Scripps based on data till the year 2000 is plotted for comparison wherever available (light blue curves). For clarity, eigenfrequencies are plotted relative to the values predicted by PREM. Similar plots for toroidal overtones are provided as Supplementary Figs. S13–S19.

constraints on the eigenfrequencies of spheroidal fundamental modes (Smith and Masters, 1989; Roult et al., 1990). Consistency across surface-wave studies from the 1990's tends to deteriorate at shorter periods corresponding to fundamental modes of angular order (l) greater than ~150–200 (e.g. Laske and Masters, 1996; Trampert and Woodhouse, 1995). Such discrepancies are likely due to past limitations in geographic coverage and theoretical approximations on the azimuthal variations in phase velocity. Recent surface-wave studies account for the azimuthal variations in phase slowness (Ekström, 2011; Ma et al., 2014), potentially reducing tradeoffs between average anisotropic velocity and azimuthal anisotropy in the upper mantle. We choose degree-0 terms of isotropic phase-velocity maps from recent dispersion models as constraints in our modeling as they provide direct sensitivity to average Earth structure (Fig. 4). Average phase velocities in the range of 25–250 s are constrained well by the extensive dataset employed in recent studies; GDM52 was constructed using the minor- and major-arc components of the phase-anomaly data obtained from 3330 shallow ($h > 50$ km) earthquakes from 2000 to 2009. A recent global surface-wave study by Ma et al. (2014), hereafter referred to as Scripps14, employed a clustering technique with minor-arc waveforms from all $M_W > 5.5$ earthquakes that occurred between 1976 and 2008.

While the data and methodology are somewhat distinct between GDM52 and Scripps14, average phase-velocity perturbations are highly consistent and do not differ by more than 0.15 % for both Love and Rayleigh waves (Fig. 4a). The relative uncertainties are substantially lower for Love waves (< 10 %) than for Rayleigh waves at periods shorter than 100 s, potentially due to choices such as the stricter quality control and exclusion of azimuthal variations in phase-velocity inversions. In periods that overlap with normal-mode techniques (~150–250 s), agreement deteriorates but GDM52 values still lie within

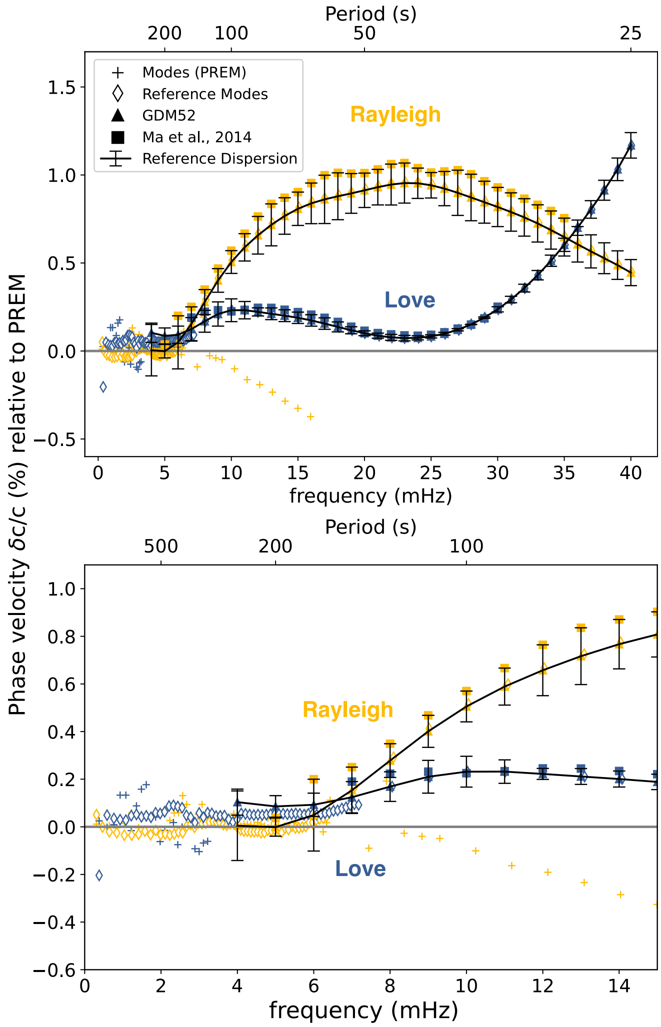

Fig. 4. Reference data of average phase-velocity perturbations (dc/c) for Love (in blue) and Rayleigh (in yellow) waves between 25 and 250 s. Reference dataset of normal mode eigenfrequencies (Figs. 2 and 3) and those used in the construction of PREM ('+' symbols) are converted to phase-velocity perturbations (dc/c, eq. 12). Values from the global dispersion model GDM52 (Ekström, 2011) and the model of Ma et al. (2014) are highly consistent. The reference dispersion data (in black) are estimated with the GDM52 measurements as the preferred mean and uncertainties dictated based on the scatter in data. In the overlapping frequencies of vibration (4–8 mHz), estimates of average dispersion and mode eigenfrequencies are in agreement ($\pm 1\sigma$) demonstrating the consistency between traveling- and standing-wave techniques. All values are calculated relative to the phase velocities obtained from PREM.

the 2-σ uncertainty bounds of mode data. Due to the high level of consistency (Fig. 4), we use the average dispersion data from GDM52 (μ_{prf}) as our best estimate and a standard deviation (σ_{sd}) that spans the various available estimates. When only a single estimate of average phase velocity is available (e.g. 25 s Love wave from GDM52), we determine uncertainty based on the nearest available (i.e. in terms of frequency) estimate of relative uncertainty in measurements (σ_{rel}).

Since GDM52 was parameterized in terms of slowness perturbations (dp/p), we derive explicitly the phase-velocity maps (dc/c) relative to PREM before incorporating the spherical averages in our inversions. This procedure leads to estimates of average dispersion that are slightly different than those in the original study (cf. Fig. 15 in Ekström, 2011). The average dispersion can be expressed as

$$\left\langle \frac{\delta c}{c_0}(\theta,\phi) \right\rangle = \Delta c_{\text{1D}}^{\text{linear}} + \Delta c_{\text{crust}}^{\text{non-linear}} = \frac{\delta c}{c_0} + \Delta c_{\text{crust}}^{\text{non-linear}}, \tag{17}$$

where the first term on the right $(\delta c/c_0)$ represents the linear contribution from the degree-0 perturbation to the radial reference model while the second term corresponds to the non-linear contributions from crustal heterogeneity (eq. 14). In order to linearize the forward problem in terms of mantle structure, we express the GDM52 dispersion curves as a set of degree-0 splitting coefficients corrected for crustal effects. Several studies use PREM as the reference model to measure perturbations in phase velocity (eqs. 14 and 17); we therefore convert the values to perturbations from our starting model. Using eqs. 5 and 12, the corresponding splitting coefficient c_{00} can be expressed as

$$c_{00} = \sqrt{4\pi}\,\frac{U_0}{c_0}\left[\frac{c_{\text{PREM}}}{c_0}\left(1 + \left\langle \frac{\delta c}{c_{\text{PREM}}} \right\rangle_{obs} - \frac{c_0}{c_{\text{PREM}}}\right) - \Delta c_{\text{crust}}^{\text{non-linear}}\right], \tag{18}$$

where subscript *obs* denotes the observed phase anomaly while c_0 and U_0 are the phase and group velocities from the starting reference model, respectively.

The conversion of Rayleigh and Love-wave dispersion curves to degree-0 splitting coefficients of equivalent spheroidal and toroidal modes allows us to adopt a linearized scheme for inverting radial structure using eq. 16. In the interest of computational efficiency when calculating the non-linear contributions (eq. 14), dispersion data are inverted only at a set of discrete reference periods - 25, 27, 30, 32, 35, 40, 45, 50, 60, 75, 100, 125, 150, 200 and 250 s. We use a weighting function for the dispersion curves that is inversely proportional to frequency of the surface wave to compensate for the high overall sensitivity of phase-velocity perturbations to the shallowest mantle and crustal structure.

2.4. Summary body-wave arrivals

The choice of a reference model can introduce discrepancies in arrival times of body waves that can exceed the signal from heterogeneity typically interpreted in tomographic studies of the Earth's interior. These issues arise largely due to choices on data weighting during model construction and the related discrepancies in the sampling of heterogeneity. Revised sets of constraints are therefore needed so that REM1D can accurately predict the average rather than a geographically biased onset of body-wave phases. Large sets of arrival times for various phases are collected by the International Seismological Centre (ISC), which could ideally be used directly for inversions of radial structure. A natural way to include such constraints is to reprocess the arrival times for summary time-distance curves of the major mantle and core phases. The reference model SP6 (Morelli and Dziewonski, 1993) was constructed to represent the global average of isotropic shear and compressional velocities while accounting for large residuals (e.g. Jeffreys, 1932) as well as the geographic bias from an uneven source-station distribution (e.g. Morelli and Dziewonski, 1991). Summary arrival times of major body-wave phases are largely consistent across techniques and have not required an update to their original estimates to date (e.g. Morelli and Dziewonski, 1993; Kennett, 2020).

Arrival-time curves of various mantle and core phases sampled at 1° intervals are used as constraints in our inversions (Table 2). We incorporate SP6 predictions in lieu of raw arrival times since their modeling philosophy emphasized construction of a spherical average rather than simply fitting the available data; arrival-time curves were constructed from well-distributed shallow ($h < 50$ km) earthquakes and corrected for lateral heterogeneity in the lower mantle (Dziewonski, 1984). Inclusion of SP6 arrival times as constraints circumvents the issues of baseline corrections that are well known in some early models (e.g. Jeffreys and Bullen, 1940). We evaluate measures of fit for each phase branch by comparing the SP6-predicted arrival times (t^{SP6}) with the predictions from a model (t). For example, fit to a phase (p) and branch (b) is expressed as

$$\chi^2_{pb} = \sum_{\Delta=\Delta_1}^{\Delta_2} \left[t_{pb}(\Delta) - t^{\mathrm{SP6}}_{pb}(\Delta) \right]^2, \tag{19}$$

where Δ=[Δ_1,Δ_2] is the range of great-circle distances where it is observed (Table 2). The values of Δ considered encompass almost the entire range used in the construction of earlier body-wave velocity models (Morelli and Dziewonski, 1993; Kennett et al., 1995). We chose a weighted sum of the fits to various phases as our measure of overall fit to the arrival-time curves; the weights (w) are chosen based on the expected amplitude of arrivals and coda of the preceding phases (Kennett et al., 1995). The overall criterion of fit to the arrival-time curves (χ^2_{tt}) can be expressed as

$$\chi^2_{tt} = \sum_p \sum_b w_{pb} \chi^2_{pb} \tag{20}$$

where the summation is done over all phases being considered (Table 2). Since radial reference models are typically used in body-wave studies by adding the necessary corrections for asphericities, we exclude contributions from lateral variations in the crust (e.g. Kustowski, 2007) and Earth's ellipticity (e.g. Dziewonski and Gilbert, 1976) in our comparisons. The phases S, SS and ScS are calculated on the transverse component (SH-motion) while other phases are calculated on the vertical component (P-SV motion), in order to account for radial anisotropy in the shallowest mantle. Predictions of arrival times from the anisotropic PREM model show deviations of ~2 s for teleseismic S and SS waves when the effects from $v_{SH} > v_{SV}$ anisotropy in the shallowest mantle are not considered. While diffracted waves (P_{diff}, S_{diff}) pass through substantial lateral heterogeneity and may not be adequately modeled with a simple ray representation (e.g. Kennett et al., 1995), they provide important constraints on the average structure in the lowermost mantle and are included in our inversions whenever the raypath can be traced (Woodhouse, 1981). The crustal and upper-mantle P and S arrivals out to 26° are excluded as there is considerable regional variation in their arrival times (Kennett et al., 1995). Several triplications from transition-zone discontinuities that arrive at distances up to 30° are also excluded from our analysis.

In order to incorporate the SP6 travel-time predictions as constraints, we parameterize the model in terms of variations to the five elastic parameters in a radially anisotropic medium and calculate the sensitivities numerically. The elastic parameters in the mantle and core are perturbed by 0.01–0.05 units ($< \cdot >$ in Fig. 5) and rays are traced though the suite of perturbed anisotropic models using a formulation modified from Woodhouse (1981). The perturbations in arrival times relative to the reference model, sampled at every 1° great-circle distance, are then assimilated into a sensitivity matrix used in the joint inversions. This procedure requires a scheme for automatic identification of branches in arrival-time curves derived from a large suite of perturbed radial models. A simple branch-classification scheme based on a prescribed range of distances is prone to branch misidentification. A clear distinction of mantle phases at short teleseismic distances ($\Delta \leq 30°$) is not straightforward to automate due to the triplications from transition-zone discontinuities. While we limit the number of spurious arrivals by permitting only small perturbations in the elastic moduli (Fig. 5), the intersection of branches can differ based on the details of radial structure. We start by tracing rays to the farthest stations and track the variation in slowness (s) and $d\Delta/ds$ with great-circle distance (Δ). The slowness variations of the propagating rays are used to identify the main branch of mantle phases (e.g. P, S, SS) and $d\Delta/ds$ variations are used to identify the prograde and retrograde branches of core phases (e.g. PKP, PKKP).

2.5. Discontinuity phases

The radial extent of the mantle transition zone and contrasts in physical properties across its internal discontinuities are constrained primarily using body waves. A discontinuity shallower than the 670 km in PREM has been reported in global stacks of SS precursors with average depth values ranging from ~653–660 km globally (e.g. Shearer and Masters, 1992; Shearer, 1993; Flanagan and Shearer, 1998; Deuss, 2009). We impose the average depth of discontinuities in the transition zone at 410 and 650 km, consistent with global compilations of SS precursors (Shearer, 1990; Gu et al., 2003). A discontinuity depth shallower than 670 km is required to match average time residuals of SS precursors, whose bounce points are biased towards structure within and around the Pacific Ocean basin. The bounce points of SS precursors have retained this geographic bias since the late 1990's across different techniques and compilations (Supplementary Fig. S20) due to the current source-station distribution. Most studies report strong depressions (exceeding 15 km) in the 650-km discontinuity beneath the slab-like anomalies in the circum-Pacific regions and substantially weaker depth variations (~1 km) in the mid-Pacific region (e.g. Shearer and Masters, 1992; Flanagan and Shearer, 1998; Gu and Dziewonski, 2002; Kustowski et al., 2008; Houser et al., 2008; Moulik and Ekström, 2014). After accounting for this geographic bias and the tradeoffs between velocity and topography of discontinuities using full-spectrum tomography, the spherically-averaged depths of both 410- and 650-km discontinuities do not deviate by more than 0.17 km in 3D tomographic models (S362ANI+M; Moulik and Ekström, 2014). Mineral physical calculations with a pyrolitic composition also indicate that the discontinuity depth may be shallower than 670 km in PREM (Table 3), although uncertainties of phase diagrams (Weidner and Wang, 2000) and strong dependence on temperature and compositional variations (e. g Cammarano et al., 2005) limit higher precision. For example, the shallower 650-km discontinuity in our models corresponds to a pressure difference with PREM of less than 0.19 GPa (Paper II), which is within the uncertainty bounds arising from temperature and composition during the dissociation reaction of ringwoodite into bridgmanite and ferropericlase (e.g. Ishii et al., 2019; Katsura, 2022).

Transition zone discontinuities at 410 and 650 km have velocity and density contrasts ($\%\Delta x$, Table 3) that are much less certain than their topography due to methodological approximations (e.g. incoherent stacking, discrepant frequency bands, focusing effects) and relatedly the greater scatter in amplitude observations than in travel time data (e.g. Shearer, 1991, 1993; Bai and Ritsema, 2013). Nevertheless, several studies have attempted to estimate either the contrast in impedance or velocity and density across the transition zone discontinuities using SS and PP precursors (e.g. Shearer and Flanagan, 1999; Shearer, 1996; Estabrook and Kind, 1996; Chambers et al., 2005), receiver functions (e. g. Lawrence and Shearer, 2006), and ScS reverberations (e.g. Revenaugh and Jordan, 1991b). Based on available constraints and the procedure described below, we determine best estimates of these parameters in Table 3 for various applications.

Precursors to the PP and SS phases afford some of the best constraints on bulk impedance contrasts due to the spatial averaging inherent in the stacking procedure, finite width of their Fresnel zones and good reflection-point coverage away from the geographically-limited sources and receivers. Amplitudes of these underside reflections from discontinuities (S_dS, P_dP where d is 410 or 650) depend on epicentral distance and contrast in impedance (Z_P, Z_S), the product of density and seismic velocity. There is a tradeoff between contrasts in density ($\Delta\rho$) and velocity (Δv_P, Δv_S) that fit the amplitudes of SS precursors equally well in global stacks (e.g. Shearer and Flanagan, 1999). The impedance contrasts needed to fit these data also correspond roughly to estimates from ScS reverberations at normal incidence (e.g. Revenaugh and Jordan, 1991b). Our best estimates and uncertainty for impedance contrasts cover the whole range of consistent measurements to within the 95 % confidence interval; uniform distribution with a range of values is provided instead for the contrasts in velocities and density due to the tradeoffs. For example, the velocity (and density) contrast at the 410-km discontinuity reported by Shearer and Flanagan (1999) are excluded from our best estimates as they are anomalously large (and small) compared to other studies even though the associated impedance contrast is consistent ($\pm 2\sigma$) with other estimates. Recent seismological studies agree that relative amplitude ratios of $S_{410}S$/SS and $P_{410}P$/PP imply P and S wave impedances (Z_P, Z_S) that are consistent with PREM at the 95 % confidence interval. The estimates of S wave impedance obtained from relative amplitudes of SS precursors are broadly in agreement with those from SH-polarized mantle reverberations such as ScS and sScS (e.g. Revenaugh and Jordan, 1991a, 1991b). We adopt the impedance contrasts from PREM as our best estimate for the 410-km discontinuity and specify an uncertainty that spans the full range of reported measurements.

Most studies agree that the impedance contrasts in PREM at the 650-km discontinuity are anomalously strong by a factor of ∼1.5–2, resulting in an relative amplitude ratio of $S_{650}S$/SS that is ∼2–3 times stronger than is observed globally (e.g. Shearer, 1991; Shearer and Flanagan, 1999; Deuss, 2009). The absence of $P_{650}P$ in long-period stacks, particularly at epicentral distances $\sim 120^\circ$ where there is less interference from other seismic phases, has been explained by a considerably smaller step change in density and velocity than PREM (e.g. Estabrook and Kind, 1996; Lawrence and Shearer, 2006; Deuss, 2009). Due to the lower S wave impedance, AK135 is widely used in lieu of PREM while analyzing SS precursor waveforms. We use the preferred value of shear impedance contrast ($\%\Delta Z_S$) from Shearer and Flanagan (1999) as our best estimate as it falls roughly within the 95 % confidence interval of other studies (Table 3). Overall, our best estimates are consistent with earlier results from several long-period reflected and converted phases, and imply P and S wave impedance contrasts at the 410-km discontinuity that are ∼0.8–1.1 times the contrasts at the 650-km discontinuity (e.g. Shearer, 1991).

2.6. Uncertainty estimation

Since several estimates with or without reported uncertainties are available for nearly every type of measurement (m), we create a reference dataset (m=$\mu \pm \sigma$) for constructing reference Earth models and data validation in other applications (e.g. Tables 1–3). Our best estimate of the mean (μ) is based on several considerations: (1) value from a preferred study $\left(\mu_{\text{prf}}\right)$ if it either supersedes the earlier estimate (e.g. G from Mohr et al. (2016)) or is the only available constraint; (2) the weighted mean of the measurements ($\mu_{\text{wei}} = \sum \mu_i/\sigma_i^2 / \sum 1/\sigma_i^2$), when the data have relative uncertainties (σ/μ) that are similar (within $\pm 10^{-5}$) given modeling approximations (e.g. normal mode eigenfrequencies at periods > 300 s) or when the reported uncertainties are based on similar techniques (e.g. bootstrapping); (3) mean of available measurements (μ_{avg}), if estimates of uncertainty are neither available nor reasonable for one or more of the measurements (e.g. quality factors of normal modes). When a normal distribution for a parameter cannot be justified based on modeling considerations (e.g. due to tradeoffs in Section 2.5), we provide our best estimate as a range of acceptable values (m=[m_{min},m_{max}], Table 3).

The uncertainty assigned to our best estimates (σ) is determined according to: (1) reported uncertainty of a preferred study (σ_{prf}), accounting for the propagation of uncertainties from independent variables (e.g. $\mathscr{M}_{true}$ from $G\mathscr{M}$); (2) a standard deviation (σ_{sd}), which spans the range of available estimates when best estimate is a preferred value $\left(\mu_{\text{prf}}\right)$ but multiple estimates need to be accounted for (e.g. inertia coefficient); (3) standard error of the mean (σ_{sem}), when best estimate is the mean (μ_{avg}); (4) weighted uncertainty of all reported uncertainties $\left(\sigma_{\text{wei}} = \sqrt{1/\sum 1/\sigma_i^2}\right)$, either when best estimate is the weighted mean (μ_{wei}) or when all available measurements have very similar means (i.e. $\sigma_{\text{sem}} \ll \sigma_{\text{wei}}$); (5) for a single estimate with no reported uncertainty, it is prescribed to have the same relative uncertainty as that of the nearest available datum in frequency and measurement type (σ_{rel}). Subscripts denoting the procedure above are available as metadata and used throughout this manuscript (e.g. Table 1).

3. Coupled effects of heterogeneity and bulk structure

We account for the coupled nature of lateral heterogeneity and bulk (average) structure in the modeling and interpretation of reference datasets (Section 2). Outstanding questions persist regarding the extents to which observational (Section 3.1) and theoretical limitations (Sections 3.2 and 3.3) are influenced by this modeling choice.

3.1. Structural insights from data and accounting for geographic bias

Geographic bias in body waves towards the structure sampled by continental stations is clearly evident in earlier inferences on the uppermost and lowermost mantle. For example, arrival times predicted by the two widely used radial models PREM and AK135 differ by up to ∼5 s for teleseismic S and SKKS waves (Fig. 6). The early arrivals of S waves at short distances ($\Delta \leq 80^\circ$) with AK135 is due to v_S structure that differs from PREM by up to 2.75 % in the uppermost mantle and below the transition zone, potentially due to biased sampling of continental regions. Geographic bias also influences the average properties of deeper regions in the Earth's interior. PREM and AK135 predict arrival times of waves reflected from the CMB (ScS) or diffracted around the core (P_{diff}, S_{diff}) that differ by ∼1–2 s (Fig. 6). While almost all AK135 arrival times are in broad agreement with SP6 (±0.5 s), phases that bottom in the D″ region are an exception. Such discrepancies may be attributed to the biased sampling of the fast northern hemisphere in the lowermost mantle (e.g. Morelli and Dziewonski, 1993). Body-wave phases that graze the outer core (e.g. SKKS) or traverse the entire core (e.g. P′P′) are systematically slower (∼5–6 s) in AK135 than PREM due to stronger gradients and slower velocities in the outermost outer core broadly in agreement with SP6. Revised constraints from SP6 (Section 2.4) are employed in our inversions to account for the global average rather than geographically biased onsets of body-wave phases.

Global dispersion of fundamental-mode surface waves provide a more uniform constraint on the elastic structure of the uppermost mantle. Multiple techniques for measuring dispersion can be reconciled and afford a consistent picture of the anisotropic structure in the upper mantle (Moulik et al., 2022). Direct interpretation of average dispersion in terms of radial structure should be avoided due to theoretical considerations (Sections 3.2 and 3.3). After accounting for the effects of heterogeneity on the reference datasets, broad implications on radial structure become evident. PREM underestimates substantially the phase velocities of Rayleigh waves at periods shorter than 200 s (Fig. 4), potentially due to a bias towards the slower continental regions in earlier studies. Since Love waves at periods shorter than 125 s were not used in the construction of PREM, estimates of radial anisotropy in the shallowest mantle were poorly constrained and could only be parameterized as a monotonic function with depth in the upper 220 km of the mantle. Rayleigh-Love discrepancies in phase velocities (Fig. 4) and corresponding eigenfrequencies (Figs. 2 and 3) differ most substantially from PREM predictions at intermediate periods (∼40–50 s). This observation indicates that radial anisotropy peaks at a depth deeper than the Mohorovičić discontinuity (hereafter Moho) in PREM (24.4 km). All recent studies concur that PREM is inconsistent with eigenfrequencies of fundamental toroidal (Love waves) and spheroidal (Rayleigh waves) modes at periods longer than ∼250 s (${}_0S_l$, ${}_0T_l$ where $l < 58$), suggesting revision of structure in the deep mantle (depth ≥ 300 km).

Joint consideration of normal-mode eigenfrequencies and quality factors also inform expected (an)elastic deviations from earlier radial models. Our new reference dataset is broadly consistent with the limited quality factors employed in the construction of PREM. Newer normal-mode and surface-wave measurements were the motivation for other

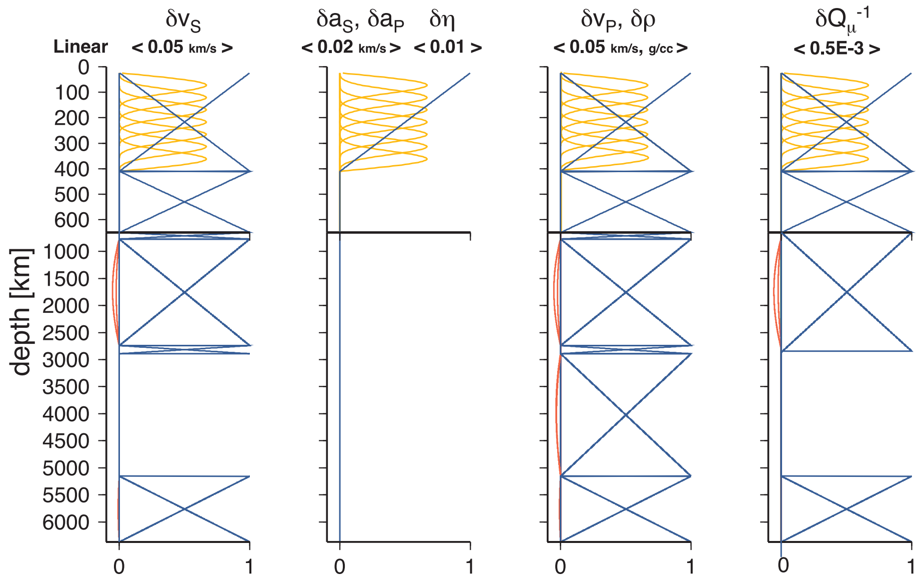

Fig. 5. Radial parameterization used in the construction of reference Earth models. Perturbations to our starting model are expressed in terms of basis functions (eq. 22). The model perturbations consist of combinations of 7 evenly-spaced cubic B-splines between 24.4 and 410 km and polynomials up to order $n = 4$ elsewhere in the Earth (Appendix A). The quartic polynomial term ($n = 4$) is employed only for density in the outer core to avoid artifacts in derivative properties (Section 4.1.4). Basis functions are colored according to various types: quadratic, cubic and quartic functions in red, cubic B-splines in yellow, and values at the top and bottom of a region in blue. A layered parameterization with boxcar functions is used for bulk attenuation (Q_κ) in various regions of the mantle and core. The perturbations for calculating numerical sensitivity kernels in Section 4.4, specified in $< \cdot >$, varies based on the physical parameter under consideration.

attenuation studies (Widmer et al., 1991; Durek and Ekström, 1996); recent normal-mode observations span a wider range of frequencies and overtone branches (Figs. 1–3; Supplementary Figs. S3–S19). Inverse quality factors of most surface-wave equivalent toroidal (${}_0T_l$, $l \geq 20$) and spheroidal fundamental modes (${}_0S_l$, $l \geq 46$) are higher than those predicted by PREM ($1000 \cdot \Delta Q^{-1} = 0.1$–$1.3$), suggesting stronger shear attenuation in the shallowest regions of the Earth. While trends in data afford broad implications for bulk Earth structure, disentangling the various effects necessitates joint inversions (Section 4).

3.2. Limits to the local-eigenfrequency approximation

Our reference normal-mode and surface-wave observations span a broad frequency range (0.3–40 mHz) that could transcend the validity limits of the local-eigenfrequency approximation. As discussed in Section 2.2.1, asymptotic limits that justify direct sensitivity of surface waves to local radial structure depend on the power spectrum of lateral heterogeneity in relation to the wavelength of an equivalent normal mode. We employ the crustal model CRUST2.0 (Bassin et al., 2000) and the mantle tomographic model S362ANI+M (Moulik and Ekström, 2014) to describe the heterogeneity spectrum. Our goal here is to restrict attention to the long-wavelength models of Earth's three-dimensional heterogeneity that are known with better precision and fidelity. If the approximation is found invalid with long-wavelength variations, any increase in the power of finer-scale structure reported using new seismic deployments is bound to restrict the validity even further. We evaluate the validity of this approximation by quantifying the extent to which sensitivity kernels to structure at various spherical harmonic degrees (K^s) can be approximated by their degree-zero counterparts ($K^s \simeq K^0$; Jordan, 1978).

First, it is clear that sensitivity kernels to structures at different wavelengths (or degree s) can vary dramatically for the low order (l), low-frequency normal modes. For example, lowest-frequency modes such as ${}_0S_2$ and ${}_0T_2$ have degree-0 and 2 sensitivities to v_S structure that are opposite in sign within the lower mantle (Fig. 7a). Predictions of frequency shifts of these modes from the elastic splitting function are therefore anti-correlated with those inferred from the local-eigenfrequency approximation (Fig. 8, Columns 1 and 2). Most tomographic models agree with S362ANI+M on the antipodal low-v_S structures beneath the Pacific Ocean and Africa that would be expressed as negative shifts in eigenfrequencies for modes ${}_0S_{2-8}$ with degree-0 kernels and the local-eigenfrequency approximation. However, observed frequency shifts of ${}_0S_2$ in the spectra of long-period seismograms are positive in these antipodal regions (e.g. Häfner and Widmer-Schnidrig, 2013; Deuss et al., 2013), consistent with low-v_S structures sampled by degree-2 sensitivity kernels. Positive (and negative) frequency shifts of up to 0.4 % in lowest-frequency modes therefore correspond to a decrease (and increase) in v_S, in contrast to the underlying assumptions in earlier studies (e.g. Silver and Jordan, 1981; Masters et al., 1982). It is worth noting that the magnitude of frequency shifts also constrains the positively buoyant region ($\mathrm{dln}\rho \simeq \pm 0.5$ %) that is anti-correlated with v_S variations in the bottom ~500 km of the mantle (Moulik and Ekström, 2016).

Second, validity of the local-eigenfrequency approximation can be quantified based on a 'local threshold' parameter, which we define as

$$\varkappa_{\mathrm{thres}} = \frac{\omega_0}{\sigma} \int_{\Omega} \left| F_E(\theta, \phi) - F_E^{\mathrm{local}}(\theta, \phi) \right| d\Omega, \tag{21}$$

where ω_0 is multiplet eigenfrequency predicted by the radial reference model, F_E is the even-degree elastic splitting function (eq. 7), F_E^{local} are values from the local eigenfrequency approximation (eq. 9) and $d\Omega$ is the differential surface area on the unit sphere. Note that the values are normalized by the uncertainty (σ) in mode eigenfrequency (Section 2.2). For this synthetic measure, both F_E and F_E^{local} are calculated till the maximum degree $s = 2\,l$ (e.g. eq. 9). A local threshold value $\varkappa_{\mathrm{thres}} > 1$ corresponds to a mean discrepancy in eigenfrequency between the theoretical assumptions that exceeds the measurement uncertainty and thereby influences significantly the residual variance in tomographic inversions.

Fig. 8 shows the values of F_E, F_E^{local} and $\varkappa_{\mathrm{thres}}$ for several spheroidal and toroidal modes. Local thresholds are substantial ($\varkappa_{\mathrm{thres}} \geq 20$) for the modes ${}_0S_{2-3}$ and ${}_0T_{2-3}$ and the local-eigenfrequency approximation is clearly invalid at the longest periods of vibration. At the shortest periods (T ~ 25 s), $\varkappa_{\mathrm{thres}}$ is zero to within numerical precision, demonstrating the applicability of JWKB and local-eigenfrequency approximations for analyzing these surface-wave observations (e.g. as equivalent modes ${}_0S_{234}$ and ${}_0T_{254}$). Local threshold value $\varkappa_{\text{thres}} = 1$ is crossed at an intermediate period of around 120 s for Love (${}_0T_{76}$) and 220 s for Rayleigh waves (${}_0S_{38}$, Fig. 7). Toroidal modes are more sensitive than spheroidal modes to the shallower crustal structure that has stronger power at shorter wavelengths (high s) compared to the underlying mantle model (degree 18). Asymptotic limits for normal modes ($l \gg s$) and the local-eigenfrequency approximation ($K^s \simeq K^0$) are strictly valid at higher frequencies (and angular orders) in toroidal (Love waves) than in spheroidal modes (Rayleigh waves). Substantial geographic variations are evident with discrepancies between F_E and F_E^{local} that cancel out along certain paths (e.g. Hawaii to South Pole for ${}_0S_2$, Fig. 8); $\varkappa_{thres}$ therefore represents the upper bound on the discrepancy that a traveling wave could accrue globally. Our non-linear formulations for correcting eigenfrequency (eq. 11) or phase velocity (eq. 18) for crustal effects, which also assume the validity of this approximation, are strictly valid only for fundamental-mode Love waves below 120 s and Rayleigh waves below 220 s. Note that these are optimistic and upper bounds on the validity limits since only the long-wavelength variations in the crust and mantle are being considered.

3.3. Non-linear effects of crustal structure

At frequencies where the local-eigenfrequency approximation is valid, phase of a propagating wave may be attributed solely to the local radial structure that the wave encounters along the ray path. If the relationship between local phase velocity and lateral structural variations is sufficiently linear, it can be modeled in terms of perturbations to the average global model using first-order perturbation theory (e.g Woodhouse and Girnius, 1982; Dahlen and Tromp, 1998) instead of solving for exact mode catalogs beneath every point (e.g. Boschi and Ekström, 2002; Nettles and Dziewonski, 2008). We perform several experiments to assess whether the strong crustal variations could influence the average dispersion in a significantly non-linear fashion. Fig. 9 shows the local phase-velocity perturbations of 35 s and 60 s Love and Rayleigh waves for PREM overlain by three-dimensional crustal structure from CRUST2.0 (Bassin et al., 2000). The phase-velocity maps exhibit a clear correlation with crustal variations; fast phase velocities are associated with the thin, fast oceanic regions while slow velocities are correlated with thick, slow continental crust in the Andes and Tibetan plateau. The phase velocities of 35 s Love waves show stronger deviations from PREM velocities (down to −12 %) than Rayleigh waves due to their stronger sensitivity to crustal structure. Global deviations of Love wave phase velocities decrease two-fold from 0.34 % at 35 s to 0.15 % at 60 s period due to the reduced sensitivity to crustal structure at longer periods (Supplementary Fig. S2).

Fig. 10 summarizes the average deviations in phase velocities from PREM across all available frequencies and wave types. These values are obtained from the spherical average of phase velocity maps (i.e. < · > in Fig. 9). Contributions of crustal structure to Love-wave dispersion curves increase monotonically with frequency and are up to 1.5 times the observed signal at periods shorter than 40 s (Fig. 10a). The influence of water depth in oceanic basins coupled with the deeper sensitivity of

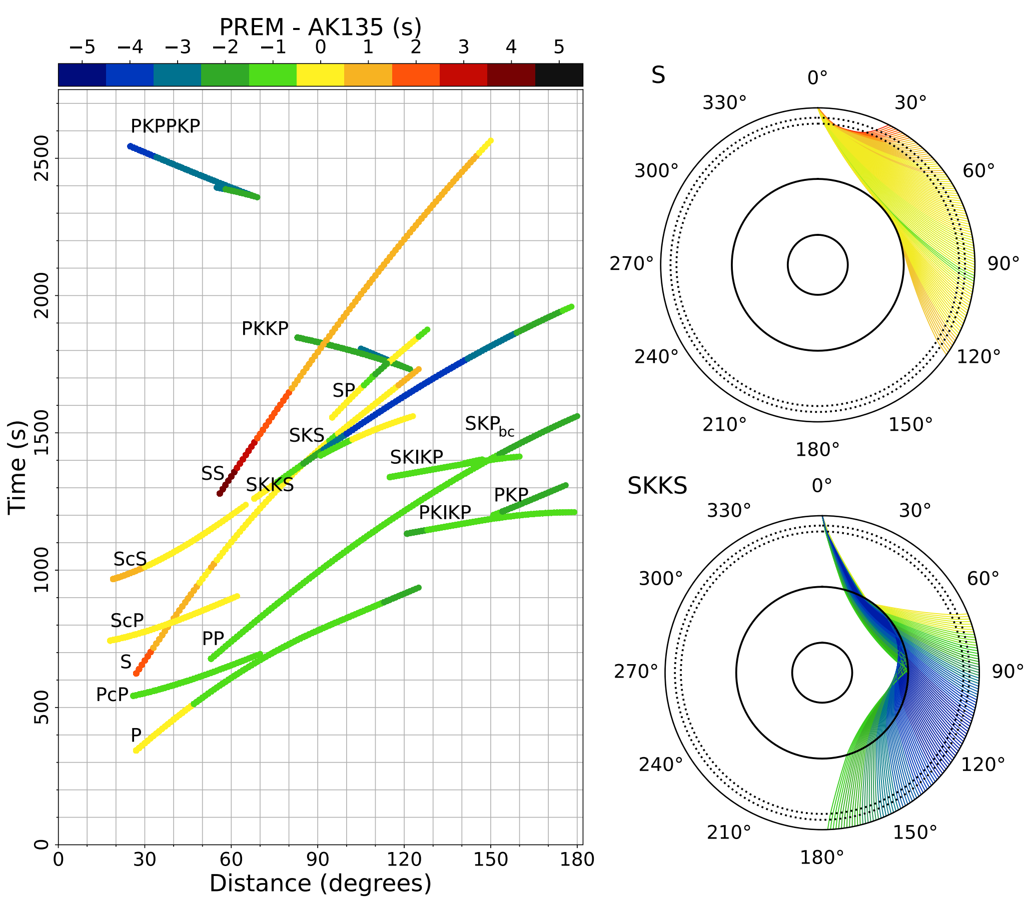

Fig. 6. Arrival-time curves of various mantle and core body phases. Arrival times are calculated from anisotropic PREM at every 1° distance and colored according to values relative to the isotropic model AK135. Red colors denote slower velocities (greater arrival times) and blue colors denote faster velocities (smaller arrival times) than AK135. The source is a surface-focus earthquake located at the equator (0°, 0°) and no ellipticity correction is applied. A modified version of an anisotropic ray tracer (Section 2.4; Woodhouse, 1981) is employed; the phases S, SS and ScS are measured on the transverse component and others on the vertical component (Table 2).

Rayleigh waves leads to substantial crustal contributions even at intermediate periods longer than 40 s. Crustal contribution to the average phase velocity of 60 s Rayleigh waves (0.54 %) is, in fact, three-fold greater than those at 35 s (0.17 %). Due to the strong agreement on average dispersion (Section 2.3), crustal contributions are often ~2–5 times the estimated uncertainties and are significant above the 99 % confidence level. Overall, the crustal contributions to globally averaged phase-velocity perturbations are substantial and often comparable to the observed deviations from the PREM dispersion curves. Both CRUST2.0 and the finer-resolution CRUST1.0 (Laske et al., 2013) show average perturbations that are similar to within ±0.05 % for both Love and Rayleigh waves between 4 and 40 mHz. Non-linear contributions to reference datasets and radial structure are largely independent of the crustal model and depend primarily on the large-scale variations in Moho depth that is relatively well constrained with diverse datasets. Our results extend the application of nonlinear crustal corrections (e.g. Kustowski et al., 2007; Lekic et al., 2009) to the direct modeling of radial structure. In case of the available quality factor observations, the non-linear contributions from a crustal layer with uniform shear attenuation ($Q_\mu = 300$) and variable Moho depth from CRUST2.0 are typically smaller than the uncertainties in available data (Fig. 10b). Crustal contribution to quality factors may be substantial for Love waves shorter than 50 s but no systematic measurements of global attenuation have been made at these short periods to date.

Observations of average dispersion can lead to divergent interpretations of radial structure based on whether crustal contributions are considered. Classical approaches based on first-order normal-mode perturbation theory suggest that the reported deviations in phase velocity or eigenfrequency can be attributed directly and linearly to changes required in PREM. Linear contributions from the crust can be readily evaluated as they are only sensitive to differences between PREM and the average structure of CRUST2.0 (Fig. 10a). Linear crustal contributions are expected to show a roughly monotonic variation since displacements and resulting sensitivities in the crust become progressively stronger with frequency, which are inconsistent with the reference dataset. Considering the non-linear effects of the crust has a perceptible and often dramatic effect on the inferences of radial structure. For example, linear assumptions might suggest that high velocities for short period Love waves ($\geq$ 30 mHz) is indicative of a crust that is thinner on average than in PREM (Ekström, 2011). However, non-linear crustal contributions are comparable or even stronger than the observed signal at these periods, which suggests that no major changes to the Moho depth in PREM are required (Fig. 11). Similar comparisons for Rayleigh waves suggest that the bulk (> 50 %) of the average phase velocity perturbations at long periods (50–100 s) can be attributed to non-linear effects from the crust. Corrected eigenfrequency perturbations indicate that the average v_{SV} (and v_{SH}) structure in the shallowest mantle is likely faster (and slower) than PREM (Fig. 11). We therefore account for the non-linear crustal contribution to degree-0 terms of phase velocity maps and normal-mode eigenfrequencies (eqs. 11 and 18) before inversions are performed for radial structure.

4. Influence of inverse modeling choices

In previous sections, we outlined forward modeling concepts that account for the effects of lateral heterogeneity on reference bulk Earth datasets. Construction of a radial model involves the inverse modeling of datasets for a description of average properties. We now explore the concepts of parameterization, starting model, regularization and sensitivity kernels, which are optimized for rapid convergence and benchmarked against classical approaches.

4.1. Prior information in the parameterization

A radial model $\oplus$ can be expressed as a linear combination of analytical basis functions that vary within 10 principal regions of the Earth (Fig. 5). The starting radial reference model can be written as

$$\oplus_0(r) = \sum_h c_h^{m_k} B_h(r), \tag{22}$$

where $c_h^{m_k}$ corresponds to the coefficient for the h-th function from the basis set and the k-th seismological parameter m_k (e.g. density, velocity). A polynomial parameterization was adopted by the early tomographic studies of radial Earth structure (Dziewoński et al., 1975) and later used in constructing PREM based on suggestions by the Standard Earth Model Committee of the I.U.G.G (e.g. Hales et al., 1974). In the sections below, we discuss and justify changes to classical parameterization schemes based on our experiments and the current geophysical knowledge.

4.1.1. Finer details in the upper mantle

A detailed parameterization in the upper mantle is informed by recent studies that demonstrate the improved resolution of elastic (e.g. Kustowski et al., 2008) and anelastic structure (e.g. Romanowicz, 1995; Selby and Woodhouse, 2000; Dalton et al., 2008) owing to new and expanded datasets. While we adopt a polynomial basis in most principal regions, our upper mantle (24.4–410 km) consists of a linear polynomial and 7 evenly spaced cubic B-splines (Appendix A). Since the 220-km discontinuity appears not to have a global extent (e.g. Gu et al., 2001), we have chosen a smooth and more detailed parameterization in the shallowest 410 km of the mantle (Fig. 5). The cubic B-splines provide a basis set with compact support like boxcar or multi-layer parameterizations (e.g. Widmer et al., 1991; Durek and Ekström, 1996), but are more advantageous since they have continuous first and second derivatives.

While high bulk attenuation in the asthenosphere (80–220 km depth) was reported by Durek and Ekström (1995), we have chosen to adopt a parameterization that permits only constant bulk attenuation throughout the upper mantle (24.4–410 km) as additional complexity with cubic B-splines is presently unjustified. Due to anelastic dispersion, a discontinuity in bulk attenuation at 220 km depth in QL6 leads to a minor discontinuity for compressional waves at periods other than the reference period (1 s), a complexity that has not yet been observed globally in recorded waveforms. An evaluation of high bulk attenuation restricted to the asthenosphere (e.g. Durek and Ekström, 1996) that does not manifest as a discontinuity for elastic parameters is beyond the scope of this study. The 220-km discontinuity is therefore summarily excluded from all physical parameters in our radial models.

4.1.2. Revised mantle discontinuities

Several adjustments are made to the parametrization in the mantle transition zone (410–650 km) based on recent observations. We remove a second-order discontinuity defined in PREM at 600 km depth, in agreement with the choice made by several studies (e.g. Kennett et al., 1995; Morelli and Dziewonski, 1993; Kustowski et al., 2008). Based on mineral physics, it is known that phase transformations in the transition zone are not univariant and can occur over a range of depths. The olivine to wadsleyite phase transformation at 410 km depth is about 10 km thick (Akaogi et al., 1989; Katsura and Ito, 1989) while the garnet-to-perovskite transformation at 650 km is about 50 km thick (Akaogi et al., 2002; Hirose, 2002). Our parameterization does not permit phase boundaries over a range of depths based on purely seismological considerations; precursor body-wave phases reflected from such boundaries cannot be traced through our models and their amplitudes detected above the noise level if the impedance contrasts extend over a region exceeding ~5 km in thickness.

Our parametrization in the lower mantle follows closely the polynomial coefficients adopted in PREM. We retain the second-order discontinuity at 771 km in the lower mantle, which corresponds roughly to the depth where transitions of all upper mantle minerals (olivine, enstatite, and garnet) to their high-pressure polymorphs

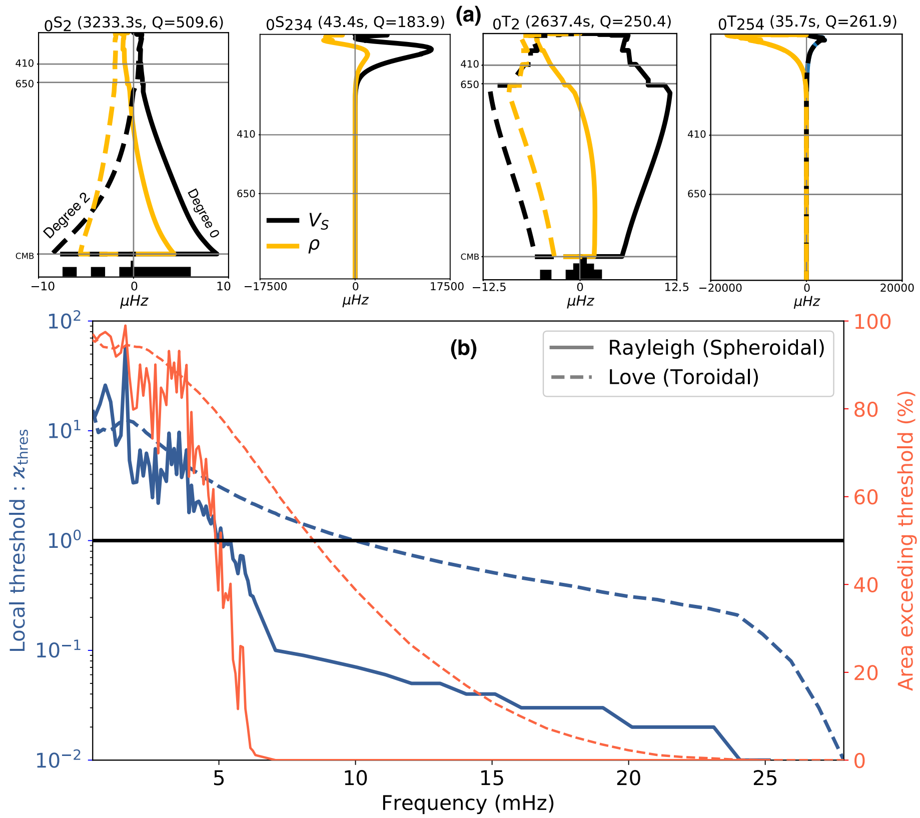

Fig. 7. Nature of sensitivity kernels and related limits for the local-eigenfrequency approximation. (a) Sensitivity kernels of the normal modes ${}_0S_2$, ${}_0S_{234}$, ${}_0T_2$ and ${}_0T_{254}$ to the degree $s = 0$ (solid) and $s = 2$ (dashed) variations in density (ρ, yellow) and Voigt-averaged shear velocity (v_S, black). Depth of the 410-km and 650-km discontinuities and the core-mantle boundary (CMB) are indicated by grey horizontal lines. For ${}_0S_2$, and ${}_0T_2$, horizontal bars beneath the velocity kernels show from top to bottom, the mode's sensitivity to topographic perturbations of the 410 and 650-km discontinuities and the CMB (K^s_{410}, K^s_{650} & K^s_{CMB}). Note that the kernels are calculated using PREM, are in units of μHz and correspond to variations in physical parameters ($\delta m_i/m_i$) or topography ($\delta h/a$) of 1 %, where a=6371 km and that each graph is scaled independently. (b) Discrepancies in structural sensitivity owing to the local eigenfrequency approximation exceeds measurement uncertainty when $\varkappa_{\text{thres}} > 1$ on average (blue curves) and in more than 50 % of the Earth's surface area (red curves). This is the case for fundamental spheroidal modes at periods above 220 s (e.g. ${}_0S_l$, $l \leq 38$) and fundamental toroidal modes above 120 s (e.g. ${}_0T_l$, $l \leq 76$).

(perovskite, ferropericlase, and calcium perovskite) are completed (e.g. Stixrude and Lithgow-Bertelloni, 2011). The steep velocity gradients in this region can therefore be considered an extension of the mantle transition zone. Another second-order discontinuity at a depth of 2741 km is adopted from PREM based on earlier definitions of a D″ layer (Bullen, 1949), which corresponds roughly to the bridgmanite to post-perovskite phase transition (e.g. Murakami et al., 2004).

4.1.3. Allowing detection of iron spin transitions

Recent tomographic studies with strong sensitivity to the mid-mantle agree on the weakness of heterogeneity in the central lower mantle (CLM, 771–2741 km; e.g. Ritsema et al., 2011; Moulik and Ekström, 2014). Radial variations in the CLM region follow smooth velocity gradients, consistent with a close-to-adiabatic thermal gradient and self-compression of the relatively stable bridgmanite over a large range of pressures. The CLM region corresponds to conditions where a transition in the electronic spin state of iron in bridgmanite and ferropericlase is expected to occur based on *ab initio* calculations and laboratory experiments though the size and radial (or pressure) extent of this phase transition remain debated (e.g. Badro et al., 2003; Tsuchiya et al., 2006; Wentzcovitch et al., 2010; Badro, 2014). Localized features in absolute properties (v_P, v_S and density) that are diagnostic of spin transitions can be permitted though parameterization choices e.g. adding cubic B-spines and higher-order polynomials or by adopting a pair of polynomials split across a second-order discontinuity. However, incorporating such complexity in our parameterization cannot be currently justified based on three considerations. First, the *a posteriori* fits to reference datasets of body waves and normal modes that are sensitive to the CLM region are excellent with the cubic polynomials for elastic structure (Paper II). Second, splitting the CLM region *a priori* in our inversions would involve prescribing the depth of a second-order discontinuity that cannot be justified based on the trends ($dt/d\Delta$) in global datasets like arrival times (t) of mantle waves (e.g. P, S) that bottom in this region ($\Delta = 52°$–$68°$). Third, emerging mineralogical studies report complicating factors such as temperature, composition and partitioning of iron between bridgmanite and ferropericlase, which may lead to a more suppressed and broadened signature of iron spin transitions in the real Earth than estimated in the laboratory for single mineral phases (e.g. Speziale et al., 2005; Caracas et al., 2010; Irifune et al., 2010).

A derivative property of interest for detecting spin transitions is the gradient of modulus ratio (μ/κ) as a function of scaled pressure (p/κ), since a linear relationship is expected in regions with uniform phase and composition (e.g. Falzone and Stacey, 1980; Burakovsky et al., 2004; Kennett, 2021). Spin crossovers in the lower mantle are expected to manifest as a smooth (second-order) phase transition that modifies the pattern with distinct linear μ/κ segments on either side of the transition region. Kennett (2021) has interpreted the mild change of μ/κ gradients (1300–1750 km depth) in the body-wave model AK135 that is parameterized with linear gradients as a signature of the iron spin transition. Additionally, this study claimed that the null detection of a μ/κ signature in PREM was due to the inherent limitations of data and the polynomial parameterization employed in its construction. Fig. 12 demonstrates that adopting a cubic polynomial parameterization does not preclude localized μ/κ changes in the CLM region. Minor reductions (~1–2 %) to

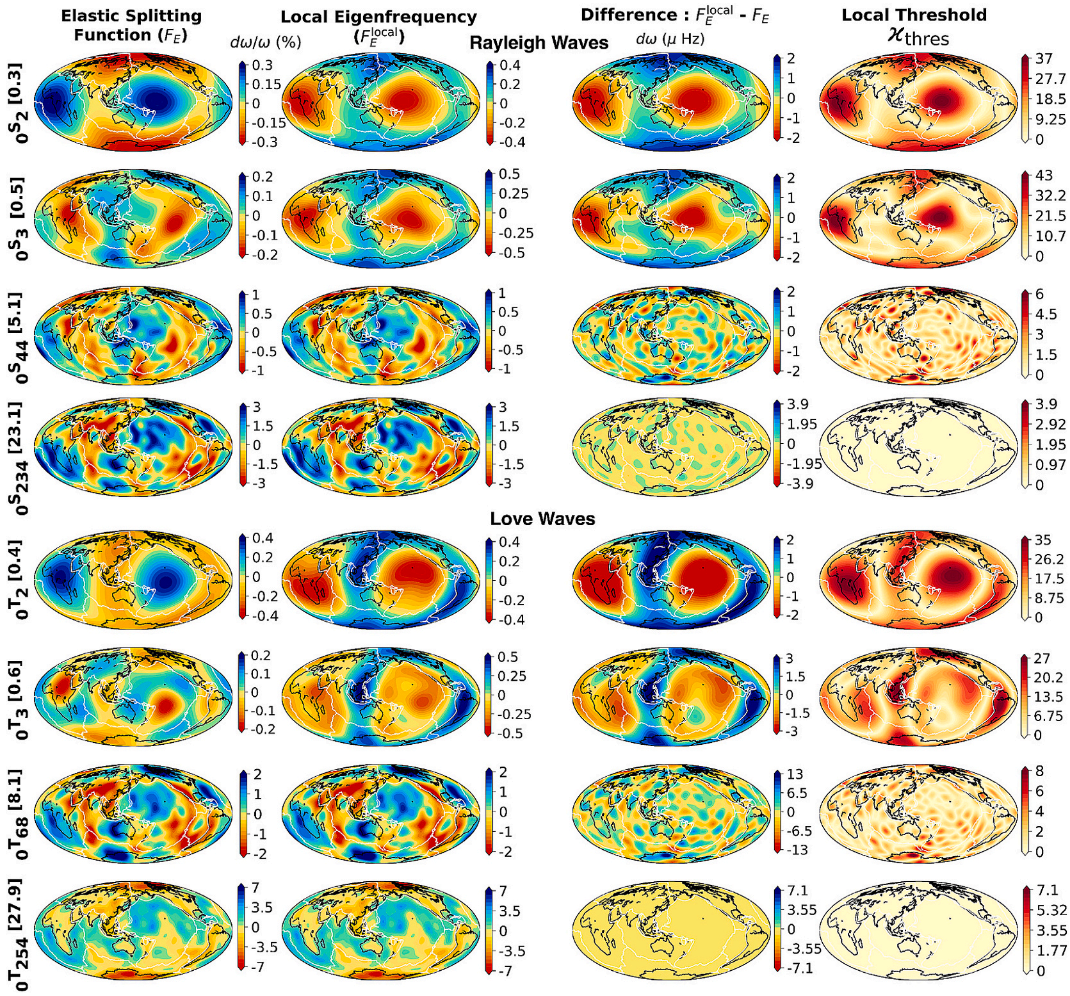

Fig. 8. Limits of the local eigenfrequency approximation for traveling waves using crustal model CRUST2.0 and mantle model S362ANI+M accounting for the topography at the 410- and 650-km discontinuities. Each row corresponds to a normal mode with its eigenfrequency provided within [·] in mHz. Predicted splitting function (Column 1, F_E, eq. 7) accounts for the finite-frequency effects of even-degree lateral heterogeneity on propagating waves while local eigenfrequencies (Column 2, F_E^{local}, eq. 9) assume ray-theoretical sensitivity solely to local radial structure. Also provided are the absolute differences (Column 3) between the two approaches (in μHz). Local eigenfrequency approximation is less valid when local threshold $\chi_{\mathrm{thres}} \geq 1$ (Column 4) on average and in more than 50 % of the Earth's surface area (e.g. $_0S_2$, $_0T_2$). Note that these calculations ignore the effects of Earth's hydrostatic ellipticity; such contributions will not influence the difference in synthetics discussed here.

the polynomial coefficients for velocity structure in PREM are adequate to capture the μ/κ variations in AK135 and a parameterization in terms of linear gradients or layers is not required. Although cubic polynomials are employed in our v_P, v_S and density variations, relative differences in their gradients permit localized derivative features to emerge that are similar in amplitude to those interpreted in past studies as signatures of spin transitions (e.g. Kennett, 2021). Feasibility for the detection of spin transitions in radial Earth models with reference datasets is discussed further in Section 4.4 of Paper II.

4.1.4. *Avoiding artifacts in derivative properties*

Properties derived from radial reference models such as the Bullen's stratification parameter η_B are strongly sensitive to deviations from adiabicity and homogeneity. Fig. 13 summarizes our experiments with polynomials of various orders using the elastic structure from SP6 and PREM. If the density gradients follow the Adams-Williamson equation $\left(d\rho/dr = -\rho^2 g/\kappa\right)$, the predicted density profile will have associated η_B values of 1 throughout the outer core. However, full complexity of such a density profile needs to be captured by our parameterization since artifacts can be wrongly attributed to changes in phase, temperature or composition. It is readily apparent that a polynomial of at least order n+1 may be needed for density if the coefficient of order n in v_P (or κ) structure in a fluid region ($v_S = 0$) is sufficiently large; this choice allows the gradient of density ($d\rho/dr$) to also have a maximum order of n and thereby satisfy the Adams-Williamson equation to greater precision. Both SP6 and PREM have a sufficiently large gradient and curvature of v_P in the outer core such that the predicted density profiles cannot be adequately fitted with cubic polynomials (Fig. 13a). The small yet mineralogically and dynamically significant deviations of η_B from one in the PREM outer core (3 %; $\eta_B = 1 \pm 0.03$) are artifacts from using polynomials of the same order for both elastic and density structure. In order to reduce the artifact from parameterization to within a range of uncertainty expected from current mineral physical knowledge ($|\eta_B - 1| < 0.005$), we add a quartic polynomial ($n = 4$) in the outer core and a cubic polynomial ($n = 3$) in the inner core to the density parameterization of PREM. Previous uncertainty bounds on the η_B parameter (i.e. 2 %; Masters, 1979) based on resolving power theory (Backus and Gilbert, 1968, 1970) are biased high since they did not include the new reference datasets or account for the artifacts of a polynomial parameterization.

It is worth noting that a polynomial parameterization does not automatically introduce spurious, inflexible and physically implausible

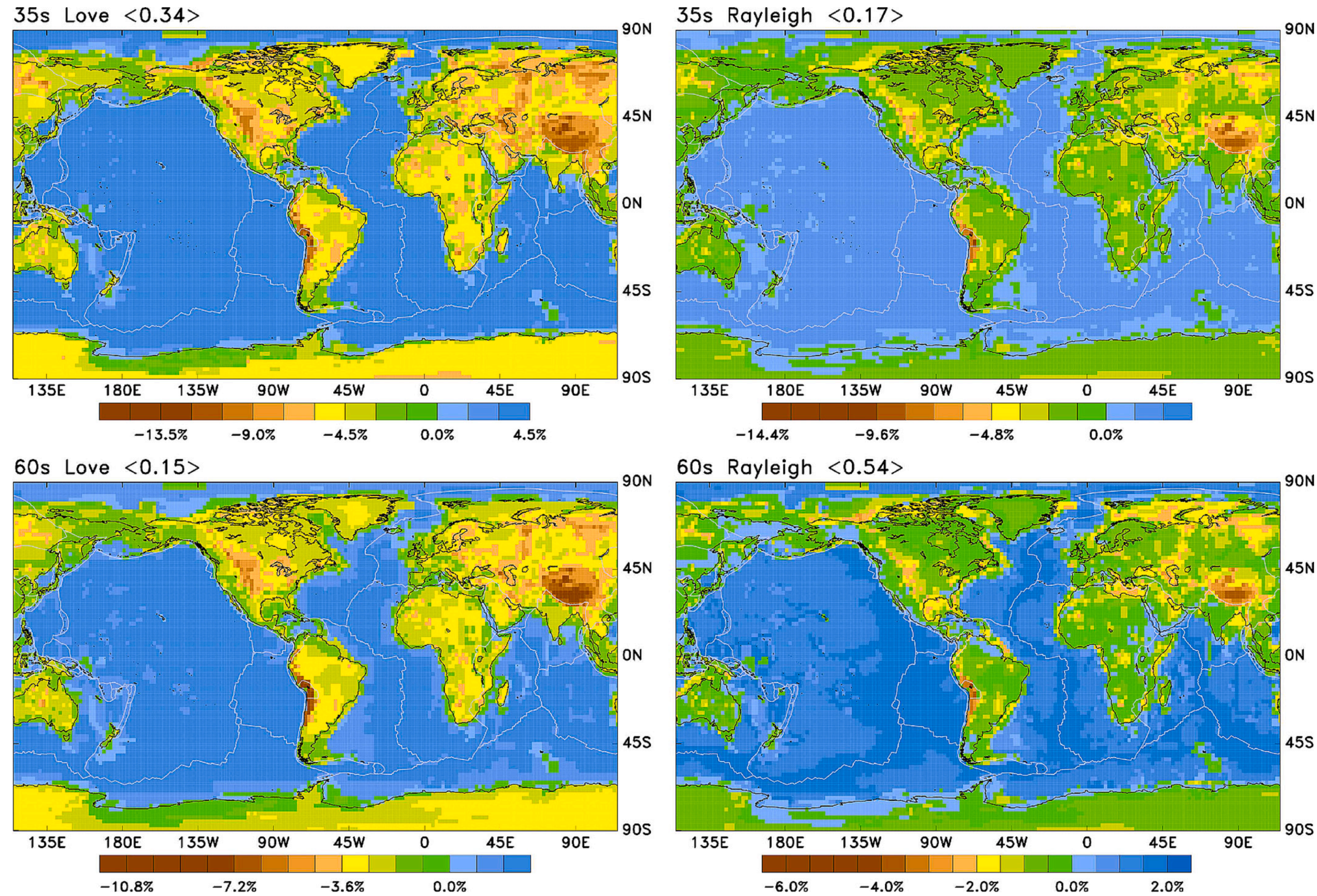

Fig. 9. Crustal phase velocity perturbations (dc/c) for Love and Rayleigh waves at 35 and 60 s. Local eigenfrequencies and phase velocities are calculated from PREM overlain by crustal structure CRUST2.0 (Bassin et al., 2000). Average values at each period, as specified in $< \cdot >$, has been used to construct the dispersion curve in Fig. 10 (solid curves).

structure as has been suggested by some studies (e.g. Stacey, 2005; Kennett, 2021). Polynomial terms in our inversion are informed by mineral physics and reference datasets ultimately dictate whether the final radial reference model conforms to such expectations. There is no apparent need to invoke interpretative assumptions on the specific EoS formulation (e.g. Birch, 1947; Vinet et al., 1987; Stacey, 1995) or estimates of molar mass, pressure and gravity in the outer core (e.g. Irving et al., 2018). On the issue of parameterization, the elastic and density variations in the outer core predicted by these EoS formulations are decidedly smooth and can be fitted to within 0.01 % using polynomials up to order 4 or 5. Polynomial parameterization is also justified based on the principle of parsimony that prefers the model with least complexity that can fit the reference datasets (e.g. Constable et al., 1987; Malinverno, 2002; Charléty et al., 2013). Models based on linear gradients and layers (e.g. AK135) afford neither uniformly better fits to seismological datasets nor more flexible constraints on derivative properties (e.g. η_B, gradients in μ/κ) than models constructed with a few polynomial functions.

4.2. Prior information in the starting model

In the following sections, we discuss and justify features of our starting radial model (START, Fig. 14) based on our experiments and insights from the literature.

4.2.1. Starting constraints on the absolute variations

Due to historical reasons and owing to the limited direct sensitivity from the datasets in this study, crustal elastic parameters, density and Moho depth from PREM are retained. However, shear attenuation in the crust is modified ($Q_\mu = 300$) following Durek and Ekström (1996). Coefficients for cubic B-splines in the upper mantle are set to zero in the starting model and linear parameters are set to a constant value that corresponds roughly to the average estimate from PREM. The shear and compressional velocities in the lower mantle (650–2891 km depth) are made compatible with SP6 to allow faster convergence to summary arrival-time curves (Section 2.4). The starting density model in the central lower mantle (771–3891 km depth) and D″ region closely resembles PREM, which was derived using a variation of the method proposed by Birch (1964).

Applying the condition that inner and outer cores are at hydrostatic equilibrium and follow the Adams-Williamson equation, density at the top of outer core $\left(\rho_{OCO}^{top}\right)$ is reduced from 9.90349 g/cm^3 in PREM to 9.89526 g/cm^3 (Fig. 13). The ρ_{OCO}^{top} parameter is optimized to fit the astronomic-geodetic data (Table 1) using the downhill simplex method (e.g. Nelder and Mead, 1965). Since radial modes provide sensitivity to bulk attenuation based on the expansion and contraction of the Earth, we incorporate constraints from Durek and Ekström (1996) to achieve faster convergence in fits. For the starting model, a fixed and finite bulk attenuation ($Q_\kappa = 28{,}000$) is adopted in the mantle while no bulk attenuation is prescribed elsewhere ($Q_\kappa = 88{,}888$ denoting infinity within numerical precision). This choice gives significantly better data fits (up to 6 times lower χ^2/N) and faster convergence for quality factors and eigenfrequencies of radial modes (Section 2.2) without deteriorating substantially the fit to other datasets.

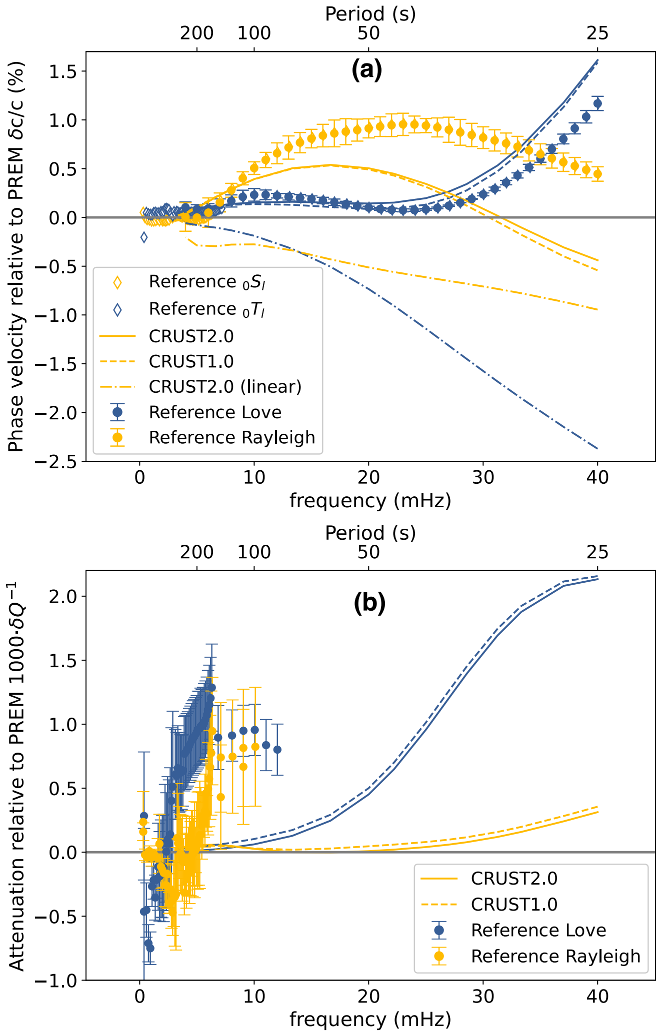

Fig. 10. Global averages of perturbations in phase-velocity ($\delta c/c$, a) and attenuation $\left(1000{\cdot}\delta Q^{-1}\right.$, b) for Love (in blue) and Rayleigh waves (in yellow) between 4 and 40 mHz. Reference data and uncertainties from Section 2 are plotted as dots with error bars while non-linear (or linear) crustal contributions are provided as solid (or dot-dashed) curves. Average non-linear crustal perturbations (solid curves) are obtained from phase velocity and attenuation maps derived using PREM overlain by CRUST2.0 (Fig. 9, eq. 14) or CRUST1.0 (dashed curves). All calculations assume a constant shear attenuation in the crust ($Q_\mu = 300$). The crystalline crust in CRUST1.0 is expanded everywhere to match the average thickness in PREM (21.4 km). Linear contributions from the crust are only sensitive to differences between average structure of CRUST2.0 and PREM (dot dashed, a). Non-linear contributions are comparable to or exceed the uncertainty in phase-velocity measurements, in contrast to the quality factors where the uncertainties are much larger (b). All perturbations reported here are calculated relative to values obtained from PREM. A zoomed-in version of this figure for frequencies up to 15 mHz is provided as Supplementary Fig. S21.

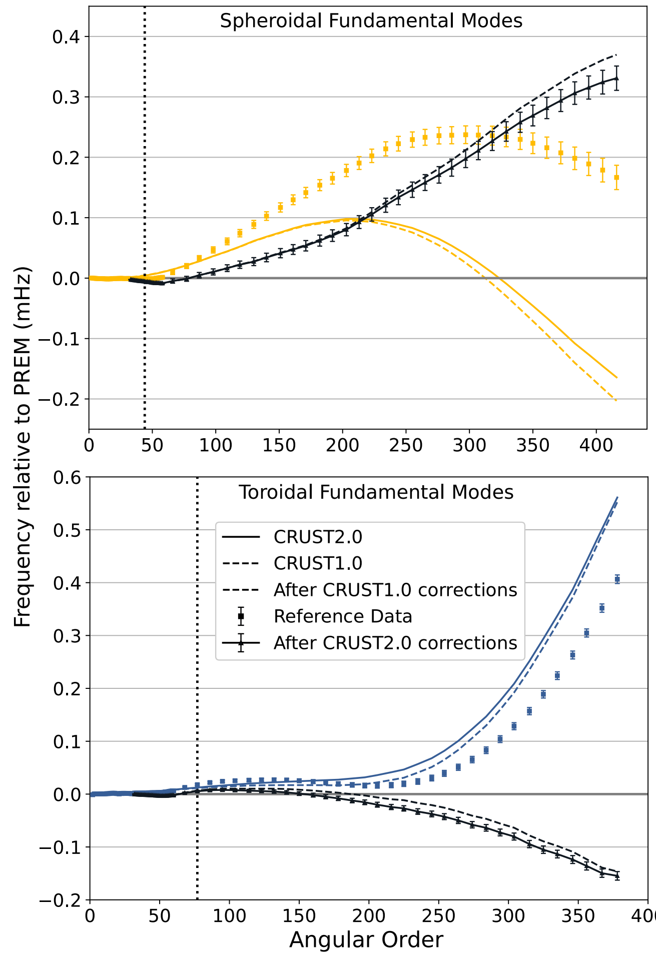

Fig. 11. Non-linear crustal corrections to the eigenfrequencies of fundamental spheroidal and toroidal modes. Non-linear contributions from CRUST2.0 (solid colored curves) and CRUST1.0 (dashed colored curves) are obtained using eq. 13 and are similar. The corresponding data after crustal corrections (black) are indicative of the modifications needed to the mantle structure in PREM. Dashed vertical lines denote the limits of local-eigenfrequency approximation (Fig. 7). These are the threshold angular orders above which the waves are of a sufficiently short wavelength that non-linear crustal corrections can be applied (i.e. $_0S_{l>38}$, $_0T_{l>76}$). All perturbations reported here are calculated relative to values obtained from PREM.

4.2.2. *Starting constraints on the discontinuities*

Several discontinuities in the Earth are modified to account for the recent literature on the mean depths and contrasts in physical parameters across boundaries. Velocity and density contrasts in the transition-zone discontinuities of our starting model are adjusted to fit best estimates from global studies of long-period seismograms (Section 2.5, Table 3). Contrasts in the starting model are identical to PREM at the 410-km discontinuity ($\%\Delta v_S = 3.4$, $\%\Delta v_P = 2.5$, $\%\Delta\rho = 5$) and similar to AK135 at the 650-km discontinuity ($\%\Delta v_S = 6.1$, $\%\Delta\rho = 5.3$) albeit with a slightly reduced contrast for compressional waves ($\%\Delta v_P = 2.5$, $\%\Delta Z_P = 7.8$). Radius of the inner core is reduced by 6 km from PREM to 1215 km based on PKIKP travel times from body-wave studies (e.g. Morelli and Dziewonski, 1993). Our choice of an inner core radius is broadly consistent with several other body-wave (Kennett et al., 1995; Dziewoński et al., 1975; Souriau and Souriau, 1989) and normal-mode studies (e.g. de Wit et al., 2014). At the inner-core boundary, shear-velocity contrasts in our starting model (Table 3) are obtained from SP6 ($\Delta v_S = 3.5$ km/s) and density contrasts from PREM ($\Delta\rho = 0.6$ g/cm^3), values broadly consistent ($\pm 2\sigma$) with recent normal-mode (e.g. Masters and Gubbins, 2003) and body-wave studies (e.g. Koper and Dombrovskaya, 2005).

4.2.3. *Starting constraints on gradients in the core*

A reasonable *a priori* expectation is that the outer core is well mixed and is composed of iron and lighter alloying components (e.g. Birch, 1964; Bloxham and Jackson, 1991). While adopting higher-order polynomials for density can help prevent artifacts in the Bullen's stratification parameter (Section 4.1), it does not alleviate concerns regarding the gradient of bulk modulus with pressure ($\kappa' = d\kappa/dp$). While average values of the derivative parameter κ' in PREM are largely valid, its curvature ($\kappa'' = d^2\kappa/dp^2$) undergoes a reversal in sign within the outer core (Fig. 13d). Based on EoS predictions of a well-mixed isochemical outer core (e.g. Stacey, 2005), the curvature κ'' should remain negative over an entire pressure range, decreasing in magnitude to zero at high pressures ($p \rightarrow \infty$). We remove this anomalous κ'' feature of PREM from our starting model START by damping the third derivative (R_t) of ρ and v_P variations (Appendix A, Table A.1). Velocities in the inner core are also modified from SP6 in order to give expected variations in κ'' while satisfying the arrival time dataset of core-sensitive body waves (e.g. PKKP, PKIKP, P′P′) to within ~0.3 s (Section 2.4, Table 2). Applying this κ'' constraint in the core does not change the fits to most subsets of the reference dataset; only the χ^2 fits to the eigenfrequencies of radial modes deteriorate by a factor greater than 1.2, which is not statistically significant for the number of effective parameters in our inversions (e.g. Hastie and Tibshirani, 1990).

4.3. Regularization and model complexity

We relate reference datasets $\mathbf{d}$ to the model vector $\mathbf{m}$ containing perturbations to our starting model using linearized sensitivity kernels ($\mathbf{Gm} = \mathbf{d}$) based on the formulations in Section 2. Due to imperfect data coverage and measurement errors, and in order to stabilize the inversion, we regularize the inversions by minimizing data misfit and specific characteristics of the radial model. Overall objective of our inversions is to minimize the quantity

$$\tilde{\chi}^2 = \chi^2 + \gamma_g R_g^2 + \gamma_c R_c^2 + \gamma_t R_t^2 + \gamma_n R_n^2 + \gamma_d R_d^2 + \gamma_s R_s^2, \tag{23}$$

where χ^2, γ_g, γ_c, γ_t and γ_n are the total data misfit, and weights to modulate the gradients, curvature, third-order derivatives and norm, respectively (Appendix A). The weight γ_d helps modulate the step change in density and velocity (i.e. contrast in %) across first-order discontinuities, such as in the transition zone (410 and 650 km) and the inner core boundary, to closely match the reference dataset (Table 3). This term is also used to impose a second-order discontinuity such as at the depth of 771 km in the lower mantle (Section 4.1). In order to modulate model perturbations in the uppermost mantle where more structural detail can be recovered, additional depth-dependent weights (W) for gradient and norm damping are used in four distinct regions (24.4–80, 80–250, 250–330, 330–410 km). For all parameters, gradients and norm of perturbations are damped strongly in the deepest region of the upper mantle (330–410 km) since data sensitivities deteriorate and no additional data variance can be explained with more structural complexity. A complete list of damping parameters used in REM1D construction (Paper II) is provided in Table A.1 and discussed in Appendix A.

We perform standard damped least-squares inversions and select an appropriate amount of damping for every principal region in the Earth. The optimal damping scheme is adjusted separately for different physical parameters after successive trials and evaluation of our results. Several persistent features emerge that are largely independent of the choices on damping. For example, shear attenuation in the upper mantle is the strongest (low Q_μ) at depths between 150 and 175 km irrespective of the amount of gradient damping employed in this region (Fig. 15d). It is worth noting that the lowest damping weights ($\gamma_g = 10$, 50) lead to very oscillatory models with depth and contain spurious features such as a Q_μ discontinuity at 410 km that is not substantiated by a L-curve

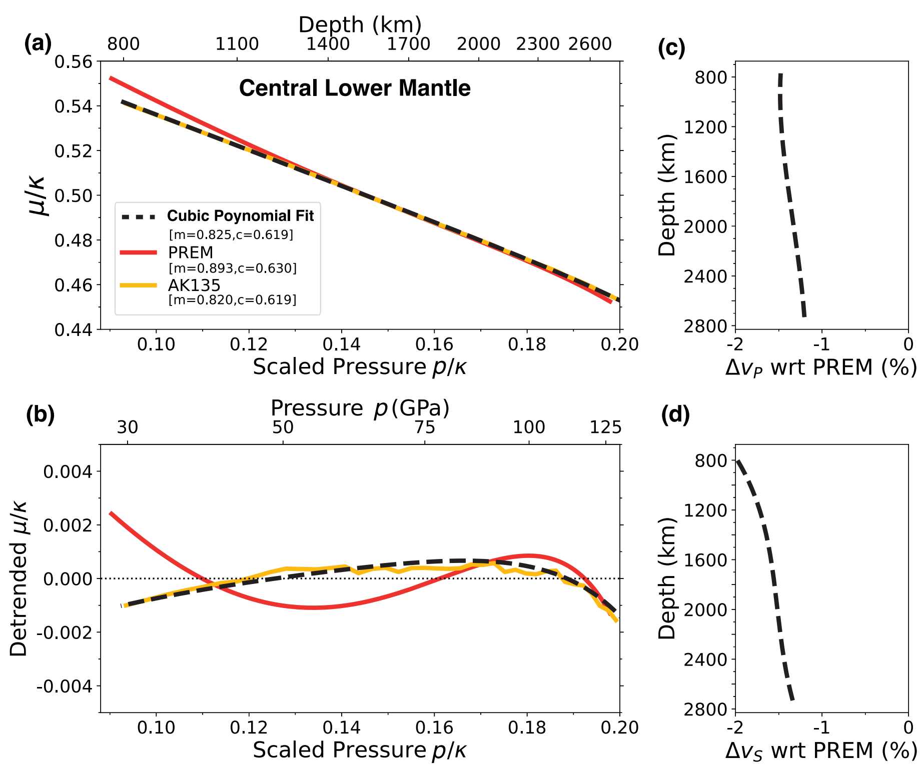

Fig. 12. Impact of parameterization on the derivative properties sensitive to spin transitions in the lower mantle. (a) Shear modulus (μ) and pressure (p) are both scaled by the bulk modulus (κ) calculated from PREM and the body-wave model AK135. (b) Trends between the two parameters are removed with a polynomial of the form $\mu/\kappa = c$ - $m{\cdot}p/\kappa$; the polynomial terms for each radial model are provided in the legend. Polynomial coefficients of v_S and v_P variations in the central lower mantle of PREM are adjusted to give trends in the modulus ratio (μ/κ) similar to AK135 using the downhill simplex method (e.g. Nelder and Mead, 1965). (c,d) Minor changes are needed to the PREM velocity structure (reduction of ~1.5–2 % in v_S, ~1.2 % in v_P) in order to fit AK135 profiles of derivative properties (dashed black curves in a,b). A slight change in the gradient of μ/κ in the central lower mantle of AK135 has been interpreted as a signature of spin transitions in iron-bearing minerals by Kennett (2021). We demonstrate that a parsimonious cubic polynomial parameterization in velocity structure is adequate to capture this feature of AK135 and parameterization in terms of several linear gradients is not required. Feasibility for the detection of spin transitions based on reference datasets is discussed further in Section 4.4 of Paper II.

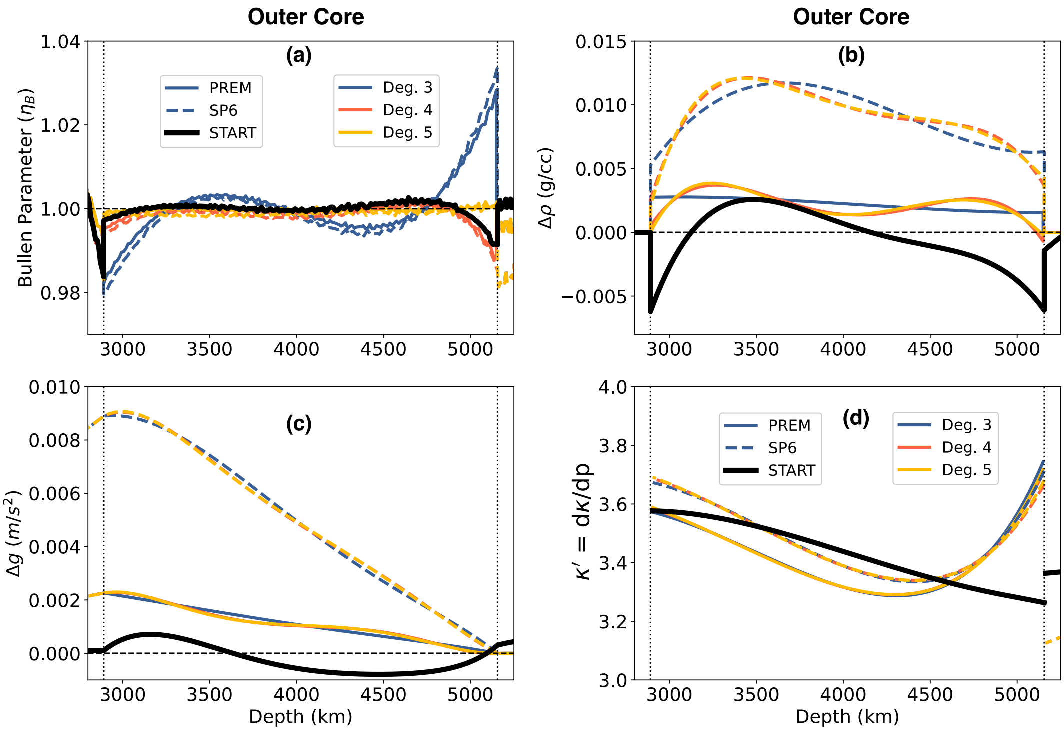

Fig. 13. Impact of parameterization and regularization on the derivative properties of the outer core. If density and its gradients follow the Adams-Williamson equation ($d\rho/dr = -\rho^2 g/\kappa$) with a prescribed value at the top of the outer core ($\rho^{top}_{OCO} = 9.90349$ g/cm^3 in PREM), such variations can only be captured with high-order polynomials (Section 4.1). (a) Estimates of the Bullen's stratification parameter η_B after the density variations derived from the SP6 and PREM elastic structure have been re-parameterized in terms of polynomials up to orders 3, 4 and 5. Polynomials of order 4 or higher are needed to avoid artifacts ($|\eta_B - 1| > 0.005$) that lead to spurious interpretations of inhomogeneity or non-adiabicity in the outer core. (b-c) Differences in the density and gravity (g) variations between the re-parameterized model and PREM; large deviations are removed in our starting model (START) by reducing ρ^{top}_{OCO} to 9.89526 g/cm^3 (Section 4.2). (d) Derivative property of the gradient in adiabatic bulk modulus with pressure ($\kappa' = d\kappa/dp$) is reported for PREM, SP6 and START. Reparametrizing the density structure in terms of polynomials of various orders does not change the κ' trends. A positive curvature ($\kappa'' = d^2\kappa/d^2p$) in earlier models is incompatible with expectations of a well-mixed outer core of uniform composition. START removes this anomalous feature by damping the third derivative (R_t) of ρ and v_P variations in the outer core (Appendix A, Table A.1).

analysis (e.g. Hansen, 2006, Fig. 15c). Robust models with less-oscillatory behavior afford improved fits to quality factor data and do not require a large step change ($\Delta Q_\mu \geq 30$) at the 410-km discontinuity.

We follow an iterative inversion scheme where the sensitivity matrices **G** are re-calculated for several iterations until convergence is achieved for all datasets. Recalculation of the sensitivity kernels accounts for the strongly non-linear and substantial effects of even slight deviations ($\lesssim$0.5 %) of physical parameters on the eigenfunctions and eigenfrequencies of normal modes. This approach is in contrast to several studies where fixed sensitivity kernels from the starting model were used to guide the search for an optimal solution (e.g. Durek and Ekström, 1996; Dalton et al., 2008). We demonstrate the utility of this iterative approach in derivations of radial attenuation structure using two experiments. First, we use a computationally expensive non-linear optimization algorithm (e.g. Nelder and Mead, 1965) to show that a second iteration in relatively simple inversions of radial shear attenuation (Q_μ) improve the χ^2 fits (Fig. 15a,b) by ~30 %; more iterations (at least 3–5) are usually needed to reach convergence in full (an)elastic and density inversions. Improvements in data fits from iterations are due to the changes in Q_μ of ~5–10 %, which are comparable to the signal in lateral variations of attenuation (e.g. Selby and Woodhouse, 2002; Dalton et al., 2008). Large deviations in shear attenuation can substantially alter the mode eigenfrequencies and displacement eigenfunctions, especially for vibrations at longer periods ($T \gg 1$ s) that sense a more pronounced and mechanically weak low-velocity zone in the uppermost mantle due to physical dispersion (cf. Fig. 11 in Paper II). Second, we test for convergence with synthetic data calculated from PREM+QL6 (elastic PREM with anelastic QL6 structure) that also justifies the need for iterative inversions. PREM+QL6 was perturbed in various regions ($\Delta Q_\mu = 10$–50) for use as the starting model in inversions for Q_μ structure. Even in the absence of noise, the perturbed models only converge back ($|\Delta Q_\mu| < 5$) to PREM+QL6 when starting perturbations were less than $\Delta Q_\mu = 20$. This is indicative of the strong non-linear dependence on the starting model, especially in the mantle lithosphere (24.4–80 km) and inner core where available quality-factor data afford weaker constraints.

4.4. Analytical versus numerical approaches

Classical radial models (e.g. Dziewoński and Anderson, 1981; Durek and Ekström, 1996) have typically been constructed with non-linear optimization algorithms like the downhill simplex method (e.g. Nelder and Mead, 1965) and sensitivity kernels computed numerically by perturbing the physical parameters in a starting model. Every physical parameter (e.g. density ρ) is perturbed in turn by an ad-hoc amount of each basis function ($< \cdot >$ in Fig. 5); data predictions from the starting and perturbed models are then subtracted to get the sensitivity matrix (i.e. **G**) employed in standard optimization routines (e.g. Press et al., 1992). Numerical approaches are easier to implement as theoretical complexities like attenuation and physical dispersion are automatically accounted for in the forward calculations. For example, normal modes in a 1D Earth model account for physical dispersion by solving the radial scalar equations for the eigenfrequency and displacement eigenfunctions using dispersed elastic parameters relevant to every normal mode (Woodhouse, 1988; Masters et al., 2011). However, numerical approaches become computationally infeasible when a large set of

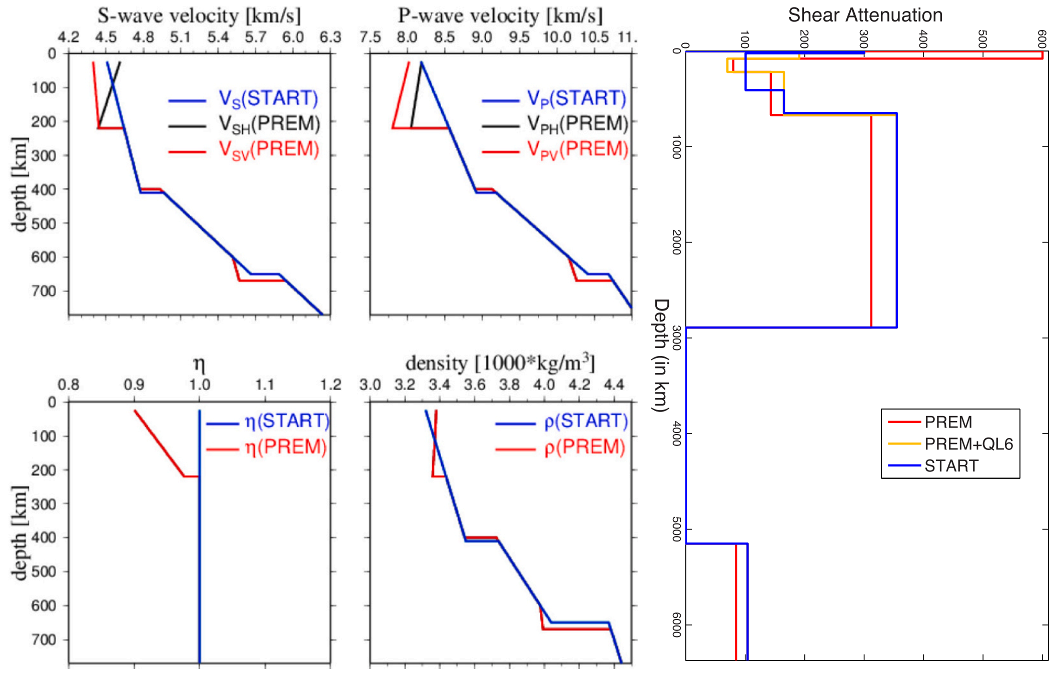

Fig. 14. Starting model (START) used in the inversions. The model perturbations consist of combinations of 7 evenly-spaced cubic B-splines between 24.4 and 410 km and polynomials up to order 4 elsewhere (Fig. 5, Appendix A). A layered parameterization with boxcar functions is used for bulk attenuation (Q_κ) in various regions of the mantle and core. PREM+QL6 denotes that the elastic and density variations are from PREM while attenuation is from QL6. Core structure in START is modified from PREM based on SP6 and other constraints (Section 4.2).

moderate- to high-frequency normal modes (T < 150 s) are analyzed or when the Earth model is expressed in terms of a large set of basis functions. Since non-linear optimization techniques require an iterative scheme to reach convergence, especially in the absence of a good starting model, repeated calculations of **G** matrices quickly becomes the rate-limiting step in such inversion schemes.

We develop an analytical approach of calculating the sensitivity matrices based on first-order perturbation theory (Section 2), which utilizes the local-eigenfrequency approximation to model the normal-mode eigenfrequencies and quality factors in terms of degree-0 perturbations to a starting model (e.g. eqs. 15 and 16). The analytical sensitivity kernels are benchmarked against classical numerical schemes that repeatedly perturb a single parameter in a region using two approaches. First, normal modes in the perturbed radial models for each parameter (Fig. 5) were compared against those predicted by analytical kernels accounting for physical dispersion. Differences in eigenfrequencies and quality factors between the original and perturbed models arising from structural perturbations should ideally be captured by eqs. 5 and 6 within the limits of first-order perturbation theory. Our experiments suggest that both formulations predict estimates that are similar to within 0.1–1 ppm, substantially lower than the relative uncertainties in available data (Section 2.6). It is worth noting that these linearity limits are only valid for small perturbations (~1–5 times the $<\cdot>$ values in Fig. 5) and are voided more easily for certain basis functions (e.g. v_S splines in the upper mantle). These basis functions correspond to regions with the strongest displacements in the eigenfunctions of surface-wave equivalent normal modes and their associated structural sensitivities. Numerical kernels used widely in seismological studies are strictly valid within these limits of linear perturbation theory and our analytical kernels can reach the same level of precision. Second, inversions for shear attenuation were carried out using analytical kernels and benchmarked against inversions using numerical kernels for a fixed parameterization (Fig. 16). General trends in shear attenuation are consistent between the two formulations with peak attenuation ($Q_\mu \sim 80$) at depths below 150 km. Both tests confirm that the use of an analytical formulation is robust for small perturbations from starting models and recalculating sensitivity kernels in an iterative scheme gives similar inferences on bulk Earth structure.

Accounting for physical dispersion (e.g. eq. 16) is critical when dealing with the non-linearities in modeling both eigenfrequencies and quality factors of normal modes. Inverting solely for mantle shear attenuation (Q_μ) leads to models that fit the quality factor dataset significantly better than other radial models while fits to eigenfrequencies deteriorate. This procedure of fixing the elastic and density structure in Q_μ inversions is analogous to what was adopted by Durek and Ekström (1996) during the construction of attenuation model QL6; similar tradeoffs are also seen therein where fits to quality factor data improve at the expense of eigenfrequencies (Fig. 16). Fits to eigenfrequencies deteriorate by a factor of ~1.5–3 for various subsets of modes, which is significant at the 95 % confidence level for the number of parameters in these inversions. Our experiments with eigenfrequencies reveal that not accounting for the dispersion term (e.g. eq. 16) leads to slower convergence towards a joint solution of radial (an) elastic structure. Tradeoffs across elastic, density and anelastic variations are therefore harder to disentangle without joint inversions and an explicit dispersion correction.

5. Conclusions and outlook

Main results of this study are reference bulk Earth datasets and new modeling concepts that can be used to infer unbiased average properties of the heterogeneous interior. The reference dataset comprises normal-mode eigenfrequencies and quality factors, surface-wave dispersion curves, impedance constraints and travel-time curves from body waves, and astronomic-geodetic observations. This reference dataset represents better geographic coverage, wider variety of techniques and broader frequency range (~0.3 mHz – 1 Hz, ~1–3200 s) than those used in the construction of earlier radial reference models. Our best estimates lie within the 95 % confidence interval of most individual studies and relative uncertainties are reduced by more than half from PREM, demonstrating the improved consistency across measurement techniques. Geographic bias towards structure sampled by continental stations is evident in earlier studies that systematically underpredict the phase velocities of Rayleigh waves (e.g. PREM) and arrival times of diffracted S_{diff} waves (e.g. AK135). In order to accurately describe the spherical average of Earth's 3D heterogeneity (degree-0 term in spherical harmonics), we account for geographic bias in body-wave and surface-wave arrival times and reconcile normal-mode observations. The new reference dataset is indicative of a peak anisotropy in the upper mantle, reduced velocities in the lowermost mantle, and strong gradients in the outermost outer core. Reference datasets can be used for the calibration and interpretation of Earth's bulk constituents as estimated by mineralogical models and dynamical simulations.

Due to the theoretical limitations arising from lateral heterogeneity, reference bulk Earth datasets cannot be interpreted directly in terms of radial structure. Most theoretical formalisms of traveling (surface and body) waves utilize the local-eigenfrequency approximation, which is valid only when horizontal wavelengths of structural heterogeneity (s) are much greater ($s \ll l$) than that of the equivalent normal modes (${}_nS_l$, ${}_nT_l$). A local threshold parameter $\varkappa_{thres}$ is introduced to assess the unaccounted for volumetric effects of heterogeneity in this approximation. Recent estimates of crustal (CRUST2.0) and mantle heterogeneity (S362ANI+M) limit the validity of the local-eigenfrequency approximation to short periods for both Love waves (toroidal fundamental, T < 120 s) and Rayleigh waves (spheroidal fundamental, T < 220 s). The adoption of JWKB theory and ray approximation to attribute the propagation phase to interior structure may not be justified for long-period surface-waves. This limitation stems from a more fundamental aspect of wave propagation in complex heterogeneous media than other complications such as finite-frequency (e.g. Wang and Dahlen, 1994) or off-great-circle propagation effects (e.g. Woodhouse and Wong, 1986), which actually utilize rather than circumvent the local-eigenfrequency approximation.

Our assessment regarding the validity of local-eigenfrequency approximation for constructing radial reference models is based on a single set of three-dimensional models. Both CRUST2.0 and S362ANI+M constrain long-wavelength heterogeneity (nominal resolution ≥ 200–1500 km, degree∼18 in the mantle) and impose v_P-v_S and ρ-v_S scaling *a priori* in their construction. Recent studies have reported heterogeneity with increasingly finer resolution (e.g. Ritsema et al., 2011; Laske et al., 2013; French and Romanowicz, 2014) and scaling complexity (e.g. Moulik and Ekström, 2016), which can modify somewhat our inferences on the local-eigenfrequency approximation. Stronger power than S362ANI+M, especially at the shorter wavelengths in recent studies (e.g. Lebedev and van der Hilst, 2008; French and Romanowicz, 2014), could shift the local threshold ($\varkappa_{thres}$) to higher frequencies and angular orders, severely limiting the applicability of theoretical formulations employed in such inversions (e.g. Nolet, 1990; Li and Tanimoto, 1993). Our estimates of local thresholds only account for the effects of even-degree variations on isolated normal modes; stronger power at odd degrees and shorter wavelengths could also shift the limitation to higher frequencies. Validity limits could also depend on the structural (in)homogeneities that traveling waves encounter along the ray path (e.g. ocean-continent transition) due to the strong coupling between normal modes (e.g. Park, 1986). Applicability of the local-eigenfrequency approximation needs to assessed rigorously during the forward and inverse modeling of traveling waves. Caution is warranted before interpreting the strong amplitudes of finer-scale 3D variations in recent tomographic studies.

A strongly heterogeneous crust can influence the features and interpretations of radial reference Earth models. Even within the validity limits of the local-eigenfrequency approximation, several reference bulk Earth datasets cannot be modeled linearly in terms of radial structure. Lateral variations in the crust can change the shape of mode eigenfunctions and local eigenfrequencies in a significantly non-linear fashion. In case of the quality factors of normal modes, non-linear contributions from a crust with uniform shear attenuation (Q_μ = 300)

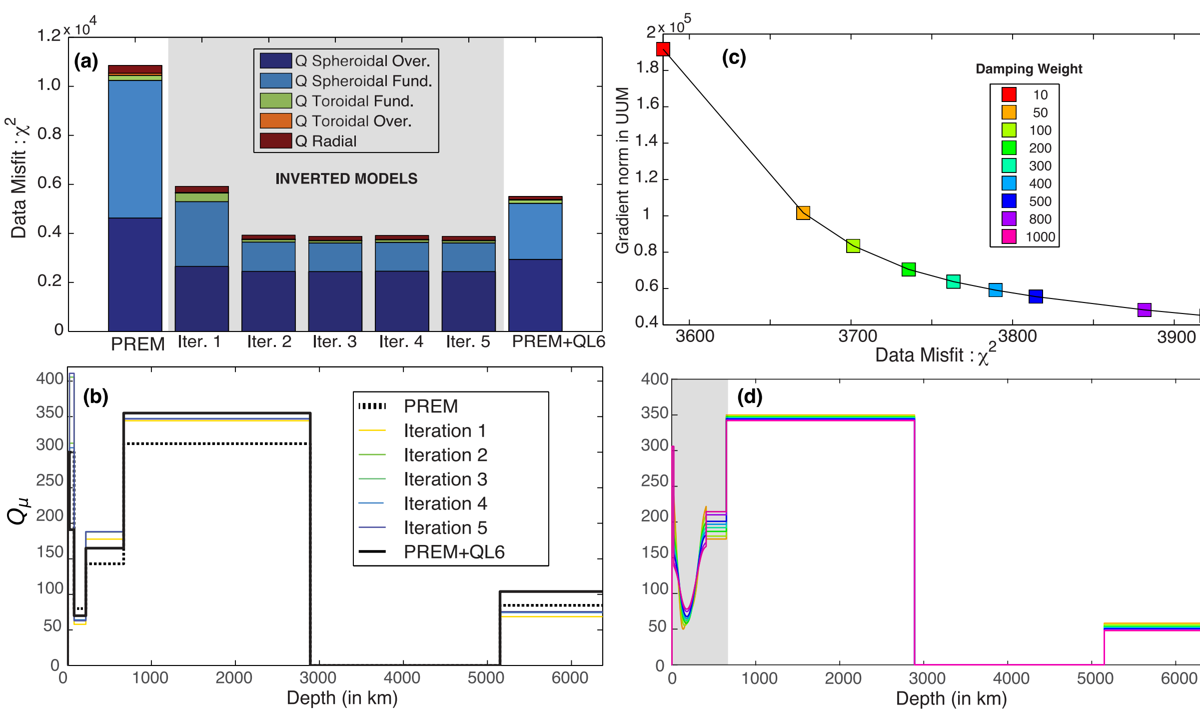

Fig. 15. Influence of iterations (a-b) and damping (c-d) on the inversions for radial structure. Quality factors of some radial, spheroidal and toroidal modes are employed in the iterative inversions for shear attenuation (Q_μ). The iterations involve recalculating the sensitivity kernels to account for the strongly non-linear effects of even slight deviations in radial structure on the eigenfunctions and eigenfrequencies of normal modes. Various amounts of gradient damping in the upper mantle (c) result in similar models with a peak in shear attenuation (low Q_μ) between 150 and 180 km depth (d). Note that the lowest damping weights (γ_g = 10,50) lead to very oscillatory models with features such as a discontinuity at 410 km that is not substantiated by the L-curve analysis (e.g. Hansen, 2006). These inversions either employ START1D (Fig. 14) or PREM with a modified mantle lithosphere (24.4–80 km, Q_μ= 300) as the starting model.

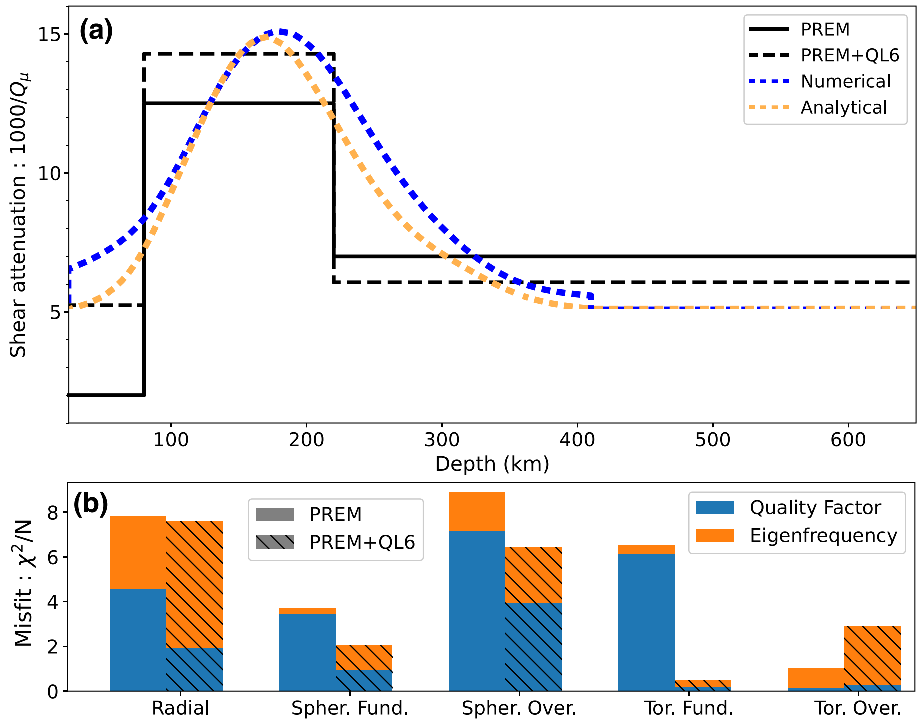

Fig. 16. Tests for benchmarking kernel formulations. (a) Inversions using either numerical or analytical kernels for radial Q_μ structure. Slightly different data, starting models and damping are used in either inversions; numerical inversion does not include a damping disfavoring abruptness across the 410-km discontinuity. Both models show a peak attenuation between 150 and 180 km depth. (b) Fits to reference dataset of normal-mode eigenfrequencies and quality factors from PREM and QL6 attenuations models. Compared to PREM, fits to quality factors improve with the QL6 attenuation model while fits to eigenfrequencies deteriorate, demonstrating the need for joint (an)elastic inversions that account for physical dispersion (eq. 16).

are statistically insignificant due to the large scatter in available measurements. Crustal contributions to observed phase-velocity variations are statistically significant and comparable in magnitude (> 50 %) to the observations of both short-period Love (≤40 s) and intermediate-period Rayleigh waves (50–100 s). Therefore, non-linear contributions from the crust can have a perceptible and often dramatic effects on the inferences of radial elastic and density structure. While linear assumptions might imply that high velocities for short-period Love waves are indicative of a thin crust (Ekström, 2011), non-linear crustal contributions can explain most of the signal suggesting that no major changes to the Moho depth are required. Lateral variations cannot be averaged out linearly when interpreting the global Love-Rayleigh discrepancy of phase velocities in terms of radial structure, as was assumed in previous theoretical (e.g. Anderson and Dziewoński, 1982) and modeling studies (e.g. PREM).

We extend full spectrum tomography (FST) to account for the intertwined theoretical (e.g. non-linearities) and observational (e.g. geographic bias) effects of lateral heterogeneity on the inferences of bulk Earth structure. Due to the strong non-linearities inherent in joint inversions for density and (an)elastic structure, we formulate analytical sensitivity kernels that account explicitly for anelastic dispersion and are re-computed at every iteration. Our new inversion scheme for radial models is benchmarked against classical approaches that employ computationally intensive numerical kernels and non-linear optimization schemes. Rapid convergence towards an optimal solution is facilitated with analytical basis functions and a revised starting model. Our parsimonious parameterization, comprising polynomials up to order 4 and cubic B-splines, is dictated by the improved data coverage and avoids interpretative assumptions on EoS formulations and mineralogical parameters. If the order of polynomial for density is greater than that of the elastic structure, artifacts in the Bullen's stratification parameter (η_B) that wrongly imply inhomogeneity and non-adiabaticity can be prevented in potentially well-mixed regions like the outer core. Other derivative properties like the gradient of bulk modulus with pressure (κ') in the core are adjusted to match expectations from mineral physics without deteriorating the fits to reference datasets. A cubic polynomial parameterization in the lower mantle is consistent with mineralogical expectations and is able to capture possible changes in the gradient of modulus ratio (μ/κ) associated with spin transitions in iron-bearing minerals. Modeling concepts introduced here provide a way to infer the average properties of a heterogeneous Earth, crucial for the geological interpretations based on the radial (1D) reference model (REM1D, Paper II) and the related construction of the 3D reference Earth model (REM3D).

CRediT authorship contribution statement

Pritwiraj Moulik: Conceptualization, Methodology, Data curation, Software, Formal analysis, Visualization, Writing – original draft preparation, Writing – review & editing. **Göran Ekström:** Writing – review & editing, Supervision.

Declaration of competing interest

The authors declare that they have no known competing financial interests or personal relationships that could have appeared to influence the work reported in this paper.

Acknowledgments

We dedicate this study to the memory of Adam Dziewonski for his guidance and specific suggestions on the refinements to our parameterization scheme. We thank Guy Masters, Frederik Simons, Gabi Laske and Vedran Lekic for discussions, and the broader geoscience community for contributing to this project (Moulik and The 3D Reference Earth Model (REM3D) Consortium, 2022, http://rem3d.org).

Funding Statement

This work has been supported for several years first by fellowships at Columbia University and thereafter by partial support from the National Science Foundation (NSF) Grants (EAR-1315984, EAR-1345082, EAR-2341811) and Princeton University. Some of the calculations were performed using the open-source AVNI toolkit (Moulik et al., 2023, http://avni.globalseismology.org) developed with support from the Computational Infrastructure for Geodynamics (http://geodynamics.org), which is funded by the NSF Grants EAR-0949446 and EAR-1550901.

Appendix A. Regularization schemes

Our modular parameterization allows evaluation of isolated features in the Earth using various types of damping or regularization as *a priori* information. All damping schemes (Section 4.3) can be expressed as a general matrix formulation $\mathbf{D}(\mathbf{m}+\delta^{abs}\mathbf{m}_0) = c$, where $\mathbf{m}_0$ is the starting model, c is a constant, and δ^{abs} dictates whether absolute properties (i.e. $\mathbf{m}_0+\mathbf{m}$, δ^{abs}=1) rather than the perturbations (i.e. $\mathbf{m}$, δ^{abs}=0) are regularized. Following discrete inverse theory (e.g. Menke, 1989), solution to our regularized inverse problem is

$$\mathbf{m}_{LS} = \left[\sum_i w_i\left(\mathbf{G}^T\mathbf{G}\right)_i + \sum_j \gamma_j\left(\mathbf{D}^T\mathbf{D}\right)_j\right]^{-1}\left[\sum_i w_i\left(\mathbf{G}^T\mathbf{d}\right)_i - \sum_j \gamma_j\left(\delta^{abs}\cdot\mathbf{D}^T\mathbf{D}\mathbf{m}_0 - \mathbf{D}^T c\right)_j\right], \tag{A.1}$$

where $\mathbf{m}_{LS}$ is a matrix containing the best-fitting model while w_i are weights given to various types of reference datasets. Here, γ_j are the weights given to different regularization choices (eq. 23) and $\left(\mathbf{D}^T\mathbf{D}\right)_j$ are the respective damping matrices derived numerically based on the formulations below. Table A.1 lists the damping choices employed during the construction of the new radial reference Earth model REM1D (Paper II).

Perturbations to our starting model ($\oplus^0$, eq. 22) are expressed in terms of two types of piecewise-continuous, analytical functions in different principal regions (Fig. 5). The first type comprises polynomials up to the fourth order ($n = 4$) i.e. values at the top ($B_t(r) = (r-r_b)/(r_t-r_b)$) and bottom ($B_b = (r_t-r)/(r_t-r_b)$) of a region, as well as the quadratic (B_{x^2}), cubic (B_{x^3}) and quartic polynomials terms (B_{x^4}). These basis functions can be expressed as

$$B_{x^n}(r) = \begin{cases} \left(r^n - r_t^n\right) - (r-r_t)^*\sum_{k=0}^{n-1}\left(r_b^{n-1-k} * r_t^k\right) & \text{if } r_b \le r \le r_t \\ 0 & \text{otherwise,} \end{cases} \tag{A.2}$$

where r_t and r_b correspond to the top and bottom radius of a region, respectively. Our parameterization in the uppermost mantle also includes piecewise-continuous cubic B-splines (Lancaster and Salkauskas, 1986) that result in smooth variations across the 220-km discontinuity. We adopt the 7 interior cubic B-splines (s_i, i=1–7) from a set defined across 9 ($N+1$) knots spaced evenly ($h = r_{i+1}$-r_i = 48.2 km) between the depths of 24.4 km (r_N = 6346.6 km) and 410 km (r_0 = 5961 km).

$$B_{s_1}(r) = \frac{2}{3}\times\begin{cases} -\frac{1}{2}h^{-3}(r-r_0)^3 + \frac{3}{2}h^{-1}(r-r_0) & \text{if } r_0 \le r \le r_1 \\ \frac{3}{4}h^{-3}(r-r_1)^3 - \frac{6}{4}h^{-2}(r-r_1)^2 + 1 & \text{if } r_1 \le r \le r_2 \\ -\frac{1}{4}h^{-3}(r-r_2)^3 + \frac{3}{4}h^{-2}(r-r_2)^2 - \frac{3}{4}h^{-1}(r-r_2) + \frac{1}{4} & \text{if } r_2 \le r \le r_3 \\ 0 & \text{if } r_3 \le r \le r_N, \end{cases} \tag{A.3}$$

$$B_{s_i}(r) = \frac{2}{3}\times\begin{cases} 0 & \text{if } r_0 \le r \le r_{i-2} \\ \frac{1}{4}h^{-3}(r-r_{i-2})^3 & \text{if } r_{i-2} \le r \le r_{i-1} \\ -\frac{3}{4}h^{-3}(r-r_{i-1})^3 + \frac{3}{4}h^{-2}(r-r_{i-1})^2 + \frac{3}{4}h^{-1}(r-r_{i-1}) + \frac{1}{4} & \text{if } r_{i-1} \le r \le r_i \\ \frac{3}{4}h^{-3}(r-r_i)^3 - \frac{6}{4}h^{-2}(r-r_i)^2 + 1 & \text{if } r_i \le r \le r_{i+1} \\ -\frac{1}{4}h^{-3}(r-r_{i+1})^3 + \frac{3}{4}h^{-2}(r-r_{i+1})^2 - \frac{3}{4}h^{-1}(r-r_{i+1}) + \frac{1}{4} & \text{if } r_{i+1} \le r \le r_{i+2} \\ 0 & \text{if } r_{i+2} \le r \le r_N, \end{cases} \tag{A.4}$$

$$B_{s_{N-1}}(r) = \frac{2}{3}\times\begin{cases} 0 & \text{if } r_0 \le r \le r_{N-3} \\ \frac{1}{4}h^{-3}(r-r_{N-3})^3 & \text{if } r_{N-3} \le r \le r_{N-2} \\ -\frac{3}{4}h^{-3}(r-r_{N-2})^3 + \frac{3}{4}h^{-2}(r-r_{N-2})^2 + \frac{3}{4}h^{-1}(r-r_{N-2}) + \frac{1}{4} & \text{if } r_{N-2} \le r \le r_{N-1} \\ \frac{1}{2}h^{-3}(r-r_{N-1})^3 - \frac{3}{2}h^{-2}(r-r_{N-1})^2 + 1 & \text{if } r_{N-1} \le r \le r_N \end{cases} \tag{A.5}$$

While curvature at the boundary knots ($i = 0,N$) are adjusted to be zero in this basis set to ensure uniqueness (e.g. Michelini and McEvilly, 1991), we exclude the two boundary cubic B-splines (s_0, s_N) from our parameterization since the edge variations are captured by the other polynomial functions B_b and B_t (Fig. 5). Radial derivatives such as gradients ($B' = \partial B/\partial r$), curvature ($B''$), and third derivatives (B''') can be readily calculated and employed in various regularization schemes (eq. 23) outlined below. All radius and derivative terms discussed in this section (e.g. eqs. A.2–A.5) are normalized by the mean radius of the solid Earth (i.e. $r = 1$ at $R = 6371$ km).

(i) **Step changes at discontinuities (R_d):** In order to impose x% contrast in a physical property (m_k) between two adjoining principal regions (p_1, p_2), the general expression is

$$
\begin{aligned}
&R_d(m_k, p_1, p_2) = \left[(\mathbf{S} - x/100{*}\mathbf{A})^T m\right]^{1/2} = 0 \\
&m = \left[c^{m_k}_{p_1,b}, c^{m_k}_{p_2,t}\right] \qquad \mathbf{S} = [-1, 1] \qquad \mathbf{A} = [1/2, 1/2] \\
&\mathbf{D} = \mathbf{S} - x/100{*}\mathbf{A} \qquad \delta^{abs} = 1 \qquad c = 0
\end{aligned}
\tag{A.6}
$$

where m contains values at the top of an underlying region ($c_{p_2,t}$) and at the bottom of an overlying region ($c_{p_1,b}$) in the starting model, respectively. This type of damping incorporates information from reference datasets (Table 3) and is strongly imposed where there is limited or no evidence of a pervasive first-order discontinuity with a step change in properties (e.g. $x = 0$ % at 771 km depth).

(ii) **Gradients of the perturbations or inverted model (R_g):** The smoothness of radial variations within a region can be quantified based on its gradients ($\mathbf{m}'$). We impose smooth perturbations for all physical parameters following

$$
\begin{aligned}
&R_g(m_k, r_{bot}, r_{top}) = \left[\sum_h \delta c^{m_k}_h \int_{r_{bot}}^{r_{top}} W^2 (B'_h \cdot B'_h)(r)\ dr\right]^{1/2} = 0 \\
&\mathbf{D} = \left[W(r)B'_1(r), \ldots.., W(r)B'_h(r)\right] \qquad \delta^{abs} = 0 \qquad c = 0
\end{aligned}
\tag{A.7}
$$

where the integral is performed over the range of radii within the region, **D** contains rows for evenly-spaced concentric shells centered at radius r, W is a depth-dependent weighting function, and $\delta c^{m_k}_h$ is the perturbation to basis coefficient (eq. 22). The weighting function is only relevant for variations in the upper mantle and are adjusted separately for three depth ranges - 24.4–80, 80–250, 250–330 and 330–410 km. Our choice of a depth-dependent damping scheme is informed by the non-uniform sensitivity of reference datasets to the strongly varying structure in the upper mantle. Quality factors of Rayleigh waves, for example, are less sensitive to the Q_μ variations between 330 and 410 km; we apply up to 10 times stronger damping than the uppermost mantle to disfavor strong Q_μ gradients at these depths. Gradients of physical parameters at the Earth's center ($r = 0$) are expected to converge towards zero. This constraint on the absolute properties of the inverted model can be expressed in its matrix form as

$$
\mathbf{D} = \left[B'_1(0), \ldots.., B'_h(0)\right] \qquad \delta^{abs} = 1 \qquad c = 0.
\tag{A.8}
$$

(iii) **Higher-order derivatives of the inverted model (R_c, R_t):** Curvature of the model ($\mathbf{m}''$) can often dictate the smoothness in thin regions with strong linear gradients. For example, quadratic and cubic terms of v_P and v_S structure in the upper lower mantle (ULM; 650–771 km depth) and D″ (2741–2891 km depth) regions need to suppressed due to weaker data constraints. Moreover, third derivatives of the inverted model ($\mathbf{m}'''$) can influence interpretations in mineral physics and global geodynamics, especially in regions where homogeneity and adiabicity may be expected such as the fluid outer core (Section 4.1.4, Fig. 13). The general expression for damping the curvature of k-th model parameter in a region is

$$
\begin{aligned}
&R_c(m_k, r_{bot}, r_{top}) = \left[\sum_h \delta c^{m_k}_h \int_{r_{bot}}^{r_{top}} W^2 (B''_h \cdot B''_h)(r)\ dr\right]^{1/2} = 0 \\
&\mathbf{D} = \left[W(r)\cdot B''_1(r), \ldots.., W(r)\cdot B''_h(r)\right] \qquad \delta^{abs} = 1 \qquad c = 0
\end{aligned}
\tag{A.9}
$$

Similar expressions for the third derivatives of a parameter (R_t) along with depth varying weights can be readily employed in our inversions.

(iv) **Norm of the perturbations or inverted model (R_n):** Strong model complexity in certain features of the Earth cannot be justified based on the fits to reference datasets. We apply norm damping on model perturbations in these situations as our starting model represents *a priori* information on physically plausible structure (Section 4.2). This constraint is applied in the inner core, for example, where limited sensitivity of the datasets in this study disfavor substantial deviations from the shear attenuation in our starting model. This regularization term can be expressed as

$$
\begin{aligned}
&R_n(m_k, r_{bot}, r_{top}) = \left[\sum_h \delta c^{m_k}_h \int_{r_{bot}}^{r_{top}} W^2 (B_h \cdot B_h)(r)\ dr\right]^{1/2} = 0 \\
&\mathbf{D} = \left[W(r)B_1(r), \ldots.., W(r)B_h(r)\right] \qquad \delta^{abs} = 0 \qquad c = 0
\end{aligned}
\tag{A.10}
$$

where the integral is defined from the top of the inner core to the center of the Earth. In other situations, norm of absolute properties ($\delta^{abs} = 1$) may need to be suppressed instead based on data fit and mineralogical considerations. For example, both a_S and a_P anisotropy in the depth range of 250–410 km are suppressed without deteriorating the fits to surface-wave dispersion data (Table A.1).

(v) **Scaling between physical parameters (R_s):** The correlation and scaling relationships between two physical parameters (m_a, m_b) may be expected based on petrological and other geophysical constraints. This regularization term can be expressed as

$$
\begin{aligned}
& R_s(m_a, m_b, r_{bot}, r_{top}) = \left[\sum_h \left[\left(c_h^{m_a} + \delta c_h^{m_a} \right) - \nu \cdot \left(c_h^{m_b} + \delta c_h^{m_b} \right) \right] \int_{r_{bot}}^{r_{top}} W^2 (B_h \cdot B_h)(r) \ dr \right]^{1/2} = 0 \\
& D^a = \left[W(r) B_1^a(r), \ldots.., W(r) B_h^a(r) \right] \\
& D^b = \left[-\nu W(r) B_1^b(r), \ldots.., -\nu W(r) B_h^b(r) \right] \\
& \mathbf{D} = \left[D^a, D^b \right] \qquad \delta^{abs} = 1 \qquad c = 0
\end{aligned}
\tag{A.11}
$$

where the ν is a scaling factor between the absolute values of the two parameters. In Paper II, this damping term is used for evaluating anisotropic variations in the mantle lithosphere (24.4–80 km depth) but is ultimately excluded during REM1D construction.

Table A.1
Regularization adopted during REM1D construction in Paper II. The terms below modulate the norm (γ_n), curvature (γ_c) and third order derivatives (γ_t) following eqs. 23 and Appendix A. When a superscript "*" is noted, absolute properties of the updated model is being regularized ($\delta^{abs} = 1$) in lieu of perturbations to the starting model ($\delta^{abs} = 0$). Additional terms not listed below modulate the step changes (in %) across discontinuities (γ_d) and gradients of model perturbations (γ_g) for all physical parameters.

Region	Depth (km)	ρ	v_P	v_S	a_P	a_S	η
Upper mantle	24.4–80	–	γ_n	–	–	–	–
[UUM]	80–250	–	–	–	–	–	–
	250–330	γ_n	γ_n	–	γ_n^*	γ_n^*	γ_n
	330–410	γ_n	γ_n	–	γ_n^*	γ_n^*	γ_n
Outer core [OCO]	2891–5156	γ_t^*	γ_t^*	–	–	–	–
Inner core [ICO]	5156–6371	γ_c^*	γ_c^*	–	–	–	–
Center [CoE]	6371	γ_g^*	γ_g^*	γ_g^*	–	–	–

Appendix B. Supplementary data

Supplementary data to this article can be found online at https://doi.org/10.1016/j.pepi.2025.107319.

Data availability

The reference dataset, REM1D model (see Paper II for features and interpretations), and codes to evaluate physical parameters at arbitrary locations are available from the project webpage (http://rem3d.org) and are permanently archived on Zenodo (https://doi.org/10.5281/zenodo.8407693).

References

Abers, G.A., Fischer, K.M., Hirth, G., Wiens, D.A., Plank, T., Holtzman, B.K., McCarthy, C., Gazel, E., 2014. Reconciling mantle attenuation-temperature relationships from seismology, petrology, and laboratory measurements. Geochem. Geophys. Geosyst. 15 (9), 3521–3542. https://doi.org/10.1002/2014gc005444.

Akaogi, M., Ito, E., Navrotsky, A., 1989. Olivine-modified spinel-spinel transitions in the system Mg2SiO4-Fe2SiO4: calorimetric measurements, thermochemical calculation, and geophysical application. J. Geophys. Res. Solid Earth 94 (B11), 15671–15685. https://doi.org/10.1029/jb094ib11p15671.

Akaogi, M., Tanaka, A., Ito, E., 2002. Garnet–ilmenite–perovskite transitions in the system Mg4Si4O12–Mg3Al2Si3O12 at high pressures and high temperatures: phase equilibria, calorimetry and implications for mantle structure. Phys. Earth Planet. Inter. 132 (4), 303–324. https://doi.org/10.1016/s0031-9201(02)00075-4.

Anderson, D.L., 1965. Recent evidence concerning the structure and composition of the earth's mantle. Phys. Chem. Earth 6, 1–131. https://doi.org/10.1016/0079-1946(65)90013-3.

Anderson, D.L., Dziewoński, A.M., 1982. Upper mantle anisotropy: evidence from free oscillations. Geophys. J. Int. 69 (2), 383–404.

Anderson, D.L., Hart, R., 1978. Q of the Earth. J. Geophys. Res. 83, 5869–5882.

Backus, G., Gilbert, F., 1968. The resolving power of gross Earth data. Geophys. J. R. Astron. Soc. 16 (2), 169–205. https://doi.org/10.1111/j.1365-246x.1968.tb00216.x.

Backus, G., Gilbert, F., 1970. Uniqueness in the inversion of inaccurate gross Earth data. Philos. Trans. R. Soc. Lond. Ser. A Math. Phys. Sci. 266 (1173), 123–192. https://doi.org/10.1098/rsta.1970.0005.

Badro, J., 2014. Spin transitions in mantle minerals. Annu. Rev. Earth Planet. Sci. 42 (1), 231–248. https://doi.org/10.1146/annurev-earth-042711-105304.

Badro, J., Fiquet, G., Guyot, F., Rueff, J.-P., Struzhkin, V.V., Vankoo, G., Monaco, G., 2003. Iron partitioning in Earth's mantle: toward a deep lower mantle discontinuity. Science 300 (5620), 789–791. https://doi.org/10.1126/science.1081311.

Bai, L., Ritsema, J., 2013. The effect of large-scale shear-velocity heterogeneity on SS precursor amplitudes. Geophys. Res. Lett. 40 (23), 6054–6058. https://doi.org/10.1002/2013gl058669.

Bassin, C., Laske, G., Masters, G., 2000. The current limits of resolution for surface wave tomography in North America. Eos. Trans. AGU 81 (48) (Fall Meet. Suppl.–03).

Birch, F., 1947. Finite elastic strain of cubic crystals. Phys. Rev. 71 (11), 809–824. https://doi.org/10.1103/physrev.71.809.

Birch, F., 1964. Density and composition of mantle and core. J. Geophys. Res. Solid Earth 69 (20), 4377–4388. https://doi.org/10.1029/jz069i020p04377.

Birge, R.T., 1929. Probable values of the general physical constants. Rev. Mod. Phys. 1 (1), 1–73. https://doi.org/10.1103/revmodphys.1.1.

Bloxham, J., Jackson, A., 1991. Fluid flow near the surface of Earth's outer core. Rev. Geophys. 29 (1), 97–120. https://doi.org/10.1029/90rg02470.

Boschi, L., Ekström, G., 2002. New images of the Earth's upper mantle from measurements of surface wave phase velocity anomalies. J. Geophys. Res. Solid Earth 107 (B4), 2059. https://doi.org/10.1029/2000jb000059.

Buland, R., Berger, J., Gilbert, F., 1979. Observations from the IDA network of attenuation and splitting during a recent earthquake. Nature 277 (5695), 358–362. https://doi.org/10.1038/277358a0.

Bullen, K.E., 1949. Compressibility-pressure hypothesis and the Earth's interior. Geophys. Suppl. Mon. Not. R. Astron. Soc. 5 (9), 335–368. https://doi.org/10.1111/j.1365-246x.1949.tb02952.x.

Bullen, K., 1963. An index of degree of chemical inhomogeneity in the Earth. Geophys. J. R. Astron. Soc. 7 (5), 584–592.

Burakovsky, L., Preston, D.L., Wang, Y., 2004. Cold shear modulus and Grüneisen parameter at all densities. Solid State Commun. 132 (3–4), 151–156. https://doi.org/10.1016/j.ssc.2004.07.066.

Cammarano, F., Deuss, A., Goes, S., Giardini, D., 2005. One-dimensional physical reference models for the upper mantle and transition zone: combining seismic and mineral physics constraints. J. Geophys. Res. Solid Earth 110, B01306. https://doi.org/10.1029/2004jb003272.

Cao, A., Romanowicz, B., 2004. Constraints on density and shear velocity contrasts at the inner core boundary. Geophys. J. Int. 157 (3), 1146–1151. https://doi.org/10.1111/j.1365-246x.2004.02330.x.

Caracas, R., Mainprice, D., Thomas, C., 2010. Is the spin transition in Fe2+−bearing perovskite visible in seismology? Geophys. Res. Lett. 37 (13). https://doi.org/10.1029/2010gl043320.

Cazenave, A., 1995. Earth rotation. In: Ahrens, T.J. (Ed.), Geoid, Topography and Distribution of Landforms. American Geophysical Union, Washington D.C., pp. 32–39

Chambat, F., Valette, B., 2001. Mean radius, mass, and inertia for reference Earth models. Phys. Earth Planet. Inter. 124 (3–4), 237–253. https://doi.org/10.1016/s0031-9201(01)00200-x.

Chambat, F., Ricard, Y., Valette, B., 2010. Flattening of the Earth: further from hydrostaticity than previously estimated. Geophys. J. Int. 183 (2), 727–732. https://doi.org/10.1111/j.1365-246x.2010.04771.x.

Chambers, K., Deuss, A., Woodhouse, J.H., 2005. Reflectivity of the 410-km discontinuity from PP and SS precursors. J. Geophys. Res. Solid Earth 110 (B2), 39. https://doi.org/10.1029/2004jb003345.

Charléty, J., Voronin, S., Nolet, G., Loris, I., Simons, F.J., Sigloch, K., Daubechies, I.C., 2013. Global seismic tomography with sparsity constraints: comparison with smoothing and damping regularization. J. Geophys. Res. Solid Earth 118 (9), 4887–4899. https://doi.org/10.1002/jgrb.50326.

Christensen, U.R., Yuen, D.A., 1985. Layered convection induced by phase transitions. J. Geophys. Res. Solid Earth 90 (B12), 10291–10300. https://doi.org/10.1029/jb090ib12p10291.

Constable, S.C., Parker, R.L., Constable, C.G., 1987. Occam's inversion; a practical algorithm for generating smooth models from electromagnetic sounding data. Geophysics 52 (3), 289–300. https://doi.org/10.1190/1.1442303.

Dahlen, F.A., Tromp, J., 1998. Theoretical Global Seismology. Princeton Univ Press, Princeton Univ Press.

Dalton, C.A., Ekström, G., Dziewonski, A.M., 2008. The global attenuation structure of the upper mantle. J. Geophys. Res. 113, B09303. https://doi.org/10.1029/2007jb005429.

Dannberg, J., Eilon, Z., Faul, U., Gassmöller, R., Moulik, P., Myhill, R., 2017. The importance of grain size to mantle dynamics and seismological observations. Geochem. Geophys. Geosyst. 18 (8), 3034–3061. https://doi.org/10.1002/2017gc006944.

de Wit, R.W.L., Käufl, P.J., Valentine, A.P., Trampert, J., 2014. Bayesian inversion of free oscillations for Earth's radial (an)elastic structure. Phys. Earth Planet. Inter. 237, 1–17. https://doi.org/10.1016/j.pepi.2014.09.004.

Denis, C., Rogister, Y., Amalvict, M., Delire, C., Denis, A.I., Munhoven, G., 1997. Hydrostatic flattening, core structure, and translational mode of the inner core. Phys. Earth Planet. Inter. 99 (3–4), 195–206. https://doi.org/10.1016/s0031-9201(96)03219-0.

Deuss, A., 2009. Global observations of mantle discontinuities using SS and PP precursors. Surv. Geophys. 30 (4–5), 301–326. https://doi.org/10.1007/s10712-009-9078-y.

Deuss, A., Ritsema, J., Heijst, H., v., 2011. Splitting function measurements for Earth's longest period normal modes using recent large earthquakes. Geophys. Res. Lett. 38 (4), L04303. https://doi.org/10.1029/2010gl046115.

Deuss, A., Ritsema, J., Heijst, H.V., 2013. A new catalogue of normal-mode splitting function measurements up to 10 mHz. Geophys. J. Int. 193, 920–937. https://doi.org/10.1093/gji/ggt010.

Dickey, J.O., 1995. Earth rotation. In: Ahrens, T.J. (Ed.), Global Earth Physics: A Handbook of Physical Constants. American Geophysical Union, Washington D.C., pp. 356–363

Doornbos, D., 1988. Seismological Algorithms. Academic Press, London.

Durek, J.J., 1994. Anelastic Structure of the Mantle from Long-Perod Seismic Data. Ph.D. thesis,. Harvard Univ, Cambridge, Mass.

Durek, J.J., Ekström, G., 1995. Evidence of bulk attenuation in the asthenosphere from recordings of the Bolivia Earthquake. Geophys. Res. Lett. 22 (16), 2309–2312. https://doi.org/10.1029/95gl01434.

Durek, J., Ekström, G., 1996. A radial model of anelasticity consistent with long-period surface-wave attenuation. Bull. Seismol. Soc. Am. 86 (1A), 144–158.

Durek, J.J., Ekström, G., 1997. Investigating discrepancies among measurements of traveling and standing wave attenuation. J. Geophys. Res. Solid Earth 102 (B11), 24529–24544. https://doi.org/10.1029/97jb02160.

Durek, J.J., Ritzwoller, M.H., Woodhouse, J.H., 1993. Constraining upper mantle anelasticity using surface wave amplitude anomalies. Geophys. J. Int. 114 (2), 249–272. https://doi.org/10.1111/j.1365-246x.1993.tb03914.x.

Dziewonski, A.M., 1984. Mapping the lower mantle: determination of lateral heterogeneity in P velocity up to degree and order 6. J. Geophys. Res. 89 (B7), 5929–5952.

Dziewoński, A.M., Anderson, D.L., 1981. Preliminary reference Earth model. Phys. Earth Planet. Inter. 25, 297–356.

Dziewonski, A.M., Gilbert, F., 1976. The effect of small, aspherical perturbations on travel times and a re-examination of the corrections for ellipticity. Geophys. J. Int. 44 (1), 7–17. https://doi.org/10.1111/j.1365-246x.1976.tb00271.x.

Dziewoński, A.M., Hales, A.L., Lapwood, E.R., 1975. Parametrically simple earth models consistent with geophysical data. Phys. Earth Planet. Inter. 10 (1), 12–48. https://doi.org/10.1016/0031-9201(75)90017-5.

Ekström, G., 2011. A global model of Love and Rayleigh surface wave dispersion and anisotropy, 25–250 s. Geophys. J. Int. 187, 1668–1686.

Ekström, G., Dziewonski, A.M., 1998. The unique anisotropy of the Pacific upper mantle. Nature 394, 168–172. https://doi.org/10.1038/28148.

Estabrook, C.H., Kind, R., 1996. The nature of the 660-kilometer upper-mantle seismic discontinuity from precursors to the PP phase. Science 274 (5290), 1179–1182. https://doi.org/10.1126/science.274.5290.1179.

Falzone, A.J., Stacey, F.D., 1980. Second-order elasticity theory: explanation for the high poisson's ratio of the inner core. Phys. Earth Planet. Inter. 21 (4), 371–377. https://doi.org/10.1016/0031-9201(80)90140-5.

Fan, H., 1998. On an Earth ellipsoid best-fitted to the Earth surface. J. Geod. 72 (9), 511–515. https://doi.org/10.1007/s001900050190.

Faul, U.H., Jackson, I., 2005. The seismological signature of temperature and grain size variations in the upper mantle. Earth Planet. Sci. Lett. 234, 119–134.

Flanagan, M.P., Shearer, P.M., 1998. Global mapping of topography on transition zone velocity discontinuities by stacking SS precursors. J. Geophys. Res. 103 (B2), 2673–2692. https://doi.org/10.1029/97jb03212.

French, S.W., Romanowicz, B.A., 2014. Whole-mantle radially anisotropic shear velocity structure from spectral-element waveform tomography. Geophys. J. Int. 199, 1303–1327. https://doi.org/10.1093/gji/ggu334.

Fukao, Y., To, A., Obayashi, M., 2003. Whole mantle P wave tomography using P and PP-P data. J. Geophys. Res. Solid Earth 108 (B1). https://doi.org/10.1029/2001jb000989. ESE 8–14,.

Gaherty, J.B., Wang, Y., Jordan, T.H., Weidner, D.J., 1999. Testing plausible upper-mantle compositions using fine-scale models of the 410-km discontinuity. Geophys. Res. Lett. 26 (11), 1641–1644. https://doi.org/10.1029/1999gl900312.

Giardini, D., Li, X.-D., Woodhouse, J.H., 1987. Three-dimensional structure of the Earth from splitting in free-oscillation spectra. Nature 325, 405–411. https://doi.org/10.1038/325405a0.

Giardini, D., Li, X.-D., Woodhouse, J.H., 1988. Splitting functions of long-period normal modes of the Earth. J. Geophys. Res. 93 (B11), 13716–13742. https://doi.org/10.1029/jb093ib11p13716.

Gilbert, F., Dziewonski, A., 1975. An application of normal mode theory to the retrieval of structural parameters and source mechanisms from seismic spectra. Philos. Trans. R. Soc. Lond. Ser. A Math. Phys. Sci. 187–269.

Groten, E., 2000. Parameters of common relevance of astronomy, geodesy, and geodynamics. J. Geod. 74 (1), 134–140. https://doi.org/10.1007/s00190-000-0134-0.

Gu, Y.J., Dziewonski, A.M., 2002. Global variability of transition zone thickness. J. Geophys. Res. Solid Earth 107. https://doi.org/10.1029/2001jb000489.

Gu, Y.J., Dziewonski, A.M., Ekström, G., 2001. Preferential detection of the Lehmann discontinuity beneath continents. Geophys. Res. Lett. 28 (24), 4655–4658. https://doi.org/10.1029/2001gl013679.

Gu, Y.J., Dziewoński, A.M., Ekström, G., 2003. Simultaneous inversion for mantle shear velocity and topography of transition zone discontinuities. Geophys. J. Int. 154, 559–583.

Häfner, R., Widmer-Schnidrig, R., 2013. Signature of 3-D density structure in spectra of the spheroidal free oscillation ${}_0S_2$. Geophys. J. Int. 192, 285–294. https://doi.org/10.1093/gji/ggs013.

Hales, A.L., Lapwood, E.R., Dziewoński, A.M., 1974. Parameterization of a spherically symmetrical earth model with special references to the upper mantle. Phys. Earth Planet. Inter. 9 (1), 9–12. https://doi.org/10.1016/0031-9201(74)90075-2.

Hansen, P.C., 2006. Analysis of discrete ill-posed problems by means of the L-curve. SIAM Rev. 34 (4), 561–580. https://doi.org/10.1137/1034115.

Hastie, T., Tibshirani, R., 1990. Generalized Additive Models. Chapman and Hall, London.

He, X., Tromp, J., 1996. Normal-mode constraints on the structure of the Earth. J. Geophys. Res. Solid Earth 101 (B9), 20053–20082. https://doi.org/10.1029/96jb01783.

Hirose, K., 2002. Phase transitions in pyrolitic mantle around 670-km depth: implications for upwelling of plumes from the lower mantle. J. Geophys. Res. Solid Earth 107 (B4). https://doi.org/10.1029/2001jb000597. ECV 3–13.

Houser, C., Masters, G., Flanagan, M., Shearer, P., 2008. Determination and analysis of long-wavelength transition zone structure using SS precursors. Geophys. J. Int. 174 (1), 178–194. https://doi.org/10.1111/j.1365-246x.2008.03719.x.

Huang, Q., Schmerr, N., Waszek, L., Beghein, C., 2019. Constraints on seismic anisotropy in the mantle transition zone from long-period SS precursors. J. Geophys. Res. 124 (7), 6779–6800. https://doi.org/10.1029/2019jb017307.

Irifune, T., Shinmei, T., McCammon, C.A., Miyajima, N., Rubie, D.C., Frost, D.J., 2010. Iron partitioning and density changes of pyrolite in Earth's lower mantle. Science 327 (5962), 193–195. https://doi.org/10.1126/science.1181443.

Irving, J.C.E., Cottaar, S., Lekic, V., 2018. Seismically determined elastic parameters for Earth's outer core. Sci. Adv. 4 (6), eaar2538. https://doi.org/10.1126/sciadv.aar2538.

Ishii, T., Huang, R., Myhill, R., Fei, H., Koemets, I., Liu, Z., Maeda, F., Yuan, L., Wang, L., Druzhbin, D., Yamamoto, T., Bhat, S., Farla, R., Kawazoe, T., Tsujino, N., Kulik, E., Higo, Y., Tange, Y., Katsura, T., 2019. Sharp 660-km discontinuity controlled by extremely narrow binary post-spinel transition. Nat. Geosci. 12 (10), 869–872. https://doi.org/10.1038/s41561-019-0452-1.

Jeanloz, R., Knittle, E., 1989. Density and composition of the lower mantle. Philos. Trans. R. Soc. Lond. Ser. A Math. Phys. Sci. 328, 377–389. https://doi.org/10.1098/rsta.1989.0042.

Jeffreys, H., 1932. An alternative to the rejection of observations. Proc. R. Soc. Lond. Ser. A 137 (831), 78–87. https://doi.org/10.2307/95930.

Jeffreys, H., Bullen, K.E., 1940. Seismological Tables. British Association for the Advancement of Science, London.

Jordan, T., 1978. A procedure for estimating lateral variations from low-frequency eigenspectra data. Geophys. J. Int. 52 (3), 441–455.

Kanamori, H., Anderson, D.L., 1977. Importance of physical dispersion in surface-wave and free oscillation problems. Rev. Geophys. 15 (1), 105–112. https://doi.org/10.1029/rg015i001p00105.
Katsura, T., 2022. A revised adiabatic temperature profile for the mantle. J. Geophys. Res. Solid Earth 127 (2). https://doi.org/10.1029/2021jb023562.
Katsura, T., Ito, E., 1989. The system Mg_2SiO_4-Fe_2SiO_4 at high pressures and temperatures: precise determination of stabilities of olivine, modified spinel, and spinel. J. Geophys. Res. Solid Earth 94 (B11), 15663–15670. https://doi.org/10.1029/jb094ib11p15663.
Kennett, B.L.N., 1998. On the density distribution within the Earth. Geophys. J. Int. 132 (2), 374–382. https://doi.org/10.1046/j.1365-246x.1998.00451.x.
Kennett, B.L.N., 2020. Radial earth models revisited. Geophys. J. Int. 222 (3), 2189–2204. https://doi.org/10.1093/gji/ggaa298.
Kennett, B., 2021. The relative behaviour of bulk and shear modulus as an indicator of the iron spin transition in the lower mantle. Earth Planet. Sci. Lett. 559, 116808. https://doi.org/10.1016/j.epsl.2021.116808.
Kennett, B.L.N., Engdahl, E.R., 1991. Traveltimes for global earthquake location and phase identification. Geophys. J. Int. 105 (2), 429–465. https://doi.org/10.1111/j.1365-246x.1991.tb06724.x.
Kennett, B.L.N., Engdahl, E.R., Buland, R., 1995. Constraints on seismic velocities in the Earth from traveltimes. Geophys. J. Int. 122, 108–124. https://doi.org/10.1111/j.1365-246x.1995.tb03540.x.
Khan, M.A., 1983. Primary geodynamical parameters for the Standard Earth Model. Geophys. J. Int. 72 (2), 333–336. https://doi.org/10.1111/j.1365-246x.1983.tb03788.x.
Koper, K.D., Dombrovskaya, M., 2005. Seismic properties of the inner core boundary from PKiKP / P amplitude ratios. Earth Planet. Sci. Lett. 237 (3–4), 680–694. https://doi.org/10.1016/j.epsl.2005.07.013.
Kustowski, B., 2007. Modeling the Anisotropic Shear-Wave Velocity Structure in the Earth's Mantle on Global and Regional Scales. Ph.D. thesis,. Harvard Univ, Cambridge, Mass.
Kustowski, B., Ekström, G., Dziewoński, A.M., 2007. Nonlinear crustal corrections for normal-mode seismograms. Bull. Seismol. Soc. Am. 97, 1756–1762. https://doi.org/10.1785/0120070041.
Kustowski, B., Ekström, G., Dziewonski, A.M., 2008. Anisotropic shear-wave velocity structure of the Earth's mantle: a global model. J. Geophys. Res. 113, B06306. https://doi.org/10.1029/2007jb005169.
Lancaster, P., Salkauskas, K., 1986. Curve and Surface Fitting : An Introduction. London: Academic Press. Academic Press, London.
Laske, G., 2001. Personal Website. https://igppweb.ucsd.edu/~gabi/rem.html accessed: 2010-08-01.
Laske, G., Masters, G., 1996. Constraints on global phase velocity maps from long-period polarization data. J. Geophys. Res. 101 (B7), 16059–16075. https://doi.org/10.1029/96jb00526.
Laske, G., Masters, G., Ma, Z., Pasyanos, M., 2013. Update on CRUST1.0 - a 1-degree global model of Earth's crust. Geophys. Res. Abstr. 15. Abstract EGU2013–2658.
Lawrence, J.F., Shearer, P.M., 2006. Constraining seismic velocity and density for the mantle transition zone with reflected and transmitted waveforms. Geochem. Geophys. Geosyst. 7 (10), Q10012. https://doi.org/10.1029/2006gc001339.
Lebedev, S., van der Hilst, R.D., 2008. Global upper-mantle tomography with the automated multimode inversion of surface and S-wave forms. Geophys. J. Int. 173 (2), 505–518. https://doi.org/10.1111/j.1365-246x.2008.03721.x.
Lekic, V., Matas, J., Panning, M., Romanowicz, B., 2009. Measurement and implications of frequency dependence of attenuation. Earth Planet. Sci. Lett. 282 (1–4), 285–293. https://doi.org/10.1016/j.epsl.2009.03.030.
Lekic, V., Panning, M., Romanowicz, B., 2010. A simple method for improving crustal corrections in waveform tomography. Geophys. J. Int. 182 (1), 265–278.
Li, X., Tanimoto, T., 1993. Waveforms of long-period body waves in a slightly aspherical Earth model. Geophys. J.R. Astron. Soc. 112, 91–102. https://doi.org/10.1111/j.1365-246x.1993.tb01439.x.
Li, X., Giardini, D., Woodhouse, J., 1991. Large-scale three-dimensional even-degree structure of the Earth from splitting of long-period normal modes. J. Geophys. Res. 96 (B1), 551–577.
Li, C., van der Hilst, R.D., Engdahl, E.R., Burdick, S., 2008. A new global model for P wave speed variations in Earth's mantle. Geochemistry 9 (5). https://doi.org/10.1029/2007gc001806.
Luzum, B., Capitaine, N., Fienga, A., Folkner, W., Fukushima, T., Hilton, J., Hohenkerk, C., Krasinsky, G., Petit, G., Pitjeva, E., Soffel, M., Wallace, P., 2011. The IAU 2009 system of astronomical constants: the report of the IAU working group on numerical standards for Fundamental Astronomy. Celest. Mech. Dyn. Astron. 110 (4), 293–304. https://doi.org/10.1007/s10569-011-9352-4.
Ma, Z., Masters, G., Laske, G., Pasyanos, M., 2014. A comprehensive dispersion model of surface wave phase and group velocity for the globe. Geophys. J. Int. 199 (1), 113–135. https://doi.org/10.1093/gji/ggu246.
Malinverno, A., 2002. Parsimonious Bayesian Markov chain Monte Carlo inversion in a nonlinear geophysical problem. Geophys. J. Int. 151 (3), 675–688. https://doi.org/10.1046/j.1365-246x.2002.01847.x.
Masters, G., 1979. Observational constraints on the chemical and thermal structure of the Earth's deep interior. Geophys. J. R. Astron. Soc. 57 (2), 507–534. https://doi.org/10.1111/j.1365-246x.1979.tb04791.x.
Masters, G., Gubbins, D., 2003. On the resolution of density within the Earth. Phys. Earth Planet. Inter. 140 (1–3), 159–167. https://doi.org/10.1016/j.pepi.2003.07.008.
Masters, G., Laske, G., 1997. On bias in surface wave and free oscillation attenuation measurements. EOS Trans. Am. Geophys. Union 78, F485.
Masters, T., Widmer, R., 1995. Free oscillations: Frequencies and attenuations. In: Global Earth Physics: A Handbook of Physical Constants, vol. 1. American Geophysical Union, Washington, DC, pp. 104–125.
Masters, G., Jordan, T.H., Silver, P.G., Gilbert, F., 1982. Aspherical Earth structure from fundamental spheroidal-mode data. Nature 298 (5875), 609–613. https://doi.org/10.1038/298609a0.
Masters, G., Park, J., Gilbert, F., 1983. Observations of coupled spheroidal and toroidal modes. J. Geophys. Res. 88, 10285–10298. https://doi.org/10.1029/jb088ib12p10285/full.
Masters, G., Woodhouse, J.H., Gilbert, F., 2011. Mineos v1.0.2 [software], computational infrastructure for geodynamics. https://geodynamics.org/cig/software/mineos.
McDonough, W.F., Sun, S.S., 1995. The composition of the Earth. Chem. Geol. 120 (3–4), 223–253. https://doi.org/10.1016/0009-2541(94)00140-4.
Menke, W., 1989. Geophysical Data Analysis: Discrete Inverse Theory. Academic, San Diego, Calif.
Michelini, A., McEvilly, T.V., 1991. Seismological studies at Parkfield. I. Simultaneous inversion for velocity structure and hypocenters using cubic B-splines parameterization. Bull. Seismol. Soc. Am. 81 (2), 524–552. https://doi.org/10.1785/bssa0810020524.
Mochizuki, E., 1986a. Free oscillations and surface waves of an aspherical Earth. Geophys. Res. Lett. 13 (13), 1478–1481. https://doi.org/10.1029/gl013i013p01478.
Mochizuki, E., 1986b. The free oscillations of an anisotropic and heterogeneous Earth. Geophys. J. Int. 86 (1), 167–176.
Mohr, P.J., Newell, D.B., Taylor, B.N., 2016. CODATA recommended values of the fundamental physical constants: 2014. Rev. Mod. Phys. 88 (3), 337. https://doi.org/10.1103/revmodphys.88.035009.
Montagner, J., Jobert, N., 1988. Vectorial tomography: II. Application to the Indian Ocean. Geophys. J. Int. 94, 309–344. https://doi.org/10.1111/j.1365-246x.1988.tb05904.x.
Morelli, A., Dziewonski, A., 1991. Joint determination of lateral heterogeneity and earthquake location. In: Sabadani, R., Lambeck, K., Boschi, E. (Eds.), Glacial Isostasy, Sea-Level Change and Mantle Rheology. Kluwer Academic, Dordrecht, pp. 515–534.
Morelli, A., Dziewonski, A.M., 1993. Body wave traveltimes and a spherically symmetric P- and S-wave velocity model. Geophys. J. Int. 112 (2), 178–194. https://doi.org/10.1111/j.1365-246x.1993.tb01448.x.
Moulik, P., Ekström, G., 2014. An anisotropic shear velocity model of the Earth's mantle using normal modes, body waves, surface waves and long-period waveforms. Geophys. J. Int. 199, 1713–1738. https://doi.org/10.1093/gji/ggu356.
Moulik, P., Ekström, G., 2016. The relationships between large-scale variations in shear velocity, density, and compressional velocity in the Earth's mantle. J. Geophys. Res. 121, 2737–2771. https://doi.org/10.1002/2015jb012679.
Moulik, P., Ekström, G., 2025. Radial structure of the Earth: (II) Model features and interpretations. Phys. Earth Planet. Inter. https://doi.org/10.1016/j.pepi.2025.107320.
Moulik, P., The 3D Reference Earth Model (REM3D) Consortium, 2022. Three-Dimensional Reference Earth Model Project: Data, Techniques, Models & Tools. American Geophysical Union (AGU) Fall Meeting, Chicago, IL, USA. https://doi.org/10.5281/zenodo.7883683.
Moulik, P., Lekic, V., Romanowicz, B., Ma, Z., Schaeffer, A., Ho, T., Beucler, E., Debayle, E., Deuss, A., Durand, S., Ekström, G., Lebedev, S., Masters, G., Priestley, K., Ritsema, J., Sigloch, K., Trampert, J., Dziewonski, A.M., 2022. Global reference seismological data sets: multimode surface wave dispersion. Geophys. J. Int. 228 (3), 1808–1849. https://doi.org/10.1093/gji/ggab418.
Moulik, P., Maguire, R., Gassmoeller, R., Havlin, C., 2023. AVNI: Analysis and Visualization Toolkit for plaNetary Inferences. https://doi.org/10.5281/zenodo.10035731.
Murakami, M., Hirose, K., Kawamura, K., Sata, N., Ohishi, Y., 2004. Post-perovskite phase transition in MgSiO3. Science 304, 855–858. https://doi.org/10.1126/science.1095932.
Nakiboglu, S.M., 1982. Hydrostatic theory of the Earth and its mechanical implications. Phys. Earth Planet. Inter. 28 (4), 302–311. https://doi.org/10.1016/0031-9201(82)90087-5.
Nelder, J.A., Mead, R., 1965. A simplex method for function minimization. Comput. J. 7, 308–313.
Nettles, M., Dziewonski, A.M., 2008. Radially anisotropic shear velocity structure of the upper mantle globally and beneath North America. J. Geophys. Res. 113 (B2), B02303. https://doi.org/10.1029/2006jb004819.
Nishimura, C.E., Forsyth, D.W., 1989. The anisotropic structure of the upper mantle in the Pacific. Geophys. J. Int. 96, 203–229. https://doi.org/10.1111/j.1365-246x.1989.tb04446.x.
Nolet, G., 1990. Partitioned waveform inversion and two-dimensional structure under the network of autonomously recording seismographs. J. Geophys. Res. 95 (B6), 8499. https://doi.org/10.1029/jb095ib06p08499.
Nolet, G., Moser, T.-J., 1993. Teleseismic delay times in a 3-D earth and a new look at the S discrepancy. Geophys. J. Int. 114 (1), 185–195. https://doi.org/10.1111/j.1365-246x.1993.tb01478.x.
Park, J., 1986. Synthetic seismograms from coupled free oscillations: effects of lateral structure and rotation. J. Geophys. Res. Solid Earth 91, 6441–6464. https://doi.org/10.1029/jb091ib06p06441.

Park, J., 1987. Asymptotic coupled-mode expressions for multiplet amplitude anomalies and frequency shifts on an aspherical earth. Geophys. J.R. Astron. Soc. 90, 129–169. https://doi.org/10.1111/j.1365-246x.1987.tb00679.x.

Pavlis, N.K., Holmes, S.A., Kenyon, S.C., Factor, J.K., 2012. The development and evaluation of the Earth Gravitational Model 2008 (EGM2008). J. Geophys. Res. Solid Earth 117 (B4), 1–38. https://doi.org/10.1029/2011jb008916.

Press, W.H., Teukolsky, S.A., Vetterling, W.T., Flannery, B.P., 1992. Numerical Recipes in Fortran 77: The Art of Scientific Computing. Cambridge University Press.

Resovsky, J.S., Pestana, R., 2003. Improved normal mode constraints on lower mantle vp from generalized spectral fitting. Geophys. Res. Lett. 30 (7), 1383. https://doi.org/10.1029/2002gl015790.

Resovsky, J., Ritzwoller, M., 1998. New and refined constraints on three-dimensional Earth structure from normal modes below 3 mHz. J. Geophys. Res. 103, 783–810.

Resovsky, J., Trampert, J., van der Hilst, R.D., 2005. Error bars for the global seismic Q profile. Earth Planet. Sci. Lett. 230 (3–4), 413–423. https://doi.org/10.1016/j.epsl.2004.12.008.

Revenaugh, J., Jordan, T.H., 1991a. Mantle layering from ScS reverberations: 1. Waveform inversion of zeroth-order reverberations. J. Geophys. Res. Solid Earth 96 (B12), 19749–19762. https://doi.org/10.1029/91jb01659.

Revenaugh, J., Jordan, T.H., 1991b. Mantle layering from ScS reverberations: 2. The transition zone. J. Geophys. Res. Solid Earth 96 (B12), 19763–19780. https://doi.org/10.1029/91jb01486.

Ries, J.C., Eanes, R.J., Shum, C.K., Watkins, M.M., 1992. Progress in the determination of the gravitational coefficient of the Earth. Geophys. Res. Lett. 19 (6), 529–531. https://doi.org/10.1029/92gl00259.

Ringwood, A.E., 1975. Composition and Petrology of the Earth's Mantle. McGraw-Hill, New York.

Ritsema, J., Deuss, A., van Heijst, H.J., 2011. S40RTS: a degree-40 shear-velocity model for the mantle from new Rayleigh wave dispersion, teleseismic traveltime and normal-mode splitting function measurements. Geophys. J. Int. 184, 1223–1236. https://doi.org/10.1111/j.1365-246x.2010.04884.x.

Ritzwoller, M., Masters, G., Gilbert, F., 1986. Observations of anomalous splitting and their interpretation in terms of aspherical structure. J. Geophys. Res. Solid Earth 91 (B10), 10203–10228. https://doi.org/10.1029/jb091ib10p10203.

Romanowicz, B., 1987. Multiplet-multiplet coupling due to lateral heterogeneity: asymptotic effects on the amplitude and frequency of the Earth's normal modes. Geophys. J.R. Astron. Soc. 90, 75–100. https://doi.org/10.1111/j.1365-246x.1987.tb00676.x.

Romanowicz, B., 1995. A global tomographic model of shear attenuation in the upper mantle. J. Geophys. Res. 100, 12375–12394.

Romanowicz, B., Lambeck, K., 1977. The mass and moment of inertia of the Earth. Phys. Earth Planet. Inter. 15, 1–4. https://doi.org/10.1016/0031-9201(77)90002-4.

Romanowicz, B., Mitchell, B., 2007. Deep earth structure: Q of the earth from crust to core. In: Schubert, G. (Ed.), Treatise on Geophysics, vol. 1. Elsevier, Oxford, UK, pp. 731–774.

Roult, G., Clévédé, E., 2000. New refinements in attenuation measurements from free-oscillation and surface-wave observations. Phys. Earth Planet. Inter. 121, 1–37. https://doi.org/10.1016/s0031-9201(00)00155-2.

Roult, G., Romanowicz, B., Montagner, J.-P., 1990. 3-D upper mantle shear velocity and attenuation from fundamental mode free oscillation data. Geophys. J. Int. 101, 61–80.

Sailor, R.V., Dziewonski, A.M., 1978. Measurements and interpretation of normal mode attenuation. Geophys. J. Int. 53 (3), 559–581. https://doi.org/10.1111/j.1365-246x.1978.tb03760.x.

Schneider, S., Deuss, A., 2020. A new catalogue of toroidal-mode overtone splitting function measurements. Geophys. J. Int. 1–33. https://doi.org/10.1093/gji/ggaa567/6008151.

Seidelmann, P.K., 1992. Explanatory Supplement to the Astronomical Almanac. A Revision to the Explanatory Supplement to the Astronomical Ephemeris and the American Ephemeris and Nautical Almanac. University Science Books.

Selby, N., Woodhouse, J., 2000. Controls on Rayleigh wave amplitudes: attenuation and focusing. Geophys. J. Int. 142 (3), 933–940.

Selby, N.D., Woodhouse, J.H., 2002. The Q structure of the upper mantle: constraints from Rayleigh wave amplitudes. J. Geophys. Res. Solid Earth 107 (B5). https://doi.org/10.1029/2001jb000257. ESE 5–11.

Shearer, P.M., 1990. Seismic imaging of upper-mantle structure with new evidence for a 520-km discontinuity. Nature 344 (6262), 121–126. https://doi.org/10.1038/344121a0.

Shearer, P.M., 1991. Constraints on upper mantle discontinuities from observations of long-period reflected and converted phases. J. Geophys. Res. Solid Earth 96 (B11), 18147–18182. https://doi.org/10.1029/91jb01592.

Shearer, P.M., 1993. Global mapping of upper mantle reflectors from long-period SS precursors. Geophys. J. Int. 115 (3), 878–904. https://doi.org/10.1111/j.1365-246x.1993.tb01499.x.

Shearer, P.M., 1996. Transition zone velocity gradients and the 520-km discontinuity. J. Geophys. Res. 101 (B2), 3053–3066. https://doi.org/10.1029/95jb02812.

Shearer, P.M., Flanagan, M.P., 1999. Seismic velocity and density jumps across the 410- and 660-kilometer discontinuities. Science 285 (5433), 1545–1548. https://doi.org/10.1126/science.285.5433.1545.

Shearer, P., Masters, G., 1990. The density and shear velocity contrast at the inner core boundary. Geophys. J. Int. 102 (2), 491–498. https://doi.org/10.1111/j.1365-246x.1990.tb04481.x.

Shearer, P., Masters, T.G., 1992. Global mapping of topography on the 660-km discontinuity. Nature 355, 791–796. https://doi.org/10.1038/355791a0.

Silver, P.G., Jordan, T.H., 1981. Fundamental spheroidal mode observations of aspherical heterogeneity. Geophys. J.R. Astron. Soc. 64, 605–634. https://doi.org/10.1111/j.1365-246x.1981.tb02687.x.

Smith, M.F., Masters, G., 1989. Aspherical structure constraints from free oscillation frequency and attenuation measurements. J. Geophys. Res. Solid Earth Planets 94, 1953–1976. https://doi.org/10.1029/jb094ib02p01953/asset/jgrb6905.pdf.

Souriau, A., Souriau, M., 1989. Ellipticity and density at the inner core boundary from subcritical PKiKP and PcP data. Geophys. J. Int. 98 (1), 39–54. https://doi.org/10.1111/j.1365-246x.1989.tb05512.x.

Speziale, S., Milner, A., Lee, V.E., Clark, S.M., Pasternak, M.P., Jeanloz, R., 2005. Iron spin transition in Earth's mantle. Proc. Natl. Acad. Sci. 102 (50), 17918–17922. https://doi.org/10.1073/pnas.0508919102.

Stacey, F.D., 1995. Theory of thermal and elastic properties of the lower mantle and core. Phys. Earth Planet. Inter. 89 (3–4), 219–245. https://doi.org/10.1016/0031-9201(94)03005-4.

Stacey, F.D., 1997. Bullen's seismological homogeneity parameter, η, applied to a mixture of minerals: the case of the lower mantle. Phys. Earth Planet. Inter. 99 (3–4), 189–193. https://doi.org/10.1016/s0031-9201(96)03218-9.

Stacey, F.D., 2005. High pressure equations of state and planetary interiors. Rep. Prog. Phys. 68 (2), 341–383. https://doi.org/10.1088/0034-4885/68/2/r03.

Stixrude, L., Lithgow-Bertelloni, C., 2011. Thermodynamics of mantle minerals - II. Phase equilibria. Geophys. J. Int. 184, 1180–1213. https://doi.org/10.1111/j.1365-246x.2010.04890.x.

Stixrude, L., Lithgow-Bertelloni, C., 2012. Geophysics of chemical heterogeneity in the mantle. Annu. Rev. Earth Planet. Sci. 40, 569–595. https://doi.org/10.1146/annurev.earth.36.031207.124244.

Tackley, P.J., Stevenson, D.J., Glatzmaier, G.A., Schubert, G., 1993. Effects of an endothermic phase transition at 670 km depth in a spherical model of convection in the Earth's mantle. Nature 361 (6414), 699–704. https://doi.org/10.1038/361699a0.

Tkalčić, H., Kennett, B.L.N., Cormier, V.F., 2009. On the inner—outer core density contrast from PKiKP/PcP amplitude ratios and uncertainties caused by seismic noise. Geophys. J. Int. 179 (1), 425–443. https://doi.org/10.1111/j.1365-246x.2009.04294.x.

Trampert, J., Woodhouse, J.H., 1995. Global phase-velocity maps of Love and Rayleigh-waves between 40 and 150 seconds. Geophys. J. Int. 122, 675–690.

Trenberth, K.E., Smith, L., Trenberth, K.E., Smith, L., 2005. The mass of the atmosphere: a constraint on global analyses. J. Clim. 18, 864–875. https://doi.org/10.1175/jcli-3299.1.

Tromp, J., Dahlen, F.A., 1992. Variational principles for surface wave propagation on a laterally heterogeneous Earth—II. Frequency-domain JWKB theory. Geophys. J.R. Astron. Soc. 109, 599–619. https://doi.org/10.1111/j.1365-246x.1992.tb00120.x.

Tsuchiya, T., Wentzcovitch, R.M., Silva, C.R.S.D., Gironcoli, S.D., 2006. Spin transition in Magnesiowüstite in Earth's lower mantle. Phys. Rev. Lett. 96 (19), 198501. https://doi.org/10.1103/physrevlett.96.198501.

Vacher, P., Mocquet, A., Sotin, C., 1998. Computation of seismic profiles from mineral physics: the importance of the non-olivine components for explaining the 660 km depth discontinuity. Chem. Geol. 106, 275–298. https://doi.org/10.1016/s0031-9201(98)00076-4.

Valencia-Cardona, J.J., Williams, Q., Shukla, G., Wentzcovitch, R.M., 2017. Bullen's parameter as a seismic observable for spin crossovers in the lower mantle. Geophys. Res. Lett. 44, 9314–9320. https://doi.org/10.1002/2017gl074666.

Vinet, P., Ferrante, J., Rose, J.H., Smith, J.R., 1987. Compressibility of solids. J. Geophys. Res. Solid Earth 92 (B9), 9319–9325. https://doi.org/10.1029/jb092ib09p09319.

Wang, Z., Dahlen, F.A., 1994. JWKB surface-wave seismograms on a laterally heterogeneous earth. Geophys. J. Int. 119, 381–401. https://doi.org/10.1111/j.1365-246x.1994.tb00130.x.

Waszek, L., Deuss, A., 2015. Anomalously strong observations of PKiKP/PcP amplitude ratios on a global scale. J. Geophys. Res. 120 (7), 5175–5190. https://doi.org/10.1002/2015jb012038.

Weidner, D.J., Wang, Y., 2000. Phase transformations: Implications for mantle structure. In: Karato, S., Forte, A., Liebermann, R., Masters, G., Stixrude, L. (Eds.), Earth's Deep Interior: Mineral Physics and Tomography From the Atomic to the Global Scale, Geophys. Monogr. Ser, vol. 117. American Geophysical Union, Washington, D. C, pp. 215–235.

Wentzcovitch, R.M., Yu, Y.G., Wu, Z., 2010. Thermodynamic properties and phase relations in mantle minerals investigated by first principles quasiharmonic theory. Rev. Mineral. Geochem. 71 (1), 59–98. https://doi.org/10.2138/rmg.2010.71.4.

Widmer, R., 1991. Earth's Elastic and Density Structure from Diverse Seismological Observations. Ph.D. thesis,. Univ. Cal, San Diego., New York, NY.

Widmer, R., Masters, G., Gilbert, F., 1991. Spherically symmetric attenuation within the Earth from normal mode data. Geophys. J. Int. 104 (3), 541–553. https://doi.org/10.1111/j.1365-246x.1991.tb05700.x.

Widmer, R., Zürn, W., Masters, G., 1992. Observation of low-order toroidal modes from the 1989 Macquarie Rise event. Geophys. J. Int. 111, 226–236.

Widmer-Schnidrig, R., 2002. Application of regionalized multiplet stripping to retrieval of aspherical structure constraints. Geophys. J. Int. 148, 201–213.
Woodhouse, J.H., 1981. A note on the calculation of travel times in a transversely isotropic Earth model. Phys. Earth Planet. Inter. 25 (4), 357–359. https://doi.org/10.1016/0031-9201(81)90047-9.
Woodhouse, J., 1988. The calculation of the eigenfrequencies and eigenfunctions of the free oscillations of the earth and the sun. In: D, J.D. (Ed.), Seismological Algorithms. Academic Press, San Diego, CA, pp. 321–370.
Woodhouse, J.H., Dziewoński, A.M., 1984. Mapping the upper mantle: three-dimensional modeling of Earth structure by inversion of seismic waveforms. J. Geophys. Res. 89, 5953–5986.
Woodhouse, J.H., Girnius, T.P., 1982. Surface waves and free oscillations in a regionalized earth model. Geophys. J. Int. 68 (3), 653–673. https://doi.org/10.1111/j.1365-246x.1982.tb04921.x.
Woodhouse, J.H., Wong, Y.K., 1986. Amplitude, phase and path anomalies of mantle waves. Geophys. J. Int. 87, 753–773. https://doi.org/10.1111/j.1365-246x.1986.tb01970.x.
Woodhouse, J., Giardini, D., LI, X., 1986. Evidence for inner core anisotropy from free oscillations. Geophys. Res. Lett. 13 (13), 1549–1552.
Yoder, C.F., 1995. Earth rotation. In: Ahrens, T.J. (Ed.), Astronomic and Geodetic Properties of the Earth and the Solar System. American Geophysical Union, Washington D.C., pp. 1–31
Yu, Y.G., Wentzcovitch, R.M., Tsuchiya, T., Umemoto, K., Weidner, D.J., 2007. First principles investigation of the postspinel transition in Mg_2SiO_4. Geophys. Res. Lett. 34, L10306. https://doi.org/10.1029/2007gl029462.
Yu, Y.G., Wu, Z., Wentzcovitch, R.M., 2008. α–β–γ transformations in Mg_2SiO_4 in Earth's transition zone. Chem. Geol. 273, 115–122. https://doi.org/10.1016/j.epsl.2008.06.023.